Doctoral Thesis

Accurate and fast hydrodynamic modeling of fluvial and pluvial floods at large scales

submitted in satisfaction of the requirements for the degree of
Doctor of Science
of the TU Wien, Faculty of Civil Engineering
as part of the Vienna Doctoral Programme on Water Resource Systems

by

Dipl.-Ing. **Andreas Buttinger-Kreuzhuber**
Matrikelnummer 0826671

Examiner: Univ.Prof. Dipl.-Ing. Dr.techn. **Günter Blöschl**
                 Institut für Wasserbau und Ingenieurhydrologie
                 TU Wien
                 Karlsplatz 13/222, 1040 Vienna, Austria

Examiner: Univ.Prof. Dipl.-Ing. Dr.techn. **Christian Bucher**
                 Institut für Hochbau, Baudynamik und Gebäudetechnik
                 TU Wien
                 Karlsplatz 13/208, 1040 Vienna, Austria

Examiner: Prof. Dr.-Ing. **Reinhard Hinkelmann**
                 Institut Bauingenieurwesen
                 Fachgebiet Wasserwirtschaft und Hydrosystemmodellierung
                 TU Berlin
                 Gustav-Meyer-Allee 25, 13355 Berlin, Germany

Co-Supervisor: Dipl-Ing. Dr.techn. **Jürgen Waser**
                 VRVis Zentrum für Virtual Reality und Visualisierung
                 Donau-City-Straße 11, 1220 Vienna, Austria

Vienna, August 2021   ....

Dissertation

Genaue und schnelle hydrodynamische Modellierung von Flusshochwässern und Starkregenereignissen

ausgeführt zum Zwecke der Erlangung des akademischen Grades eines
Doktors der technischen Wissenschaften
eingereicht an der Technischen Universität Wien, Fakultät für Bauingenieurwesen
als Teil des Doktoratskollegs für Water Resource Systems

von

Dipl.-Ing. **Andreas Buttinger-Kreuzhuber**

Matrikelnummer 0826671

Gutachter:	Univ.Prof. Dipl.-Ing. Dr.techn. **Günter Blöschl** Institut für Wasserbau und Ingenieurhydrologie TU Wien Karlsplatz 13/222, 1040 Wien
Gutachter:	Univ.Prof. Dipl.-Ing. Dr.techn. **Christian Bucher** Institut für Hochbau, Baudynamik und Gebäudetechnik TU Wien Karlsplatz 13/208, 1040 Wien
Gutachter:	Prof. Dr.-Ing. **Reinhard Hinkelmann** Institut Bauingenieurwesen Fachgebiet Wasserwirtschaft und Hydrosystemmodellierung TU Berlin Gustav-Meyer-Allee 25, 13355 Berlin
Co-Betreuer:	Dipl-Ing. Dr.techn. **Jürgen Waser** VRVis Zentrum für Virtual Reality und Visualisierung Donau-City-Straße 11, 1220 Wien

Wien, August 2021 ....

Abstract

Floods are the most costly natural disaster worldwide, causing significant socio-economic losses. There is a growing concern that floods are increasing in frequency and magnitude due to climate change. In order to mitigate the disastrous consequences, flood management agencies, regional planners, and insurance companies rely on an accurate modeling of inundated areas. The reliability of large-scale flood hazard maps, which show the probability of flooding at a specific location within a certain time period, is of key importance. Previous large-scale studies show limitations in terms of accuracy and local relevance in the delineated inundation maps. The aim of this thesis is to develop accurate and efficient methods for fluvial and pluvial flood hazard assessment at large scales.

In a first step, the focus is on the numerical scheme for solving the instationary two-dimensional shallow water equations (SWEs). In the SWEs, the bed source term accounts for the gravitational acceleration due to a sloped bed. In finite volume methods, the treatment of discontinuities in the bed source term across cell interfaces is challenging. To address this issue, a second-order accurate scheme is developed based on a recently introduced first-order accurate scheme. The novel scheme involves a specialized reconstruction of water levels and bed levels enabling an accurate resolution of shallow flows over abruptly changing bed topography. The scheme's accuracy is verified with analytical solutions in several Riemann problems and the parabolic basin test case, and it is shown to outperform previous schemes. The scheme is also validated on historic flood events in Malpasset, France, and Lobau, Austria, showing good agreement between simulated and observed water level records.

Second, the presented second-order scheme is applied in an inundation modeling framework for Austria at a resolution of 2 m. Given an arbitrary tiling of the region of interest, the framework automatically sets up boundary conditions and executes the hydraulic simulation. For an efficient simulation, discharges are adjusted along the 33,880 km long stream network to maintain the prescribed flood probabilities. In combination with a parallelized implementation running on 10 graphics processing units (GPUs), the delineation of an inundated area of 3500 km^2 for a 100-year flood takes less than a month. The approach shows good agreement between simulated and measured data at stream gauges, as well as between simulated inundated areas and local flood hazard maps, achieving a critical success index (CSI) score of 0.7.

Third, an integrated modeling framework is proposed that accounts for processes relevant for flash floods. Interception and infiltration is modeled in a time-dependent, spatially distributed way. For urban scenarios, the surface flow is coupled with the sewer network in an interleaved way, which allows parallel time-stepping. Except for the sewer network simulation, all models are implemented on a GPU, resulting in runtimes up to 1000 times faster than a sequential execution on a central processing

Abstract

unit (CPU) core. For rainfall–runoff modeling, the first-order accurate scheme at a higher resolution is more efficient than the novel second-order accurate scheme at a lower resolution. The coupled model is able to accurately simulate areas of up to 200 km^2 with a resolution of 1 m.

Overall, this thesis contributes to current research on large-scale flood hazard mapping through innovative methods with enhanced accuracy and computational efficiency.

Kurzfassung

Hochwässer verursachen erhebliche sozioökonomische Kosten und sind die teuerste Naturkatastrophe weltweit. Infolge des Klimawandels steigt die Besorgnis, dass diese Extremereignisse an Häufigkeit und Intensität zunehmen. Um deren negative Konsequenzen zu vermindern, ist für Hochwasserschutzdienste, Raumplanungsbehörden und Versicherungen die genaue und flächendeckende Kenntnis möglicher Überflutungsflächen wichtig. Überflutungsflächen geben die mit einer bestimmten Wahrscheinlichkeit in einem gewissen Zeitraum überschwemmten Teile der Landschaft an. Großskalige Berechnungen von Überflutungsflächen wiesen bisher hinsichtlich ihrer Rechengenauigkeit und der Berücksichtigung lokaler Effekte Einschränkungen auf. Das Ziel dieser Arbeit ist es, genaue und effiziente Methoden zur flächendeckenden Ausweisung der Überflutungsgefahr von Flusshochwässern und Starkregenereignissen zu entwickeln.

Im ersten Teil der Arbeit liegt der Fokus auf der Entwicklung eines numerischen Schemas für die Lösung der zeitabhängigen zweidimensionalen Flachwassergleichungen. Bei der Methode der finiten Volumen ist die Behandlung von Unstetigkeiten im Quellterm der Flachwassergleichungen an den Zellrändern herausfordernd. Dieser Quellterm berücksichtigt die Beschleunigung des Fluids auf einer geneigten Fläche aufgrund der Erdanziehungskraft. Um eine steile und sich abrupt verändernde Topographie numerisch zuverlässig zu behandeln, wird eine spezielle Rekonstruktion der Wasserstände und der Bodentopographie eingeführt und in ein neu entwickeltes Rechenschema zweiter Ordnung integriert. Die Genauigkeit des Schemas wird an Riemannproblemen und dem Testproblem "parabolisches Becken" verifiziert. Für historische Ereignisse in Malpasset, Frankreich, und in der Lobau, Österreich, gibt es eine gute Übereinstimmung zwischen simulierten und gemessenen Wasserständen. Das neue Rechenschema weist eine größere Genauigkeit bei kürzeren oder ähnlichen Rechenzeiten als vorangegangene Schemata auf.

Im zweiten Teil der Arbeit wird das entwickelte Rechenschema in einem Framework zur Berechnung von Überflutungsflächen mit einer Auflösung von 2 m für ganz Österreich angewandt. Das Framework berechnet sowohl Randbedingungen als auch Überflutungsflächen vollautomatisch unter der Voraussetzung, dass das Gebiet bereits in Rechenkacheln unterteilt wurde. Die Durchflüsse werden entlang des 33 880 km langen Flussnetzes angepasst, um die vorgegebene Jährlichkeit des Ereignisses (z.B. 100 Jahre) zu erhalten. Die Einführung dieser effizienten Methode und eine hochgradig parallelisierte Implementierung auf 10 Grafikkarten (GPUs) resultiert in einer Rechenzeit von weniger als einem Monat für $3\,500$ km^2 an Überflutungsflächen in Österreich für ein 100-jährliches Hochwasser. Das Modell weist eine gute Übereinstimmung zwischen gemessenen und simulierten Wasserstands–Durchfluss–Beziehungen an Flusspegeln sowie zwischen lokalen Gefahrenzonen (GFZ) und simulierten Überflutungsflächen (Critical Success Index von 0.7) auf.

Kurzfassung

Im dritten Teil der Arbeit wird das entwickelte Schema mit numerischen Modellen zur Beschreibung der hydrologischen Prozesse bei Starkregen gekoppelt. Zum Beispiel werden Versickerung und Wasserrückhalt durch die Vegetation mit räumlich verteilten, zeitabhängigen Modellen beschrieben. Für urbane Gebiete wird die Simulation des Oberflächenabflusses mit einer Kanalnetzsimulation gekoppelt. Die Simulationen laufen innerhalb eines Kopplungsschrittes parallel, wodurch schnellere Rechenzeiten erzielt werden. Mit Ausnahme der Kanalnetzsimulation werden die Rechenmodelle auf GPUs implementiert, sodass eine über tausendfache Beschleunigung im Vergleich zu einem einzigen CPU Kern erreicht wird. Für die Simulation von Starkregen ist die Verwendung des Rechenschemas erster Ordnung bei höherer Auflösung gegenüber dem Schema zweiter Ordnung bei niedriger Auflösung zu bevorzugen. Das gekoppelte Modell ermöglicht die genaue Simulation der Überflutungsflächen von bis zu 200 km^2 großen urbanen Gebieten mit einer Auflösung von 1 m.

Diese Arbeit trägt durch innovative Ansätze, welche eine verbesserte Genauigkeit und eine gesteigerte rechnerische Effizienz bieten, zur Forschung in der großskaligen hydrodynamischen Modellierung von Hochwassergefahren bei.

I am very grateful to my supervisor Prof. Günter Blöschl for giving me this opportunity and for always providing great guidance. I would like to thank Prof. Christian Bucher and Prof. Reinhard Hinkelmann for reviewing my thesis.

I am thankful to Jürgen Waser for co-supervising this thesis and his day-by-day support at the VRVis Research Centre and to my colleagues in the research group Integrated Simulations, especially Daniel Cornel, Zsolt Horváth, and Artem Konev. Many thanks to the staff at the VRVis, in particular to the members of the 12:30 fellowship, who made lunch breaks much more enjoyable.

I wish to thank my fellow students and friends from the Vienna Doctoral Program on Water Resource Systems for all the stimulative conversations during the last five years.

Another big thanks goes to my friends and the Mathe Homies for providing welcome distraction after work.

Last but not least, I want to thank my family for constantly supporting me. Finally, I want to thank my dearest one for always being there for me.

Contents

Contents

List of acronyms

ALS	airborne laser scanning
ARS	approximate Riemann solver
BC	boundary condition
CFL	Courant–Friedrichs–Lewy
CN	Chen and Noelle
CPU	central processing unit
CSI	critical success index
DTM	digital terrain model
DTM-H	hydrologically enforced digital terrain model
EBS	error bias
FAR	false alarm ratio
FEM	finite element method
FV	finite volume
FVM	finite volume method
GA	Green–Ampt
GI	green infrastructure
GPU	graphics processing unit
HLLC	Harten–Lax–van Leer-contact
HOAL	Hydrological Open Air Laboratory
HR	hydrostatic reconstruction
HTR	hit rate
LID	low-impact development
LIDAR	light detection and ranging
MAE	mean absolute error
MSE	mean signed error
ODE	ordinary differential equation
PDE	partial differential equation
RP	Riemann problem
SV	Saint-Venant
SW	shallow water
SWE	shallow water equation
SWMM	Storm Water Management Model

1 Introduction

Both frequency and intensity of floods have recently increased in parts of Europe (Alfieri et al., 2015; Blöschl et al., 2015; Blöschl et al., 2019). For example, Austria was hit by major floods in 2005, 2013 (Blöschl et al., 2013), and, more recently, in 2019. This accumulation of floods in the last decades stimulates discussions about trends in floods linked to climate change (Alfieri et al., 2017). Moreover, intensifying sub-daily heavy rain events due to rising temperatures (Chen et al., 2018) are expected to increase the occurrence of flash floods. Just a few weeks ago, on July 13 up to 150 mm of rain fell in 24 hours in western Germany and parts of Belgium, causing one of the deadliest recent flash floods in Europe (Cornwall, 2021). Flash floods are characterized by very short durations. In Bavaria, Germany, catchments smaller than 100 km^2 show a median rising time of 8 hours, but also rising times as short as an hour occur (Kaiser et al., 2020). The rapidity of these events results in a higher mortality compared to fluvial floods (Jonkman, 2005).

Risk-orientated flood management approaches are considered essential in order to minimize human life loss and economic damage and are required by the European Union Flood Directive (European Commission, 2007). According to the Directive, flood risk is defined as the combination of flood hazard, i. e. the probability of flooding at a certain location within a certain time span, and of the associated adverse consequences. A critical step in the derivation of flood hazard maps is the simulation of water flow, and in particular of the maxima of flow velocities and water depths at each location in a region. The accuracy of simulated flood hazard maps is of paramount importance, thus the simulation needs to be accurate yet fast enough to be completed within a reasonable timespan.

The motion of fluids is described by the Navier–Stokes equations, which express conservation of mass and conservation of momentum for Newtonian fluids (Temam, 1984). A particular case is inviscid flow, which is governed by the Euler equations. Under the assumption of incompressible flow, hydrostatic pressure approximation, and constant density of the fluid, the shallow water equations (SWEs) can be derived from the Navier–Stokes equations by depth-averaging (Whitham, 1999b; Gerbeau and Perthame, 2001). The SWEs provide a widely used description of water flow assuming that the flow is shallow, i. e. the vertical depth is small compared to the horizontal length scale. Mass and momentum are conserved in the homogeneous SWEs, i. e. in the SWEs without source terms. Therefore, the homogeneous SWEs are a so-called system of conservation laws. Often, viscous and turbulent terms are neglected, yielding a set of hyperbolic partial differential equations (PDEs). A distinctive feature of hyperbolic PDEs is a bounded domain of dependence as the characteristic waves travel at a finite speed, given by the eigenvalues. However, in the quasilinear SWEs, an initially smooth state may transition into a discontinuous solution, a process called shock formation. This discontinuity in the solution is

challenging from an analytical and numerical perspective, as numerical solvers based on a smooth representation of the solution require a high resolution for resolving the shock.

In the case of mesh- or grid-based, so-called Eulerian, discretizations, finite element methods (FEMs) and finite volume methods (FVMs) are typically used to solve the SWEs or its one-dimensional variant, the Saint-Venant equations. The FEM reframes the problem in a variational setting. The solution is sought in a finite-dimensional space, usually piecewise polynomial functions. In order to represent discontinuous solutions, a FEM variant, the discontinuous Galerkin FEM, is typically used, where restrictions on the smoothness of the global solution are relaxed (Klöckner et al., 2009; Kesserwani and Liang, 2012). The FVM is a popular method as it directly ensures the conservation of mass and momentum. In the FVM, the solution is approximated by average values over cells or so-called finite volumes. Between the cells, numerical fluxes are exchanged at the interfaces and can be computed with approximate Riemann solvers.

The accuracy of finite volume schemes hinges both on the order of accuracy for the smooth regions of the solution as well as on a correct resolution of the bed source term at discontinuities (Audusse and Bristeau, 2005; Noelle et al., 2006). The bed source term accounts for gravitational acceleration due to a sloped bottom topography. In particular, numerical issues arise in the vicinity of wet–dry boundaries and for steep or abruptly changing bottom topography (Audusse et al., 2004; Chinnayya et al., 2004; Bollermann et al., 2013; Hou et al., 2013b; Hou et al., 2013a; Morales de Luna et al., 2013; Horváth et al., 2015; Chen and Noelle, 2017). Additionally, the numerical scheme is required to preserve at least specific steady states, such as a lake at rest, a property termed well-balancedness (Bouchut, 2004; Castro et al., 2007; Murillo and García-Navarro, 2012; Duran et al., 2013). Still, even popular methods with a low computational footprint, e.g. the hydrostatic reconstruction (HR) method (Audusse et al., 2004; Audusse and Bristeau, 2005), suffer from limitations in steep terrain (Delestre et al., 2012). Thus, there is a need for computationally efficient methods that combine higher order accuracy with an appropriate treatment of bed discontinuities for shallow flows in complex terrain.

The accuracy of the hydrodynamic simulation also relies on the grid resolution so that the digital terrain model (DTM) is able to resolve terrain features and buildings. Small, localized modifications of the terrain, e.g. retention basins and levees, may protect otherwise flooded areas and vice versa, since inundation is a complex and nonlinear process. However, regional to continental flood inundation models traditionally operate on resolutions of 30 to 100 m, which are too coarse to resolve for example levees. In this case, post-processing steps are required, e.g. down-sampling procedures (Falter et al., 2016; Bates et al., 2021). Unfortunately, high resolutions come with slow simulation runtimes due to the Courant–Friedrichs–Lewy (CFL) condition (Courant et al., 1967), which links the time step with the spatial resolution via the numerical wave speeds in explicit time integration methods. The effective runtime increases by a factor of 5 to 7 times if the grid cell size is halved (Horváth et al., 2020). As river floods often last over a week, the model runtime limits

the usage of high resolutions in fluvial flood hazard mapping. In order to improve accuracy, efficient methods for large-scale flood hazard mapping are needed, which will pave the way for high-resolution simulations that still remain computationally feasible.

To speed up simulations, simplifying assumptions, such as neglecting the advection term in the SWEs, are common in continental models (Alfieri et al., 2014; Wing et al., 2017; Bates et al., 2021). In contrast to the full or dynamic SWEs, simplified SWEs may lead to unsatisfactory results at wet–dry boundaries (Cozzolino et al., 2019) and in urban regions (Costabile et al., 2017; Costabile et al., 2020). For urban regions, the inclusion of microtopography and buildings as anisotropic porosity in the SWEs is an interesting option to enable fast runtimes (Özgen et al., 2016). A viable, generic alternative is to accelerate model runtimes with graphics processing units (GPUs). More than a decade ago, shallow water solvers were first implemented on GPUs (Acuña and Aoki, 2009; Brodtkorb et al., 2010; Brodtkorb et al., 2012). Since then, GPU implementations of the SWEs have become increasingly popular (Horváth et al., 2016; Xing et al., 2018; Echeverribar et al., 2019; Xia et al., 2019; Morales-Hernández et al., 2021).

The accuracy of the simulated inundated areas also depends on the considered processes and the modeled level of detail. For the accurate assessment of pluvial flood hazard, a comprehensive approach including simulation of interception of rainfall by vegetation, infiltration of surface water into soil, flow through culverts, and urban sewer network systems is necessary. Spatial variations in land use, small-scale alterations of street elevation, clogged culverts or sewer overflows may have significant effects on local flood hazard. Particularly in urban areas, soil permeability may change abruptly due to sealed surfaces or green infrastructure (GI), e. g. green roofs, bioswales, and rain gardens, which are intended to reduce flash flood risk as part of low-impact development (Rosenzweig et al., 2021). For a thorough assessment of hot spots in the urban stormwater management system, coupling the surface runoff with the sewer network is inevitable. Thus, spatially distributed modeling of these hydrologic processes and their interactions at a high resolution is important (Almeida et al., 2016; Berland et al., 2017; Noh et al., 2018). To guide regional planners in the development of new city quarters, multiple simulations need to be evaluated that account for different scenarios. Moreover, numerous simulations or so-called ensemble simulations are needed for calibration and uncertainty analysis, thus fast runtimes are crucial. To accelerate accurate flood hazard assessment, culverts, sewers, and multiple submodels for spatially distributed rainfall runoff processes need to be included and preferably implemented on the GPU.

The aim of this thesis is to contribute to the recent research on fast and accurate numerical schemes and on locally relevant hydrodynamic modeling of fluvial and pluvial flood hazards. Specifically, this thesis goes beyond the existing literature with the following key points. First, a novel second-order scheme for a fast and accurate hydrodynamic simulation over abruptly changing topography is presented. Second, this research bridges the gap between detailed local models that account for small-scale features affecting flood hazard and large-scale models that partially

neglect them by enabling high resolutions through innovative computational methods. Third, this thesis aims for a comprehensive assessment of fluvial and pluvial floods by integrating multiple model components.

The main chapters of this thesis each correspond to a scientific paper. Chapter 2 introduces a well-balanced shallow water scheme, which is second-order accurate and builds upon a novel reconstruction approach. Furthermore, an economical approximation of the source term and a robust treatment of wet–dry zones are introduced, which reduce computation times. Chapter 3 presents the application of the proposed second-order scheme for the delineation of inundated areas for a stream network of 33,880 km on a 2 by 2 m^2 grid. Moreover, a novel approach for maintaining consistent flood probabilities along the river network is proposed. In Chapter 4, an integrated framework for pluvial flood hazard assessment is presented, where each model component operates in a spatially distributed way so that local measures, e. g. GI, are fully taken into account. The complete surface runoff model is implemented on the GPU enabling fast runtimes. Finally, Chapter 5 presents a summary along with the main conclusions and possible directions for future work.

2 A fast second-order shallow water scheme on two-dimensional structured grids over abrupt topography

The present chapter corresponds to the following scientific publication in its original form:

A. Buttinger-Kreuzhuber, Z. Horváth, S. Noelle, G. Blöschl, and J. Waser (2019). A fast second-order shallow water scheme on two-dimensional structured grids over abrupt topography. *Advances in Water Resources* 127, pp. 89–108. DOI: 10.1016/j.advwatres.2019.03.010.

Abstract

This paper presents a finite volume scheme on structured grids to simulate shallow flows over complex terrain. The situation of shallow downhill flow over a step is particularly challenging for most shallow water schemes. We study this situation in detail and devise a novel second-order reconstruction strategy, which gives superior results over former hydrostatic reconstruction (HR) schemes. The reconstruction step is based on a recent first-order HR method, which improves shallow flows over steps. The proposed second-order scheme is well-balanced, positivity-preserving, and handles dry cells. When compared with the original HR, we lower the computational burden by using a simplified quadrature for the bed slope source term. We test the scheme on various benchmark setups to assess accuracy and robustness, where the method produces comparable results to other HR-based schemes in most cases and superior results in the case of shallow downhill flow over steps. The novel second-order scheme is capable of simulating large-scale real-world flood scenarios fast and accurately.

2.1 Introduction

The shallow water equations (SWEs) describe the motion of an incompressible fluid under the gravitational force. They provide plausible and reliable results of water levels for tsunamis, river floods, dam breaks, and levee breaches (Audusse et al., 2004; Brodtkorb et al., 2012; Asunción et al., 2013; Hervouet and Petitjean, 1999; Liang and Marche, 2009; Russo, 2005). Based on the assumption that the horizontal length scale is large compared to the vertical length scale, the SWEs can be derived by depth averaging the Navier-Stokes equations (Temam, 1984; Whitham, 1999a).

The finite volume method (FVM) is a common numerical method for solving the SWEs. For the spatial discretization, a computational grid has to be chosen. Un-

structured triangular meshes are able to incorporate complex geometries, however they require time-consuming mesh generation. In contrast, rectangular grids lack the pre-processing step at the expense of poor resolution of topographic features not aligned with the grid. This issue can be overcome with the cut-cell technique (An and Yu, 2012; Ingram et al., 2003). Furthermore, in the context of second-order methods, slope reconstruction on unstructured grids has a great influence on the solution quality, thus making it harder to compare schemes (Buffard and Clain, 2010; Hou et al., 2014). Also, numeric models on Cartesian grids are easier to implement and faster than their counterparts on unstructured grids. They are suitable for straightforward parallelization on graphics processing units (GPUs) due to their simplicity, which reduces computation times by a factor of up to 100 compared to conventional programming models (Brodtkorb et al., 2012; Horváth et al., 2016; Vacondio et al., 2016). For temporal evolution, usually a strong-stability-preserving Runge-Kutta method is employed, such as the second-order Heun's method (Bouchut, 2007; Gottlieb et al., 2001).

A stable and efficient way to solve the SWEs are schemes derived by the hydrostatic reconstruction (HR) method, developed by Audusse et al. (2004). The superior stability properties of this scheme – it is positivity preserving, well-balanced and satisfies a semi-discrete in-cell entropy inequality – contributed to its popularity (Berthon and Foucher, 2012; Castro et al., 2007; Clain et al., 2016; Hou et al., 2013a; Liang and Marche, 2009; Noelle et al., 2006). The HR scheme in combination with a kinetic solver satisfies a fully discrete entropy inequality with an error term coming from the topography (Audusse et al., 2016). Thus, convergence of this scheme can be expected for Lipschitz continuous bathymetry.

In first-order and second-order finite volume (FV) schemes the bottom topography is approximated by piecewise constant and piecewise linear functions, respectively, thus giving rise to discontinuities in the bottom at the discrete level. In practice, large discontinuous bottom steps may occur at coarse spatial resolutions or in stormwater scenarios, where the water layer is often thinner than the stepsize of the bottom jumps. As bottom steps appear at the discrete level of FVMs, there is a need to stretch the applicability of the SWEs also to cases involving discontinuous bathymetries. This leads to mathematical and numerical problems, since then the product of the depth and the bottom gradient cannot be understood in a distributional sense. The mathematical theory of nonconservative products in the source term is an active field of research (Dal Maso et al., 1995). Even if discontinuous bathymetries are not within the theoretical assumptions of the SWEs, Morales de Luna et al. (2013) note that the SWEs still give reasonable results in the case of small enough bottom jumps. Altogether, this motivates the study of shallow water flows over bottom steps and their numerical approximation.

In the case of shallow downhill flow, the original first-order HR scheme does not properly account for the acceleration due to a sloped bottom (Delestre et al., 2012). This effect can be mitigated by switching from a first-order to a second-order approximation. Morales de Luna et al. (2013) improve the original first-order HR scheme in the case of partially wet interfaces. Recently, Chen and Noelle (2017) proposed a

new reconstruction which features an even better approximation of the source term in case of shallow downhill flows, leading to a new first-order scheme, called the CN scheme in this work. Also they present a way to investigate and derive the two existing HR schemes by means of subcell reconstructions. Xia et al. (2017) present a Surface Reconstruction Method (SRM) to overcome the problem of partially wet interfaces, which they describe by the term "waterfall effect". In their first-order scheme, a second-order approximation of the bottom is used in all cells to reconstruct the water surface and the bottoms at the interfaces for the flux and source term computation. Other strategies to further improve the flow over abrupt topography include considering the conservation of the total head instead of the conservation of the hydrostatic equilibrium. Such schemes are also called energy-balanced methods and typically require additional waves in the approximate Riemann solver (ARS) to resolve the stationary bottom discontinuity at the interface. This leads to additional complexity in the solver, both implementation-wise and performance-wise (Goutal et al., 2017; LeFloch and Thanh, 2011; Murillo and García-Navarro, 2010; Murillo and García-Navarro, 2013; Murillo and Navas-Montilla, 2016).

Another numerical difficulty arises at wet-dry zones, characterized by interfaces between dry and wet cells. A robust numerical scheme should be able to maintain nonnegativity of water depth, but should also avoid unphysically high velocities in these sensitive regions. Typically, at wet-dry zones, the wet cells only feature a thin layer of water thus giving rise to large velocities when the discharge is divided by a small depth. Different methods are tailored to tackle this problem (Hou et al., 2013b; Horváth et al., 2015). In Hou et al. (2013b), a novel source treatment, which is slightly faster than the original source terms as in Audusse et al. (2004), for unstructured grids is introduced.

In this paper, we present a new two-dimensional scheme, which is second-order accurate. It is based on the hydrostatic reconstruction procedure of Chen and Noelle (2017). The second-order accuracy allows us to reduce the discretization error and perform more accurate simulation runs. We apply a simple source treatment, which is computationally efficient and leads to a minor loss of accuracy in typical use cases. Furthermore, our proposed reconstruction is adapted to limit the velocities, which reduces the occurrence of unphysically high velocities, and to correctly reconstruct the solution variables in the vicinity of abrupt changes in the bottom topography and in the water levels. In particular, our method is able to capture the drying process in regions with complex terrain in a robust and efficient way. This approach ensures that the time step, which is connected to the velocities by the Courant–Friedrichs–Lewy (CFL) condition, is not overly restricted when simulating large time spans. Our proposed source term approximation coincides with the simple and economical source term of Hou et al. (Hou et al., 2013b) in fully wet regions. For shallow flow over abrupt topography, the novel scheme outperforms previous schemes based on the HR method. We remark again that discontinuous bottom steps are not within the theoretical assumptions on the derivation of the shallow water (SW) model, however, they appear by construction in first-order and second-order FVMs. Thus, the correct handling of bottom steps in the numerical approximation, including the

reconstruction procedure as well as the source term discretization, is important. We propose to reconstruct the HR water depth from bottom slopes instead of water level slopes in regions where the topography changes abruptly. This novel "adaptive" second-order reconstruction allows us to significantly increase accuracy of shallow flow down a bottom step, when compared to other second-order HR-based schemes.

The paper is organized as follows. In Section 2.2, we discuss the model equations, the HR schemes and present the second-order scheme based on a new HR (Chen and Noelle, 2017) in detail. In Section 2.3, we present numerical experiments highlighting the advantages and disadvantages of our proposed scheme. We extensively verify the presented scheme on multiple benchmark tests, including a dam break over bottom steps, seven Riemann problems, the parabolic bump, and the parabolic basin. We validate the scheme on the Malpasset dam break and a river flood event. Finally, in Section 2.4, we conclude the findings of this work and give a brief outlook into future works.

This paper contributes with the following key points:

1) a two-dimensional well-balanced scheme based on an improved hydrostatic reconstruction

2) a novel second-order reconstruction which yields superior results for shallow downhill flows over a step,

3) an economical approximation of the source term to speed up computation,

4) reduction of unphysically high velocities at wet-dry zones.

2.2 Model equations and numerical methods

2.2.1 The shallow water equations

In this section, we describe the shallow water model and the FVM for SW schemes. The hyperbolic conservation law described by the two-dimensional shallow water equation (SWE), also referred to as the Saint-Venant system, with geometric source term can be written as

$$\begin{bmatrix} h \\ hu \\ hv \end{bmatrix}_t + \begin{bmatrix} hu \\ hu^2 + \frac{1}{2}gh^2 \\ huv \end{bmatrix}_x + \begin{bmatrix} hv \\ huv \\ hv^2 + \frac{1}{2}gh^2 \end{bmatrix}_y = \begin{bmatrix} 0 \\ -ghb_x \\ -ghb_y \end{bmatrix}, \tag{2.1}$$

where h represents the water height, hu is the discharge along the x-axis, hv is the discharge along the y-axis (Figure 2.1a), u and v are the average flow velocities in x and y-direction respectively, g is the gravitational constant, and b is the bathymetry (assumed to be time-independent). Subscripts represent partial derivatives, e.g., $\mathbf{U}_t$ stands for $\frac{\partial \mathbf{U}}{\partial t}$. In vector form the system writes

$$\mathbf{U}_t + \mathbf{F}(\mathbf{U}, b)_x + \mathbf{G}(\mathbf{U}, b)_y = \mathbf{S}(\mathbf{U}, b), \tag{2.2}$$
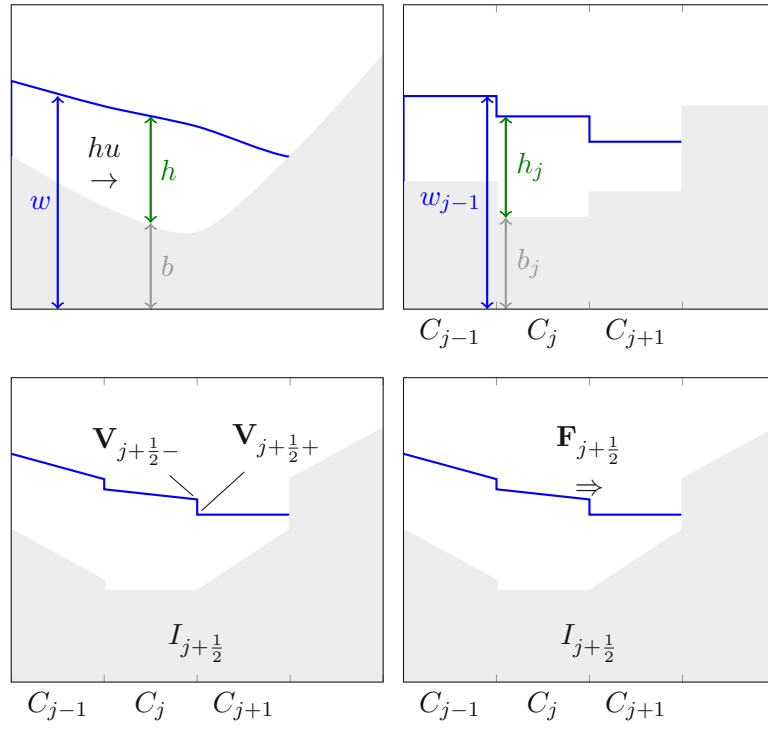
Fig. 2.1. Schematic one-dimensional view of a shallow water flow, definition of the variables, and flux computation. a) Continuous variables. b) The conserved variables $\mathbf{U} = [h, hu, hv]^T$ are discretized as cell averages $\mathbf{U}_{j,k}$ on the cell $C_{j,k}$. c) Left- and right-sided point values $\mathbf{V}_{j+1/2\mp,k}$ are reconstructed at the cell interface $I_{j+1/2,k}$. d) Fluxes $\mathbf{F}$ are computed using the HLL flux at the cell interfaces.

where $\mathbf{U} = [h, hu, hv]^T$ is the vector of conserved variables, $\mathbf{F}$ and $\mathbf{G}$ are flux functions. The bed slope term $\mathbf{S}$ models the fluid's acceleration due to the gravitational forces. An additional friction term $\mathbf{S}_f(\mathbf{U})$ can be included on the right hand side of (2.2), which is introduced in Section 2.2.10.

In two dimensions, the SWEs allow for complicated steady state solutions, however we restrict ourselves to two important steady-state equilibria. Following Chen and Noelle (2017), there is the *still-water* equilibrium, i. e.,

$$u, v = 0 \text{ and } \nabla w = 0, \tag{2.3}$$

where w denotes the water level $w = h + B$, and the *lake at rest* equilibrium, which includes dry shores, i. e.,

$$hu, hv = 0 \text{ and } h \nabla w = 0. \tag{2.4}$$

If a numerical scheme is capable of balancing source and numerical flux terms for these two stationary solutions it is called *well-balanced* and thus preserves the lake at rest and also the still-water equilibrium.

2.2.2 Discretization

We choose a uniform grid $x_\alpha := \alpha \Delta x$ and $y_\beta := \beta \Delta y$, where Δx and Δy are the cell sizes. We denote by $C_{j,k}$ the cell $C_{j,k} := [x_{j-1/2}, x_{j+1/2}] \times [y_{k-1/2}, y_{k+1/2}]$. The SWEs are discretized by the method of lines. The FVM is chosen for the spatial discretization on top of the uniform grid. An FVM discretizes the conserved variables $\mathbf{U}$ as cell averages, e.g., $\mathbf{U}_{j,k}$ for the finite volume $C_{j,k}$. This yields a system of ordinary differential equations for the cell averages

$$\frac{d}{dt}\mathbf{U}_{j,k}(t) = -\frac{\mathbf{F}_{j+\frac{1}{2},k}(t) - \mathbf{F}_{j-\frac{1}{2},k}(t)}{\Delta x} - \frac{\mathbf{G}_{j,k+\frac{1}{2}}(t) - \mathbf{G}_{j,k-\frac{1}{2}}(t)}{\Delta y} + \mathbf{S}_{j,k}(t), \quad (2.5)$$

where $\mathbf{F}_{j\mp\frac{1}{2},k}$ and $\mathbf{G}_{j,k\mp\frac{1}{2}}$ are the discretized interface fluxes and $\mathbf{S}_{j,k}$ is an appropriate source term discretization.

2.2.3 Hydrostatic reconstruction

To achieve well-balancedness, it is necessary to introduce a special reconstruction for the Riemann states that are fed into the approximate Riemann solver. Assuming time-independent bathymetry values $b_{j,k} := b(x_j, y_k)$ at the cell centers, the essential idea of the hydrostatic reconstruction (HR) technique is to redefine the interface bottom values used for deriving the Riemann states in oreder to ensure well-balancedness and positivity. The name HR method originates from the fact that the associated HR scheme balances the hydrostatic pressure and the topographic source terms at each interface in the still water steady-state. We illustrate the technique only in x-direction, the application to the y-direction can be done analogously.

In the following, we briefly summarize the original first-order HR of Audusse (Aud) (Audusse et al., 2004) and the modification of Chen and Noelle (CN) (Chen and Noelle, 2017). In both first-order schemes, there is only one hydrostatically reconstructed bathymetry value at each interface. The original first-order HR evaluates the interface bottom values b^* in an upwind fashion (Audusse et al., 2004),

$$b^{*,\mathrm{Aud}}_{j+\frac{1}{2},k} = \max(b_{j+1,k}, b_{j,k}). \tag{2.6}$$

The left- and right-sided interface heights with respect to the interface $I_{j+1/2,k}$ between cell $C_{j,k}$ and $C_{j+1,k}$ are then defined as

$$\begin{aligned}
h^{*,\mathrm{Aud}}_{j+\frac{1}{2}-,k}(t) &= \max(w_{j,k}(t) - b^{*,\mathrm{Aud}}_{j+\frac{1}{2},k}, 0), \\
h^{*,\mathrm{Aud}}_{j+\frac{1}{2}+,k}(t) &= \max(w_{j+1,k}(t) - b^{*,\mathrm{Aud}}_{j+\frac{1}{2},k}, 0).
\end{aligned} \tag{2.7}$$

This definition ensures the nonnegativity of the water depths h.
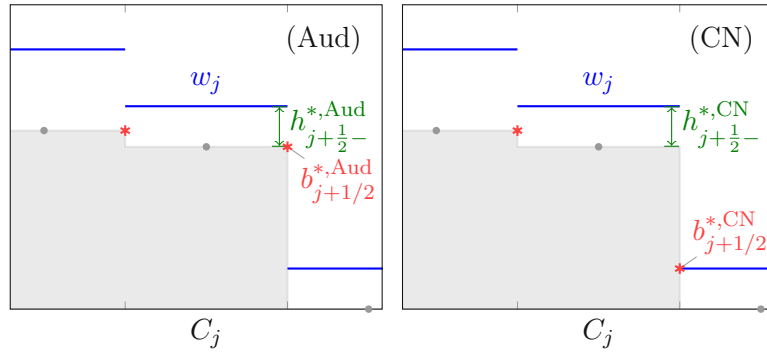
Fig. 2.2. First-order hydrostatic reconstruction in the case of shallow flow over discontinuous bottom. Water levels w are shown as blue lines and the bathymetry is visualized in gray. At the right partially wet interface, Audusse's scheme gives interface bathymetry values $b^{*,\text{Aud}}$, which are different to the values $b^{*,\text{CN}}$ provided by the CN scheme. The HR interface bathymetry values are marked with red asterisks.

The CN scheme (Chen and Noelle, 2017) improves the original reconstruction on partially-wet cases where an adjacent water level is lower than the bottom topography, i. e.

$$\underline{w}_{j+1/2,k}(t) := \min(w_{j,k}(t), w_{j+1,k}(t)) < b^{*,\text{Aud}}_{j+\frac{1}{2},k}. \tag{2.8}$$

The CN scheme defines the interface bottom values b^* as

$$b^{*,\text{CN}}_{j+\frac{1}{2},k}(t) = \min(b^{*,\text{Aud}}_{j+\frac{1}{2},k}, \underline{w}_{j+\frac{1}{2},k}(t)). \tag{2.9}$$

The interface heights h^* are given by

$$\begin{aligned}
h^{*,\text{CN}}_{j+\frac{1}{2}-,k}(t) &= \min(w_{j,k}(t) - b^{*,\text{CN}}_{j+\frac{1}{2},k}(t), h_{j,k}(t)), \\
h^{*,\text{CN}}_{j+\frac{1}{2}+,k}(t) &= \min(w_{j+1,k}(t) - b^{*,\text{CN}}_{j+\frac{1}{2},k}(t), h_{j+1,k}(t)).
\end{aligned} \tag{2.10}$$

For a constant water level W, the interface depths are then continuous across interfaces, that is

$$\max(W - b^{*,\text{Aud}}_{j+\frac{1}{2},k}, 0) = h^{*,\text{Aud}}_{j+\frac{1}{2}-,k} = h^{*,\text{Aud}}_{j+\frac{1}{2}+,k} = \max(W - b^{\text{Aud}}_{j+\frac{1}{2},k}, 0). \tag{2.11}$$

The continuous depths then make it easy to show well-balancedness for consistent fluxes, see Section 2.2.9. We remark that the hydrostatic interface heights h^* of the two first-order schemes do not differ, only the HR interface bathymetry values differ in partially wet cells (Chen and Noelle, 2017), compare also Figure 2.2.

2.2.4 Second-order reconstruction

For second-order accuracy, left- and right-sided point values have to be computed at the cell interface midpoints through slopes taking into account the neighbouring values. The left-sided point values of a cell $C_{j,k}$ are then denoted by subscripts $j - 1/2+$ and $k - 1/2+$ in x- and y-dimension, respectively. We reconstruct $\mathbf{V} = [h, u, v, w]^T$ instead of the conserved variables (Audusse et al., 2004; Bouchut, 2007). From now on, we omit time dependence in the equations, since all reconstructed variables are time-dependent. To suppress unphysical oscillations, the generalised minmod-limiter is applied to the slopes (Van Leer, 1979; Sweby, 1984; Nessyahu and Tadmor, 1990)

$$
\begin{aligned}
\mathrm{D}_x \mathbf{V}_{j,k} &= \mathrm{minmod}\left(\theta \frac{\mathbf{V}_{j,k} - \mathbf{V}_{j-1,k}}{\Delta x}, \frac{\mathbf{V}_{j+1,k} - \mathbf{V}_{j-1,k}}{2\Delta x}, \theta \frac{\mathbf{V}_{j+1,k} - \mathbf{V}_{j,k}}{\Delta x}\right), \\
\mathrm{D}_y \mathbf{V}_{j,k} &= \mathrm{minmod}\left(\theta \frac{\mathbf{V}_{j,k} - \mathbf{V}_{j,k-1}}{\Delta y}, \frac{\mathbf{V}_{j,k+1} - \mathbf{V}_{j,k-1}}{2\Delta y}, \theta \frac{\mathbf{V}_{j,k+1} - \mathbf{V}_{j,k}}{\Delta y}\right),
\end{aligned}
\tag{2.12}
$$

where θ between 1 and 2. The minmod limiter is given by (Nessyahu and Tadmor, 1990)

$$
\mathrm{minmod}(a,b,c) = \begin{cases} \min(a,b,c) & \text{if } a,b,c \geq 0, \\ \max(a,b,c) & \text{if } a,b,c \leq 0, \\ 0 & \text{otherwise} \end{cases}
\tag{2.13}
$$

The value of θ controls the amount of dispersion added to the system and is chosen to be 1.3 in our simulations. This choice of slope limiting conserves the maximum principle. The left- and right-sided water depth point values are given by

$$
\begin{aligned}
h_{j-\frac{1}{2}+,k} &= h_{j,k} - \frac{\Delta x}{2}\mathrm{D}_x h_{j,k}, & h_{j,k-\frac{1}{2}+} &= h_{j,k} - \frac{\Delta y}{2}\mathrm{D}_y h_{j,k}, \\
h_{j+\frac{1}{2}-,k} &= h_{j,k} + \frac{\Delta x}{2}\mathrm{D}_x h_{j,k}, & h_{j,k+\frac{1}{2}-} &= h_{j,k} + \frac{\Delta y}{2}\mathrm{D}_y h_{j,k},
\end{aligned}
\tag{2.14}
$$

and the left- and right-sided water level point values by

$$
\begin{aligned}
w_{j-\frac{1}{2}+,k} &= w_{j,k} - \frac{\Delta x}{2}\mathrm{D}_x w_{j,k}, & w_{j,k-\frac{1}{2}+} &= w_{j,k} - \frac{\Delta y}{2}\mathrm{D}_y w_{j,k}, \\
w_{j+\frac{1}{2}-,k} &= w_{j,k} + \frac{\Delta x}{2}\mathrm{D}_x w_{j,k}, & w_{j,k+\frac{1}{2}-} &= w_{j,k} + \frac{\Delta y}{2}\mathrm{D}_y w_{j,k}.
\end{aligned}
\tag{2.15}
$$

Velocity reconstruction

According to Bouchut (2007), we reconstruct velocities $[u, v] = [hu/h, hv/h]$ instead of discharges hu, hv to avoid high velocities near dry cells. To satisfy the conservativity requirement dimension-wise on the discharges, the point values have to satisfy

$$
hu_{j,k} = \frac{1}{2}\left(h_{j-\frac{1}{2}+,k} u_{j-\frac{1}{2}+,k} + h_{j+\frac{1}{2}-,k} u_{j+\frac{1}{2}-,k}\right),
\tag{2.16}
$$

and

$$hu_{j,k} = \frac{1}{2}\left(h_{j,k-\frac{1}{2}+}u_{j,k-\frac{1}{2}+} + h_{j,k+\frac{1}{2}-}u_{j,k+\frac{1}{2}-}\right), \tag{2.17}$$

and analogously for hv. Thus, the velocity point values are modified accordingly to these equations giving

$$
\begin{aligned}
u_{j-\frac{1}{2}+,k} &= \frac{hu_{j,k}}{h_{j,k}} - \frac{h_{j+\frac{1}{2}-,k}}{h_{j,k}}\frac{\Delta x}{2}\mathrm{D}_x u_{j,k}, \\
u_{j+\frac{1}{2}-,k} &= \frac{hu_{j,k}}{h_{j,k}} + \frac{h_{j-\frac{1}{2}+,k}}{h_{j,k}}\frac{\Delta x}{2}\mathrm{D}_x u_{j,k},
\end{aligned}
\tag{2.18}
$$

and

$$
\begin{aligned}
u_{j,k-\frac{1}{2}+} &= \frac{hu_{j,k}}{h_{j,k}} - \frac{h_{j,k+\frac{1}{2}-}}{h_{j,k}}\frac{\Delta y}{2}\mathrm{D}_y u_{j,k}, \\
u_{j,k+\frac{1}{2}-} &= \frac{hu_{j,k}}{h_{j,k}} + \frac{h_{j,k-\frac{1}{2}+}}{h_{j,k}}\frac{\Delta y}{2}\mathrm{D}_y u_{j,k}.
\end{aligned}
\tag{2.19}
$$

The same modification is applied for the velocity v. We remark that the depth point values in (2.14) are not yet hydrostatically reconstructed. If the interface water depth, e.g., $h_{j+1/2-,k}$, is smaller than some dry threshold ϵ_{dry}, we set the respective velocity to zero in the reconstruction step, i.e. $hu_{j,k}/h_{j,k}$ is set to zero if $h_{j,k} < \epsilon$ for all j,k.

Second-order hydrostatic reconstruction

Here, we describe the procedure used in Audusse et al. (2004) to get second-order HR water heights h^* at the interfaces. The left- and right-sided second-order bottom point values are given by subtracting the water depth from the level, i.e.

$$
\begin{aligned}
b_{j-\frac{1}{2}+,k} &= w_{j-\frac{1}{2}+,k} - h_{j-\frac{1}{2}+,k}, \quad & b_{j,k-\frac{1}{2}+} &= w_{j,k-\frac{1}{2}+} - h_{j,k-\frac{1}{2}+}, \\
b_{j+\frac{1}{2}-,k} &= w_{j+\frac{1}{2}-,k} - h_{j+\frac{1}{2}-,k}, \quad & b_{j,k+\frac{1}{2}-} &= w_{j,k+\frac{1}{2}-} - h_{j,k+\frac{1}{2}-}.
\end{aligned}
\tag{2.20}
$$

From the second-order bottom point values at the interfaces, the HR interface bottom values are set to

$$b_{j+\frac{1}{2},k}^{*,\mathrm{Aud}} = \max(b_{j+\frac{1}{2}-,k}, b_{j+\frac{1}{2}+,k}). \tag{2.21}$$

Then the hydrostatic interface heights h^* are reconstructed by

$$
\begin{aligned}
h_{j-\frac{1}{2}+,k}^{*,\mathrm{Aud}} &= \max(w_{j-\frac{1}{2}+,k} - b_{j-\frac{1}{2},k}^{*,\mathrm{Aud}}, 0). \\
h_{j+\frac{1}{2}-,k}^{*,\mathrm{Aud}} &= \max(w_{j+\frac{1}{2}-,k} - b_{j+\frac{1}{2},k}^{*,\mathrm{Aud}}, 0).
\end{aligned}
\tag{2.22}
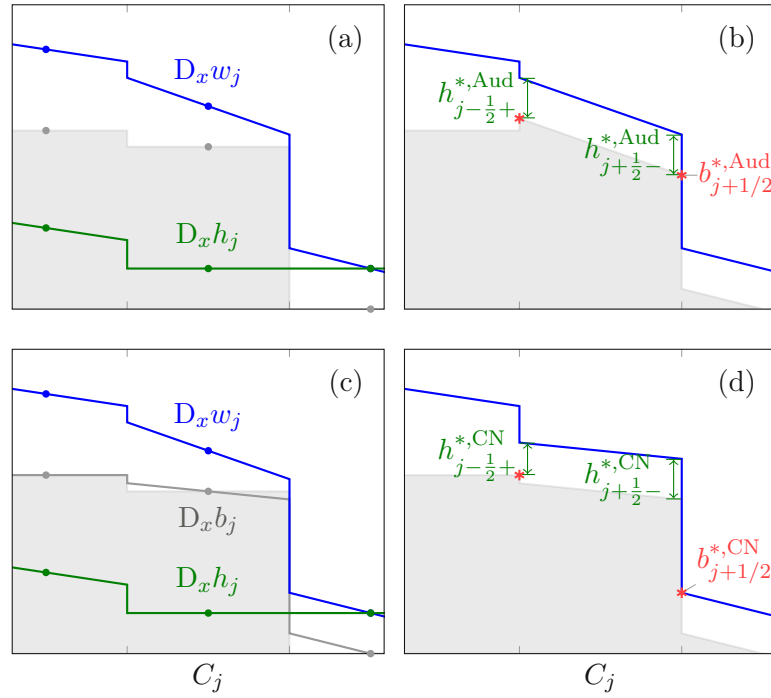$$

The procedure is visualized in Figure 2.3a,b.

Fig. 2.3. Second-order reconstruction for partially wet cells. a) From the cell centered values (marked with dots), slopes for the water depth and water levels and are derived in the scheme of Audusse et al. b) Then, the bottom slope and HR point values are reconstructed. c) For the BHNW scheme, we additionally reconstruct the bottom slope if interfaces are partially wet. d) In this case, the water level slope is recomputed from the water depth and bottom slope and used to derive the HR bottom values (red asterisks). We see that the left HR interface depth $h^*_{j-1/2+}$ differs in the two second-order HR reconstructions.

"Adaptive" second-order hydrostatic reconstruction

We introduce a new second-order reconstruction in combination with the recent hydrostatic reconstruction introduced by Chen and Noelle (2017). We propose a reconstruction that is additionally based on bottom values in case of "large" discontinuities in bathymetry and water levels, as explained for the x-dimension in the following paragraph. If we might land in a "partially wet" situation, i. e.

$$w_{j-\frac{1}{2}+,k} - h_{j-\frac{1}{2}+,k} > w_{j-1,k} \text{ or } w_{j+\frac{1}{2}-,k} - h_{j+\frac{1}{2}-,k} > w_{j+1,k}, \tag{2.23}$$

then, at this cell, we check if the bottom slope

$$\mathrm{D}_x b_{j,k} = \mathrm{minmod}\left(\theta \frac{b_{j,k} - b_{j-1,k}}{\Delta x}, \frac{b_{j+1,k} - b_{j-1,k}}{2\Delta x}, \theta \frac{b_{j+1,k} - b_{j,k}}{\Delta x}\right). \tag{2.24}$$

is greater than the water level slope $\mathrm{D}_x w_{j,k}$. If the conditions

$$|\mathrm{D}_x w_{j,k}| > |\mathrm{D}_x b_{j,k}| \tag{2.25}$$

14

and (2.23) hold, we reset the water level slope

$$D_x w_{j,k} = D_x h_{j,k} + D_x b_{j,k}. \tag{2.26}$$

We proceed by recalculating the second-order water level point values (2.15). Condition (2.25) ensures a correct treatment at partially wet cells and at wet-dry regions of an advancing wave front on a sloped bottom. We remark that the bottom slopes, e. g., $D_x b_{j,k}$ in (2.24), can be precomputed for time-independent bathymetry values.

Then, we derive a second-order HR bottom value per interface,

$$
\begin{aligned}
b^{*,\text{CN}}_{j-\frac{1}{2},k} &= \min\left(b^{*,\text{Aud}}_{j-\frac{1}{2},k}, \min(w_{j-\frac{1}{2}+,k}, w_{j-\frac{1}{2}-,k})\right), \\
b^{*,\text{CN}}_{j+\frac{1}{2},k} &= \min\left(b^{*,\text{Aud}}_{j+\frac{1}{2},k}, \min(w_{j+\frac{1}{2}+,k}, w_{j+\frac{1}{2}-,k})\right)
\end{aligned}
\tag{2.27}
$$

from the water level point values (2.15) and Audusse's HR bottom values $b^{*,\text{Aud}}$ (2.21), which are also depending on the water level point values. We set the second-order HR left and right interface depth values h^* to

$$
\begin{aligned}
h^{*,\text{CN}}_{j-\frac{1}{2}+,k} &= \min(w_{j-\frac{1}{2}+,k} - b^{*,\text{CN}}_{j-\frac{1}{2},k}, h_{j-\frac{1}{2}+,k}), \\
h^{*,\text{CN}}_{j+\frac{1}{2}-,k} &= \min(w_{j+\frac{1}{2}-,k} - b^{*,\text{CN}}_{j+\frac{1}{2},k}, h_{j+\frac{1}{2}-,k}),
\end{aligned}
\tag{2.28}
$$

using the water depth (2.14) and level (2.15) point values, see also Figure 2.3c,d. Equations (2.27) and (2.28) are the second-order analogs to equations (2.9) and (2.10). The HR reconstructed depth values (2.28) and (2.22) agree in cells where either condition (2.23) or condition (2.25) is not true for the cell itself and all neighboring cells. In general, our HR interface point values do not agree with the original HR interface point values, compare Figure 2.3.

This adaptive reconstruction strategy is necessary, since a naive second-order reconstruction can not be applied to all cells as in the vicinity of strong bottom jumps a back wave might emerge at the top of the step. This unphysical behavior is caused by an unphysical bottom reconstruction in the upper cell of the bottom jump.

We conclude this section with properties of the HR interface depth values. Since the reconstruction operator obeys the maximum principle for $\theta \leq 2$, particularly $h_{j-\frac{1}{2}+,k}, h_{j+\frac{1}{2}-,k} \geq \min(h_{j-1,k}, h_{j,k}, h_{j+1,k}) \geq 0$, the second-order reconstructed interface depths $h_{j+\frac{1}{2}-,k}$ are nonnegative by construction, see (2.12) and (2.14). Since furthermore in any case the water levels are greater than the reconstructed bathymetry, e. g., $w_{j+\frac{1}{2}-,k} \geq b^*_{j+\frac{1}{2},k}$, the reconstructed HR water depths fulfill

$$0 \leq h^*_{j+\frac{1}{2}\pm,k} \leq h_{j+\frac{1}{2}\pm,k}, \quad 0 \leq h^*_{j,k+\frac{1}{2}\pm} \leq h_{j,k+\frac{1}{2}\pm}, \tag{2.29}$$

for all interfaces $I_{j+1/2,k}$ and $I_{j,k+1/2}$.

2.2.5 Source terms

We revisit the bathymetry source term $\mathbf{S}$ in a cell $C_{j,k}$ for the second-order HR scheme of Audusse et al. (2004). Clearly, the depth source term $\mathbf{S}^h$ is zero, i.e.

$$\mathbf{S}^h_{j,k} = 0. \tag{2.30}$$

The momentum source terms $\mathbf{S}^{hu}$ and $\mathbf{S}^{hv}$ are split into interface parts and a centered part $\hat{\mathbf{S}}_{j,k}$, i.e.

$$\mathbf{S}^{hu}_{j,k} = \mathbf{S}^{hu}_{j-\frac{1}{2}+,k} + \mathbf{S}^{hu}_{j+\frac{1}{2}-,k} + \hat{\mathbf{S}}^{hu}_{j,k}, \tag{2.31}$$

$$\mathbf{S}^{hv}_{j,k} = \mathbf{S}^{hv}_{j,k-\frac{1}{2}+} + \mathbf{S}^{hv}_{j,k+\frac{1}{2}-} + \hat{\mathbf{S}}^{hv}_{j,k}. \tag{2.32}$$

The centered source terms read

$$\hat{\mathbf{S}}^{\mathrm{Aud},hu}_{j,k} = -\frac{g}{\Delta x} \frac{h_{j+\frac{1}{2}-,k} + h_{j-\frac{1}{2}+,k}}{2} (b_{j+\frac{1}{2}-,k} - b_{j-\frac{1}{2}+,k}) \tag{2.33}$$

$$\hat{\mathbf{S}}^{\mathrm{Aud},hv}_{j,k} = -\frac{g}{\Delta y} \frac{h_{j,k+\frac{1}{2}-} + h_{j,k-\frac{1}{2}+})}{2} (b_{j,k+\frac{1}{2}-} - b_{j,k-\frac{1}{2}+}). \tag{2.34}$$

ensure second-order consistency in regions where the solution is smooth. If the solution is varying a lot, the source term is distributed towards the interfaces (Bouchut, 2007). The interface terms are only described for the x-dimension, all the steps are repeated analogously in y-dimension for $\mathbf{S}^{hv}_{j,k-\frac{1}{2}+}$ and $\mathbf{S}^{hv}_{j,k+\frac{1}{2}-}$. The interface source terms in the second-order HR scheme (Audusse et al., 2004) are given as

$$
\begin{aligned}
\mathbf{S}^{\mathrm{Aud},hu}_{j-\frac{1}{2}+,k} &= -\frac{g}{\Delta x} \frac{h_{j-\frac{1}{2}+,k} + h^{*,\mathrm{Aud}}_{j-\frac{1}{2}+,k}}{2} \left(h_{j-\frac{1}{2}+,k} - h^{*,\mathrm{Aud}}_{j-\frac{1}{2},k} \right), \\
\mathbf{S}^{\mathrm{Aud},hu}_{j+\frac{1}{2}-,k} &= -\frac{g}{\Delta x} \frac{h^{*,\mathrm{Aud}}_{j+\frac{1}{2}-,k} + h_{j+\frac{1}{2}-,k}}{2} \left(h^{*,\mathrm{Aud}}_{j+\frac{1}{2},k} - h_{j+\frac{1}{2}-,k} \right).
\end{aligned}
\tag{2.35}
$$

The smoother the solution, the smaller the differences of the variables across the interfaces. Thus the source term is mostly influenced by the cell centered source term. However, since the source terms (2.35) only depend on the smoothness of the water level w and depth h, discontinuities in the bottoms might be interpreted only as a centered source term reflecting the water level slope (Figure 2.4).

We approximate the source term without a centered source term (Hou et al., 2013a; Hou et al., 2013b), i.e.

$$\mathbf{S}^{hu}_{j,k} = \mathbf{S}^{hu}_{j-\frac{1}{2}+,k} + \mathbf{S}^{hu}_{j+\frac{1}{2}-,k}, \tag{2.36}$$

$$\mathbf{S}^{hv}_{j,k} = \mathbf{S}^{hv}_{j,k-\frac{1}{2}+} + \mathbf{S}^{hv}_{j,k+\frac{1}{2}-}, \tag{2.37}$$
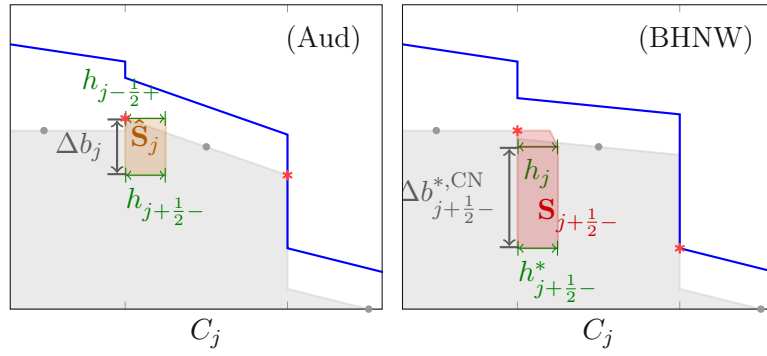
Fig. 2.4. The second-order reconstruction of Audusse et al. leads only to a centered source term $\hat{\mathbf{S}}_j$ (yellow) in the upper cell, as the HR bottom values (red asterisks) agree with the second-order bottom values. In contrast, in our proposed BHNW scheme, interface source terms appear in the upper cell, where the right subcell source term labeled $\mathbf{S}_{j+1/2-}$ accounts for the right bottom jump. The source terms are visualized as trapezoids based on the water depths and the difference $\Delta b_j = b_{j+1/2-} - b_{j-1/2+}$ of the second-order bottom values for the centered term, or, the difference $\Delta b_{j+1/2-}^{*,\mathrm{CN}} = b_{j+1/2}^{*,\mathrm{CN}} - b_j$ between reconstructed and cell-centered bottom value for the interface term.

where the left and right interface source term is given by

$$
\begin{aligned}
\mathbf{S}_{j-\frac{1}{2}+,k}^{hu} &= -\frac{g}{\Delta x} \frac{h_{j,k} + h_{j-\frac{1}{2}+,k}^{*,\mathrm{CN}}}{2} \left(b_{j,k} - b_{j-\frac{1}{2},k}^{*,\mathrm{CN}} \right), \\
\mathbf{S}_{j+\frac{1}{2}-,k}^{hu} &= -\frac{g}{\Delta x} \frac{h_{j+\frac{1}{2}-,k}^{*,\mathrm{CN}} + h_{j,k}}{2} \left(b_{j+\frac{1}{2},k}^{*,\mathrm{CN}} - b_{j,k} \right).
\end{aligned}
\tag{2.38}
$$

and analogously for $\mathbf{S}_{j,k}^{hv}$. The simple approximation slightly reduces the computational burden and is easier to implement. The difference between the two source term approximations is visualized in Figure 2.5 for fully wet cells. We remark that our source term treatment consisting of (2.36), (2.37) and (2.38) also leads to differences in wet regions, when compared to the original HR method (Audusse et al., 2004).

A similar approximation of the source term without the centered part can also be found in the works of Hou et al. (Hou et al., 2013a; Hou et al., 2013b) with the following source terms $\mathbf{S}_{j-\frac{1}{2}+,k}^{hu}, \mathbf{S}_{j+\frac{1}{2}-,k}^{hu}$ in (2.36) and (2.36)

$$
\begin{aligned}
\mathbf{S}_{j-\frac{1}{2}+,k}^{\mathrm{Hou},hu} &= -\frac{g}{\Delta x} \frac{h_{j,k} + h_{j-\frac{1}{2}+,k}^{*,\mathrm{Aud}}}{2} \left(b_{j,k} - b_{j-\frac{1}{2}+,k}^{*,\mathrm{Hou}} \right), \\
\mathbf{S}_{j+\frac{1}{2}-,k}^{\mathrm{Hou},hu} &= -\frac{g}{\Delta x} \frac{h_{j+\frac{1}{2}-,k}^{*,\mathrm{Aud}} + h_{j,k}}{2} \left(b_{j+\frac{1}{2}-,k}^{*,\mathrm{Hou}} - b_{j,k} \right).
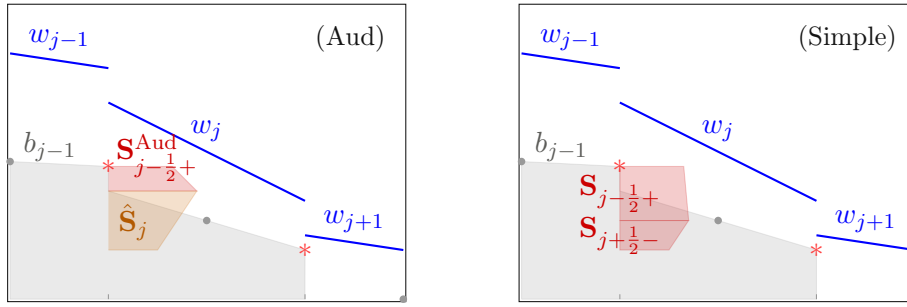\end{aligned}
\tag{2.39}
$$

Fig. 2.5. Approximation of second order source terms as in Audusse et al. (Aud) or simply by two interface source terms, visualized in one spatial dimension. The images show the difference of the source term approximation $\mathbf{S}^{\text{Aud}}_{j-1/2+} + \hat{\mathbf{S}}_j$ of Audusse et al. and the simple approximation $\mathbf{S}_{j-1/2+} + \mathbf{S}_{j+1/2-}$. In this case, $\mathbf{S}^{\text{Aud}}_{j+1/2-} = 0$.

In the robust and simple scheme of Hou et al. (Hou et al., 2013a; Hou et al., 2013b) only the bed elevations at the lower side are modified resulting in different bottom values at the left and the right interface to maintain well-balancedness, i. e.

$$b^{*,\text{Hou}}_{j-\frac{1}{2}+,k} = \min(b^{*,\text{Aud}}_{j-\frac{1}{2},k}, w_{j-\frac{1}{2}+,k}), \quad b^{*,\text{Hou}}_{j+\frac{1}{2}-,k} = \min(b^{*,\text{Aud}}_{j+\frac{1}{2},k}, w_{j+\frac{1}{2}-,k}). \tag{2.40}$$

Thus, there is no acceleration in the upper cell's source terms coming from the bed slope. Thus, as in the scheme of Audusse et al. (2004), it does not fully account for bathymetry steps at shallow flow conditions. If in two adjacent cells there is shallow flow and we are in a partially wet situation (2.23), then the simple source term approximation of Hou et al. neglects the difference $\underline{w}_{j+1/2,k} - b^{*,\text{Aud}}_{j+1/2,k}$. Thus, the contribution of the bottom jump to the source term at the upper cell is neglected, in contrast to our approach. This is further highlighted in a numerical experiment, see Section 2.3.1.

2.2.6 Numerical fluxes

The discretized fluxes are obtained through an approximate Riemann solver, the HLL flux $\mathcal{F}_{\text{HLL}}$ (Harten et al., 1983). The hydrostatically reconstructed interface point values $\mathbf{U}^* = [h^*, h^*u, h^*v]^T$, consisting of the HR depth h^* (2.28) and the HR reconstructed discharges, i. e., the reconstructed velocities u (2.18), v (2.19) times the HR depth h^*, are used as Riemann states for the numerical flux

$$\begin{aligned}
\mathbf{F}_{j+\frac{1}{2},k} &= \mathcal{F}_{\text{HLL}}(\mathbf{U}^*_{j+\frac{1}{2}-,k}, \mathbf{U}^*_{j+\frac{1}{2}+,k}) \\
&= \frac{\sigma^+_{j+\frac{1}{2},k}\mathbf{F}\left(\mathbf{U}^*_{j+\frac{1}{2}-,k}, b_{j+\frac{1}{2},k}\right) - \sigma^-_{j+\frac{1}{2},k}\mathbf{F}\left(\mathbf{U}^*_{j+\frac{1}{2}+,k}, b_{j+\frac{1}{2},k}\right)}{\sigma^+_{j+\frac{1}{2},k} - \sigma^-_{j+\frac{1}{2},k}} \\
&\quad + \frac{\sigma^+_{j+\frac{1}{2},k}\sigma^-_{j+\frac{1}{2},k}}{\sigma^+_{j+\frac{1}{2},k} - \sigma^-_{j+\frac{1}{2},k}}\left(\mathbf{U}^*_{j+\frac{1}{2}+,k} - \mathbf{U}^*_{j+\frac{1}{2}-,k}\right).
\end{aligned} \tag{2.41}$$

The nonnegative and nonpositive speed values $\sigma^+_{j+\frac{1}{2},k}$ and $\sigma^-_{j+\frac{1}{2},k}$ are functions of the eigenvalues λ of the Jacobian of the flux $\mathbf{F}$ at the interface $I_{j+\frac{1}{2},k}$, i.e.

$$
\begin{aligned}
\sigma^+_{j+\frac{1}{2},k} &= \max\left(\lambda^+_{j+\frac{1}{2}-,k}, \lambda^+_{j+\frac{1}{2}+,k}, 0\right) \\
&= \max\left(u_{j+\frac{1}{2}-,k} + \sqrt{gh^*_{j+\frac{1}{2}-,k}},\ u_{j+\frac{1}{2}+,k} + \sqrt{gh^*_{j+\frac{1}{2}+,k}},\ 0\right).
\end{aligned}
\tag{2.42}
$$

$$
\sigma^-_{j+\frac{1}{2},k} = \min\left(u_{j+\frac{1}{2}-,k} - \sqrt{gh^*_{j+\frac{1}{2}-,k}},\ u_{j+\frac{1}{2}+,k} - \sqrt{gh^*_{j+\frac{1}{2}+,k}},\ 0\right)
\tag{2.43}
$$

Analogously, speed values in y-direction can be derived from the Jacobian of the flux in y-dimension $\mathbf{G}$. We remark that the HLL flux is consistent, i.e. $\mathcal{F}_{\mathrm{HLL}}(\mathbf{U}, \mathbf{U}) = \mathbf{F}(\mathbf{U})$ and with the given choices for the speeds it is also able to handle dry states.

The HLL flux is remarkable robust, however, it is known that the HLL flux does not resolve shear waves accurately as it ignores the contact discontinuity of the transverse velocity (Toro, 2001). One way to fix this issue is to include the middle wave, which leads to the Harten–Lax–van Leer-contact (HLLC) flux. To preserve the nonnegativity of the water depths and to satisfy a discrete entropy inequality, additional sub-characteristic conditions have to be satisfied (Bouchut, 2007). It is possible to approximate the HLLC flux with a simplified version, i.e.,

$$
\mathcal{F}^{hv}_{j+\frac{1}{2}-,k} = \begin{cases} v_j\,\mathcal{F}^h_{j+\frac{1}{2}-,k} & \text{if } \mathcal{F}^h_{j+\frac{1}{2}-,k} \geq 0, \\ v_{j+1}\,\mathcal{F}^h_{j+\frac{1}{2}-,k} & \text{otherwise.} \end{cases}
\tag{2.44}
$$

Other choices for the ARS include the Roe solver. Although the Roe solver is more accurate than the HLL flux, it has difficulties with dry beds. The handling of dry beds is often incorporated by imposing internal boundary conditions, which adds complexity to schemes using the Roe solver (Castro et al., 2005; Murillo and García-Navarro, 2012; Murillo and Navas-Montilla, 2016; Parés and Pimentel, 2019). Moreover, at transcritical rarefactions, i.e., if the left or right eigenvalue is close to zero, an entropy fix is needed (Harten and Hyman, 1983; LeVeque, 1992). Thus, the Roe solver is a priori less robust and requires an additional parameter, which decides if speeds are close to zero and thus considered for a transcritical rarefaction fix (Toro, 2001).

2.2.7 Time integration

For first-order time integration, an explicit Euler is used, i.e.

$$
\mathbf{U}^{n+1}_{j,k} = \mathbf{U}^n_{j,k} + \Delta t\, \mathbf{R}(\mathbf{U}^n)_{j,k},
\tag{2.45}
$$

where

$$
\mathbf{R}(\mathbf{U}^n)_{j,k} = \mathbf{S}^n_{j,k} - \frac{\mathbf{F}^n_{j+\frac{1}{2},k} - \mathbf{F}^n_{j-\frac{1}{2},k}}{\Delta x} - \frac{\mathbf{G}^n_{j,k+\frac{1}{2}} - \mathbf{G}^n_{j,k-\frac{1}{2}}}{\Delta y}.
\tag{2.46}
$$

Quantities denoted by a superscript n depend on the state $\mathbf{U}^n \approx \mathbf{U}(t_n)$.

The CFL condition restricts the time step $\Delta t_n = t_{n+1} - t_n$ and is given by

$$\Delta t_n \leq \text{CFL} \cdot \min\left(\frac{\Delta x}{\sigma_x^n}, \frac{\Delta y}{\sigma_y^n}\right), \tag{2.47}$$

where σ_x^n and σ_y^n represent the maximum wave speeds in x- and y-direction at time t_n. They are computed by a reduction over all interface wave speeds given by the absolute values of (2.42) and (2.43). The CFL constant has to be positive and is not allowed to be greater 0.25 to ensure the positivity of the two-dimensional second-order accurate FV scheme, as we show in Section 2.2.8.

Heun's method is used for second-order time integration. By denoting intermediate states with an asterisk, the state $\mathbf{U}^{n+1}$ at time t_{n+1} is given by

$$\mathbf{U}^{*,n+1} = \mathbf{U}^n + \Delta t \mathbf{R}(\mathbf{U}^n), \tag{2.48}$$

$$\mathbf{U}^{*,n+2} = \mathbf{U}^{*,n+1} + \Delta t \mathbf{R}(\mathbf{U}^{*,n+1}) \tag{2.49}$$

$$\mathbf{U}^{n+1} = \frac{1}{2}\left(\mathbf{U}^n + \mathbf{U}^{*,n+2}\right) = \frac{1}{2}\left(\mathbf{U}^n + \mathbf{U}^{*,n+1}\right) + \frac{\Delta t}{2}\mathbf{R}(\mathbf{U}^{*,n+1}) \tag{2.50}$$

where the residual $\mathbf{R}(\mathbf{U})$ is defined according to (2.46). Clearly, by (2.50), the intermediate state $\mathbf{U}^{*,n+2}$ does not need to be explicitly calculated. The solution $\mathbf{U}$ is updated dimension-wise. First, we compute reconstructed values, fluxes and sources in x-dimension. Second, we perform the computations in y-dimension. Afterwards we update the solution with the combined residual.

2.2.8 Positivity preserving

Our scheme preserves the nonnegativity of the water depths, i.e.

$$h_{j,k}^n \geq 0 \Rightarrow h_{j,k}^{n+1} \geq 0, \tag{2.51}$$

under a certain CFL condition.

Following (Audusse et al., 2004), we require that the homogeneous flux $\mathcal{F}$ preserves the nonnegativity of the water depths h *by interface* with numerical speeds $\sigma^+(U_i, U_{i+1}) \geq 0$ and $\sigma^-(U_i, U_{i+1}) \leq 0$, which means that whenever the CFL condition

$$0 \leq \sigma(U_i, U_{i+1})\Delta t \leq \Delta x \tag{2.52}$$

with

$$\sigma(U_i, U_{i+1}) = \max(-\sigma^-(U_i, U_{i+1}), \sigma^+(U_i, U_{i+1})) \tag{2.53}$$

holds, we have

$$h_i - \frac{1}{\sigma^-(U_i, U_{i+1})}\left(\mathcal{F}^h(U_i, U_{i+1}) - h_i u_i\right) \geq 0, \tag{2.54}$$

$$h_{i+1} - \frac{1}{\sigma^+(U_i, U_{i+1})}\left(\mathcal{F}^h(U_i, U_{i+1}) - h_{i+1} u_{i+1}\right) \geq 0. \tag{2.55}$$

The HLL flux preserves nonnegative water heights by interface, e.g., it fulfills (2.54) and (2.55), for the specified numerical speeds σ^+, σ^- in (2.42) and (2.43), respectively (Bouchut, 2007).

The new second-order scheme guarantees nonnegative water depth for the SWEs (2.1) under condition (2.47) with the CFL number being halved when compared to the CFL condition needed for a positivity-preserving first-order scheme associated with the homogeneous problem, e.g., the HLL scheme. This statement can be proved similarly as in Audusse et al. (2004), Audusse and Bristeau (2005), and Bouchut (2004). The positivity follows from the facts that the reconstructed depths are nonnegative (2.22) and that the chosen second-order time integration is a convex combination of two first-order time steps.

The two-dimensional scheme

$$h_{j,k}^{n+1} = h_{j,k}^n - \frac{\Delta t}{\Delta x} \left(\mathbf{F}_{j+\frac{1}{2},k}^{h,n} - \mathbf{F}_{j-\frac{1}{2},k}^{h,n} \right) - \frac{\Delta t}{\Delta y} \left(\mathbf{G}_{j,k+\frac{1}{2}}^{h,n} - \mathbf{G}_{j,k-\frac{1}{2}}^{h,n} \right), \qquad (2.56)$$

is positivity-preserving under half the CFL condition needed for the positivity-preserving one-dimensional scheme. Thus, by choosing a positive CFL constant not greater than 0.25 we obtain a positivity-preserving two-dimensional second-order scheme. We remark that the different source treatment does not have any influence on the preservation of nonnegative states. Furthermore, the numerical speed of the HR schemes is not higher than the one of the associated homogenous scheme, since the numerical speed is a monotone function of the water depth h, see (2.42),(2.43).

2.2.9 Well-Balancedness

We show well-balancedness in two steps. First, for the still-water steady state and, second, for the lake at rest steady state involving wet-dry boundaries. We remark that since our proposed scheme does not couple dimensions for the flux and source terms, it is enough to show well-balancedness dimension-wise. In fact, each interface can be associated with a subcell for which we will show well-balancedness. We will use the following convex decomposition of the residuum

$$\mathbf{R}_{j,k} = \mathbf{R}_{j-\frac{1}{2}+,k} + \mathbf{R}_{j+\frac{1}{2}-,k} + \mathbf{R}_{j,k-\frac{1}{2}+} + \mathbf{R}_{j,k+\frac{1}{2}-}, \qquad (2.57)$$

where

$$\mathbf{R}_{j-\frac{1}{2}+,k} = -\frac{1}{\Delta x} \left(\mathbf{F}_{j,k} - \mathbf{F}_{j-\frac{1}{2},k} \right) + \mathbf{S}_{j-\frac{1}{2}+,k} \qquad (2.58)$$

with analogous definitions for the other subcells.

In the still water situation, we have $\nabla w = 0$ and $hu, hv = 0$ and we analyse the nontrivial case $h > 0$. In this case, all cells are fully wet and the reconstructed interface bottom levels and water depths agree with the ones defined by Audusse et al. (2004). For a cell $C_{j,k}$, we will show that the left residuum $\mathbf{R}_{j-\frac{1}{2}+,k}$ (2.58) vanishes. For a constant water level W, which is preserved by our second-order

reconstruction, i.e. $w_{j-\frac{1}{2}+,k} = w_{j,k+\frac{1}{2}-} = w_{j,k-\frac{1}{2}+} = w_{j,k+\frac{1}{2}-} = W$ for all j,k, the HR left and right interface water depths are the same by (2.11). The depth and the y-discharge component of the residuum $\mathbf{R}_{j-1/2+,k}$ are zero because of the consistency of the flux and the absence of source terms. For the hu-fluxes, we have

$$\mathbf{F}^{hu}_{j-\frac{1}{2}+,k} = \mathbf{F}^{hu}(\mathbf{U}^*_{j\frac{1}{2}-,k}, \mathbf{U}^*_{j-\frac{1}{2}+,k}) = \frac{g}{2} h^{*,2}_{j+\frac{1}{2},k}, \tag{2.59}$$

and

$$\mathbf{F}^{hu}_{j,k} = \mathbf{F}^{hu}(\mathbf{U}_{j,k}) = \frac{g}{2} h^2_{j,k}. \tag{2.60}$$

by consistency of the HLL flux and since the water is at rest. Furthermore, we notice that

$$h_{j,k} - h^*_{j-\frac{1}{2}+,k} = W - b_{j,k} - (W - b^*_{j-\frac{1}{2}+,k}) = -(b_{j,k} - b^*_{j-\frac{1}{2}+,k}), \tag{2.61}$$

as the water level W is greater than the bathymetry, and use it to compute the left source term

$$\mathbf{S}^{hu}_{j-\frac{1}{2}+,k} = -\frac{g}{\Delta x} \frac{h_{j,k} + h^*_{j-\frac{1}{2}+,k}}{2} \left(b_{j,k} - b^*_{j-\frac{1}{2}+,k} \right) \tag{2.62}$$

$$= \frac{g}{2\Delta x} \left(h^2_{j,k} - h^{*,2}_{j-\frac{1}{2}+,k} \right). \tag{2.63}$$

Together, this shows

$$\mathbf{R}^{hu}_{j-1/2+,k} = 0. \tag{2.64}$$

The residuum vanishes also for all other subcells by the same reasons, yielding a vanishing cell residuum $\mathbf{R}_{j,k} = \mathbf{0}$. Thus, the new two-dimensional second-order scheme is well-balanced for the still-water steady state (2.3).

In the lake at rest situation, we have $h\nabla w = 0$ and $hu, hv = 0$. It is enough to show well-balancedness for wet-dry boundaries in one dimension, e.g., a dry-wet front (Figure 2.6), i.e. $h_{j,k} = 0, h_{j+1,k} > 0$ and $b_{j,k} > w_{j+1,k}$. For a dry-wet front $b_{j,k} = w_{j,k} > w_{j+1,k} = b_{j+1,k} + h_{j+1,k} > b_{j+1,k}$ holds. We have to show that the residuum

$$\mathbf{R}_{j,k} = -\frac{1}{\Delta x} \left(\mathbf{F}_{j+1/2,k} + \mathbf{F}_{j-1/2,k} \right) + \mathbf{S}_{j+1/2-,k} + \mathbf{S}_{j-1/2+,k} \tag{2.65}$$

in these cells vanishes, that is $\mathbf{R}_{j,k} = 0$ and $\mathbf{R}_{j+1,k} = 0$. At a wet-dry front, the bathymetry slope $\mathrm{D}_x b$ can only be greater or equal the water level slope $\mathrm{D}_x w$, thus condition (2.25) is not true, and we only need to consider water levels and depths as second-order reconstructed variables. The reconstructed water levels are still constant at wet cells. At the interface $I_{j+1/2,k}$, we observe that $b^*_{j+1/2,k} = w_{j+1,k}$ and $h_{j+1/2-,k} = 0$, therefore

$$h^*_{j+\frac{1}{2}+,k} = \min(w_{j+\frac{1}{2}+,k} - b^*_{j+\frac{1}{2},k}, h_{j+\frac{1}{2}+,k}) = \min(0, h_{j+\frac{1}{2}+,k}) = 0, \tag{2.66}$$

$$h^*_{j+\frac{1}{2}-,k} = \min(w_{j+\frac{1}{2}-,k} - b^*_{j+\frac{1}{2},k}, h_{j+\frac{1}{2}-,k}) = 0 \tag{2.67}$$
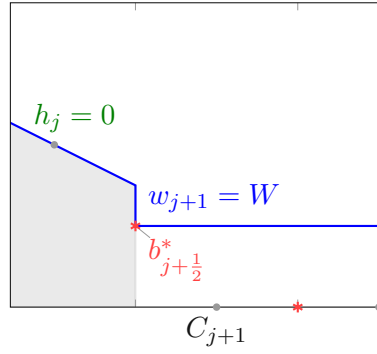
Fig. 2.6. Lake at rest. Visualization of a dry-wet boundary, i. e. $h_j = 0, h_{j+1} > 0$. The HR interface depth values $h^*_{j+1/2-}$ and $h^*_{j+1/2+}$ vanish. The HR interface bathymetry values b^* are marked with red asterisks.

holds, compare Figure 2.6. By consistency of the numerical flux, the numerical flux across the interface vanishes,

$$\mathbf{F}_{j+\frac{1}{2},k} = \mathcal{F}_{\mathrm{HLL}}(\mathbf{U}^*_{j+\frac{1}{2}-,k}, \mathbf{U}^*_{j+\frac{1}{2}+,k}) = \mathcal{F}_{\mathrm{HLL}}(\mathbf{0},\mathbf{0}) = \mathbf{0}. \tag{2.68}$$

Therefore, the residual $\mathbf{R}_{j,k}$ equals zero, since the cell depth $h_{j,k}$ and interface depths $h^*_{j-1/2+,k}$ and $h^*_{j+1/2-,k}$ are zero.

For cell $C_{j+1,k}$, we will use the convex decomposition of the residuum (2.57) where

$$\mathbf{F}^{hu}_{j+1,k} = \frac{g}{2}h^2_{j+1,k}, \tag{2.69}$$

since the water is at rest. As $h^*_{j+1/2+,k} = 0$, we have

$$\mathbf{S}^{hu}_{j+\frac{1}{2}+,k} = -\frac{g}{\Delta x}\frac{h_{j+1,k} + h^*_{j+\frac{1}{2}+,k}}{2}\left(b_{j+1,k} - b^*_{j+\frac{1}{2}+,k}\right), \tag{2.70}$$

$$= \frac{g}{2\Delta x}h^2_{j+1,k} = \frac{1}{\Delta x}\mathbf{F}^{hu}_{j+1,k}. \tag{2.71}$$

With $\mathbf{F}^{hu}_{j+1/2,k} = 0$ we conclude that $\mathbf{R}^{hu}_{j+1/2+,k} = 0$. For a completely wet right interface $I_{j+3/2,k)}$,

$$\mathbf{R}_{j+\frac{3}{2}-,k} = \mathbf{0} \tag{2.72}$$

holds, compare the proof of the previous theorem. However, if $C_{j+1,k}$ is degenerate, i. e., cell $C_{j+2,k}$ is dry, the second-order scheme falls back to first order, in which case well-balancedness follows from the first-order CN scheme. In this case, equation (2.72) also holds (Chen and Noelle, 2017). Thus, the residua $\mathbf{R}^{hu}_{j,k}$ in x-dimension vanish for all j, k. An adaptation of the previous arguments shows that the residua

$\mathbf{R}_{j,k}^{hv}$ in y-dimension vanish. By inspection of the flux terms, $\mathbf{R}_{j-\frac{1}{2}+,k}^{h} = \mathbf{R}_{j+\frac{1}{2}-,k}^{h} = 0$ for all interfaces in the lake-at-rest state Together, this shows that our novel scheme is well-balanced, also for the lake at rest steady state (2.4).

We remark that our scheme is well-balanced on a per-interface basis, thus this property holds also on unstructured grids if the second-order reconstruction keeps the water levels balanced.

2.2.10 Friction source terms

To provide realistic water flow, a friction term is introduced in the laboratory and real-world scenarios. The friction term $\mathbf{S}_f$ is included via an additional source term

$$\mathbf{S}_f(\mathbf{U}) = -gn^2 h^{-\frac{1}{3}} \begin{bmatrix} 0 \\ u\sqrt{u^2+v^2} \\ v\sqrt{u^2+v^2} \end{bmatrix}, \tag{2.73}$$

where n is the Manning roughness coefficient. It is evaluated in a semi-implicit manner by splitting the friction source term $\mathbf{S}_f$ into a coefficient-wise product of an implicitly evaluated state and an explicitly evaluated friction term $\widetilde{\mathbf{S}}_f$ (Brodtkorb et al., 2012)

$$\mathbf{S}_f(\mathbf{U}_{j,k}^{*,n+1}) \approx \mathbf{U}_{j,k}^{*,n+1} \widetilde{\mathbf{S}}_f(\mathbf{U}_{j,k}^n), \tag{2.74}$$

$$\mathbf{S}_f(\mathbf{U}_{j,k}^{n+1}) \approx \mathbf{U}_{j,k}^{n+1} \widetilde{\mathbf{S}}_f(\mathbf{U}_{j,k}^{*,n+1}). \tag{2.75}$$

where

$$\widetilde{\mathbf{S}}_f(\mathbf{U}) = -gn^2 h^{-\frac{4}{3}} \begin{bmatrix} 0 \\ \sqrt{u^2+v^2} \\ \sqrt{u^2+v^2} \end{bmatrix}. \tag{2.76}$$

Then, the integration from time t_n to t_{n+1} including friction is achieved by using the following explicit update of the states

$$\mathbf{U}^{*,n+1} = \frac{\mathbf{U}^n + \Delta t\, \mathbf{R}(\mathbf{U}^n)}{1 - \Delta t\, \widetilde{\mathbf{S}}_f(\mathbf{U}^n)}, \tag{2.77}$$

$$\mathbf{U}^{n+1} = \frac{1}{2} \frac{\mathbf{U}^n + \mathbf{U}^{*,n+1} + \Delta t\, \mathbf{R}(\mathbf{U}^{*,n+1})}{1 - \frac{\Delta t}{2}\, \widetilde{\mathbf{S}}_f(\mathbf{U}^{*,n+1})}, \tag{2.78}$$

instead of (2.48) and (2.50).

2.3 Validation

We validate the scheme on various test cases, a dam break over a step, the parabolic bump, seven Riemann problems, the parabolic basin (Thacker, 1981), the Malpasset

dam break event, and a historical flooding. Additionally, we verify the order of the scheme at the parabolic basin and the parabolic bump. In the following sections, we denote the scheme of Audusse et al. (2004) by Aud and the proposed second-order scheme by BHNW. The implementation of the scheme of Audusse et al. only differs in the HR, the adaptive second-order reconstruction and in the source term approximation. In particular, the generalised minmod slope limiter and the velocity reconstruction with a dry threshold was used for all schemes. The gravity constant g equals 9.81 in all our simulations, except for the parabolic basin where it is set to 2. The dry threshold ϵ_{dry} is set to 10^{-6} in the dam break and in the parabolic basin and to 10^{-4} in the Malpasset and Lobau. The experimental order of convergence EOC is defined as

$$EOC = \log_2\left(\frac{\|U_N - U\|}{\|U_{2N} - U\|}\right), \tag{2.79}$$

where U is the exact solution and U_N is the numerical approximation on a mesh with cell size $\Delta x \cdot \Delta y$, while U_{2N} is the numerical approximation on a mesh with half of the cell size, i.e. $\Delta x/2 \cdot \Delta y/2$. We use either the discrete L^1-norm of the water depth, or the maximum water depth difference, that is, the L^∞-norm.

2.3.1 Dam break over a dry step

We describe the setup for a dam break over a dry step, as specified in Chen and Noelle (2017) based on numerical experiments from Bollermann et al. (2013) and Castro et al. (2008). The difficulty lies in the correct approximation of the wet/dry front and the bottom step. As noted in the introduction, discontinuities in the bottom are outside the validity range of the SW model. However, bottom steps necessarily occur at the discrete level in FVMs and thus motivate this test. The quasi one-dimensional test is performed on a domain with range $[0, 1] \times [0, 0.01]$. The bottom topography b and the initial water depth h_0 is given by

$$b(x, y) = \begin{cases} -0.1 & \text{for } x < 0.1, \\ -0.45 & \text{otherwise,} \end{cases} \tag{2.80}$$

and

$$h_0(x, y) = \begin{cases} 0.5 & \text{for } x < 0.05, \\ 0 & \text{otherwise,} \end{cases} \tag{2.81}$$

respectively. We use a uniform cell size of 0.0025 m for the simulated values. The reference solution is computed on a grid with a cell size of 10^{-5} m and a piecewise linear step at $x = 0.1$ with 100 cells in the transition layer. The transition layer used for approximating the bottom step is thus 0.001 m wide.

We display the results at a final time $T = 0.18$ s in Figure 2.7. In this case, the scheme of Audusse et al. (2004) and the robust scheme of Hou et al. (2013a) produce nearly identical results. As already noted in Section 2.2.5, these two schemes neglect
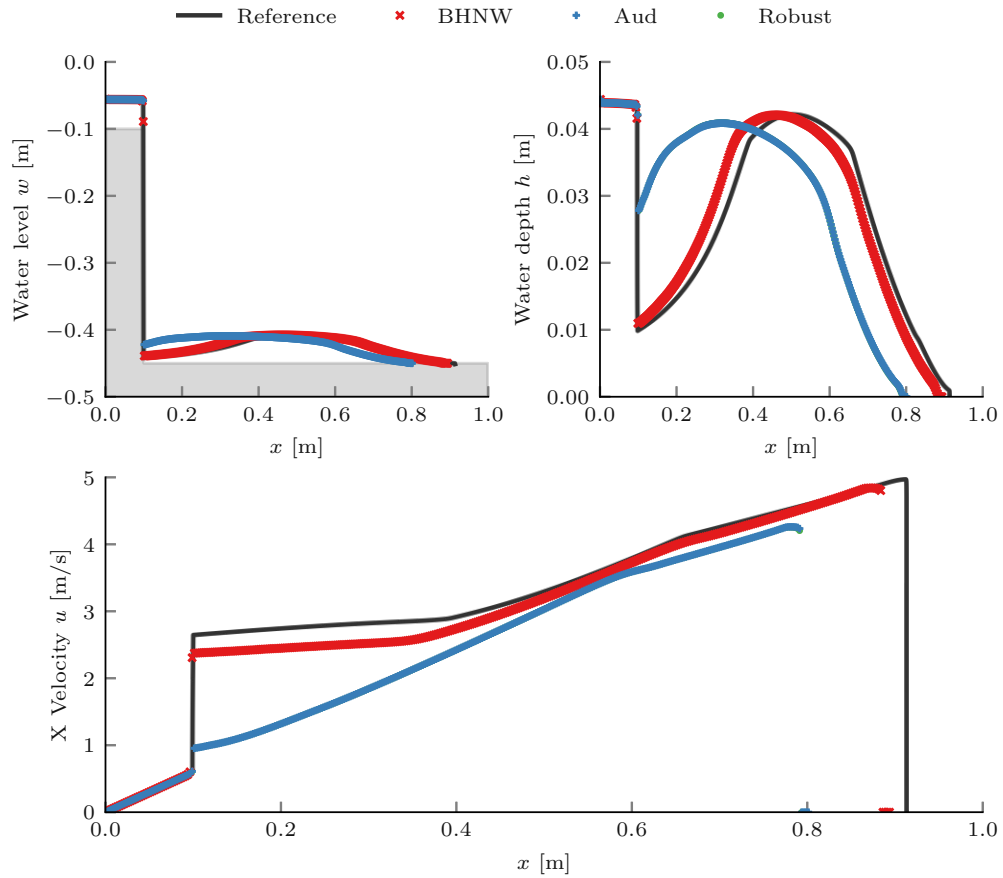
Fig. 2.7. Dam break over dry step. Water level, depth and velocity profile after 18 s. The new second-order scheme (BHNW) outperforms both the HR scheme of Audusse et al. (Aud) and the robust scheme of Hou et al. (Robust). The latter two schemes give nearly exactly the same results, thus the results of the robust scheme are hidden by those of Audusse et al. The reference solution is obtained with the first-order scheme of Audusse et al. on a finer grid with a 250 times smaller cell size and a continuous piecewise linear approximation of the bottom jump.
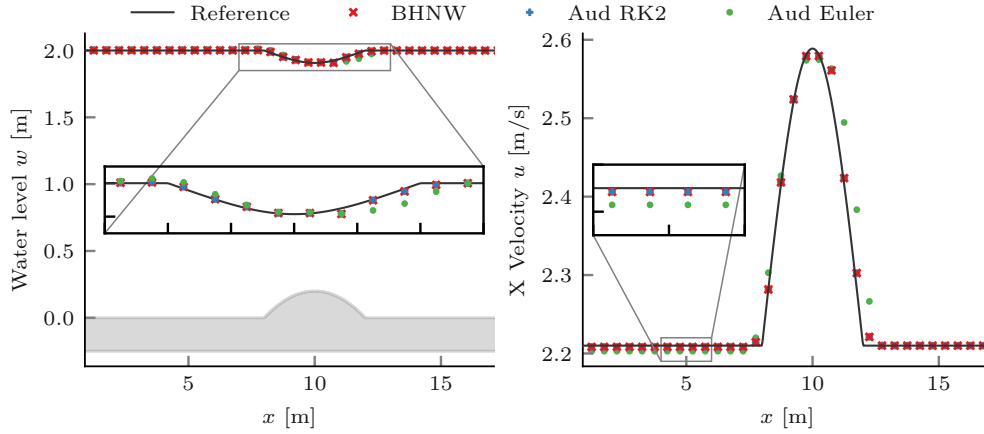
Fig. 2.8. Parabolic bump. Water level and velocity profiles for steady-state flow after 120 s. At a resolution of 0.5 m, the BHNW scheme shows visible differences from the analytical solution (Reference) in the vicinity of the bump edges and near the top of the bump. The first order Audusse scheme (Aud Euler) overestimates the water level and underestimates the velocities at the discharge inflow at the left of the bump. The second-order BHNW and Aud scheme (Aud RK2) produce nearly identical results in spite of the different source treatments.

the jump in the water levels at the interface, which leads to incorrect predictions of the velocities after the step. The improved HR method of the CN scheme together with the novel adaptive second-order reconstruction enables us to capture the water flow after the step accurately.

2.3.2 Parabolic bump

This section is devoted to show the performance of the scheme on a quasi one-dimensional steady-state test with a parabolic bump. The scenario is set up analogously to Audusse and Bristeau (2005) and Delestre et al. (2013) and is originally from Goutal and Maurel (1997). The analytical solutions for the steady states can be derived using the Bernoulli relation, see (Bouchut, 2007; Delestre et al., 2013). The bathymetry is given by

$$b(x,y) = \begin{cases} 0.2 - 0.05(x-10)^2 & \text{if } 8 < x < 12, \\ 0 & \text{else,} \end{cases} \tag{2.82}$$

for a domain of length L = 20 m and a width of 4 m (Figure 2.8).

In the case of subcritical flow, a discharge boundary condition (BC) is specified at the inflow $x = 0$ and a water level BC at the outflow $x = L$. The water depth is given by

$$h^3 + \left(b - \frac{q}{2gh_O} - h_O\right) h^2 + \frac{q^2}{2g} = 0, \tag{2.83}$$
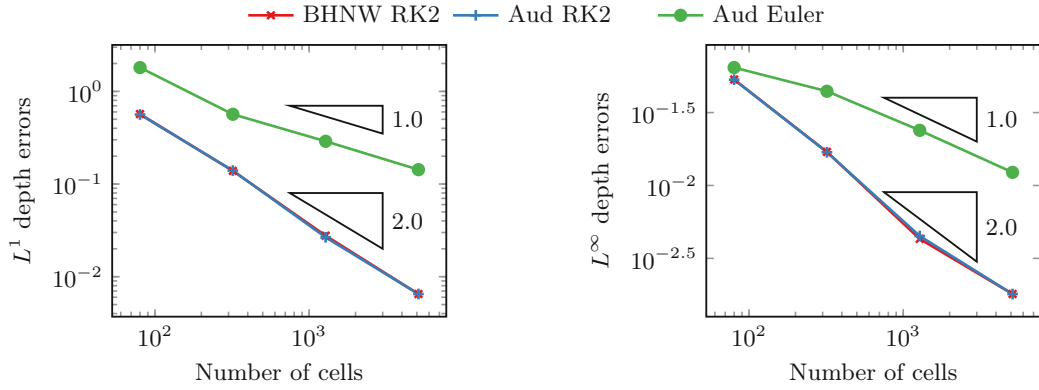
Fig. 2.9. Parabolic bump. Water depths error analysis for the proposed second-order BHNW scheme and the second-order scheme of Audusse et al. (Aud RK2) as well as for the first-order scheme of Audusse et al. (Aud Euler). The simple source treatment has a negligible effect on the accuracy, as the errors of the second-order scheme are nearly exactly the same.

Table 2.1. Parabolic bump. Water depths error analysis for the proposed second-order BHNW scheme and the second-order scheme of Audusse et al. (Aud RK2).

	BHNW RK2				Aud RK2		
Δx	L^1 Error	L^1 EOC	L^∞ Error	Δx	L^1 Error	L^1 EOC	L^∞ Error
1	0.5688		0.0533	1	0.5633		0.0532
0.5	0.1388	2.04	0.0170	0.5	0.1398	2.39	0.0169
0.25	0.0277	2.32	0.0043	0.25	0.0266	2.40	0.0045
0.125	0.0065	2.16	0.0018	0.125	0.0065	1.97	0.0018

where $h_O = w_O = 2$ m is the water depth at the outflow boundary. The discharge in x-direction is specified as $q = 4.42 \ \mathrm{m}^2/\mathrm{s}$ at the left inflow boundary. Water levels and velocities are shown in Figure 2.8 for a cell size of 0.5 m. Since in this setup all cells are always flooded, the CN HR falls back to the original HR and thus the first-order Audusse scheme agrees with the CN scheme. The BHNW scheme with simple source term produces results nearly identical to the ones of the second-order schemes of Audusse et al. (Aud RK2). This is also visible in Table 2.1, showing that the simple source treatment has only a very small effect on the accuracy. Due to the increased diffusivity in first-order schemes, the water levels at the discharge inflow are underestimated (right zoom-in in Figure 2.8). An error analysis for a range of cell sizes starting from 1 m down to 0.125 m shows that the schemes are second-order accurate in the smooth subcritical flow regime (Figure 2.9).

2.3.3 Riemann problems

We test the scheme on several RPs including resonant cases. All RPs are defined on the domain $[-1, 1]$ and by an initial state U_0 consisting of a left state $U_L = (h_L, u_L)$

Table 2.2. Investigated Riemann problems. Initial left and right Riemann states including bottom levels.

RP	h_L	h_R	u_L	u_R	b_L	b_R
1	4.0	0.50537954	0.1	0.0	0.0	1.5
2	1.5	0.16664757	2.0	0.0	0.0	2.0
3	0.3	0.4	2.0	2.2	1.1	1.0
4	1.0	0.8	2.0	4.0	1.1	1.0
5	0.75	1.0	0.0	0.0	1.0	0.0
6	0.1	0.05	0.1	0.4	0.1	0.0
7	1.0	1.0	2.0	4.0	1.0	0.0
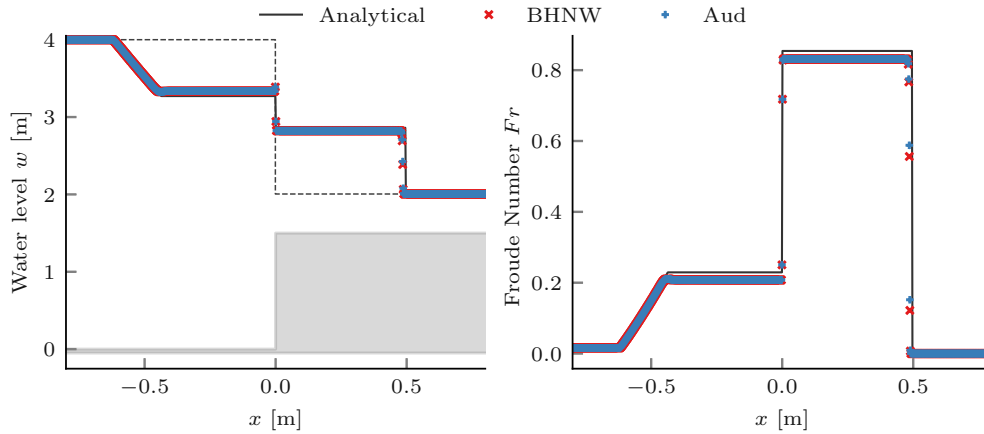
Fig. 2.10. Riemann problem 1. Dam break over a bottom step. Audusse and BHNW produce nearly the same results as all interfaces are fully wet. The results are in good agreement with the analytical solution.

with a left bottom level b_L for $x < 0$, and a right state $U_R = (h_R, u_R)$ with a right bottom level b_R for $x > 0$. The exact analytical solution is given by completing the SW system (2.1) with $\partial_t b = 0$ and connecting the resulting Riemann states. This extended inhomogenenous system shows a rich solution pattern. In fact, the RP may have no, a unique, or multiple solutions, depending on the given states and the bottom jump (Han and Warnecke, 2014; LeFloch and Thanh, 2007; LeFloch and Thanh, 2011). We restrict ourselves to cases with a unique solution. The investigated setups are listed in Table 2.2. All of them result in a flow from left to right at the bottom jump. The analytical solution is computed as outlined in Han and Warnecke (2014). All simulations are run until 0.1 s. The cell size is set to 0.002 m. We plot the water level and Froude number to emphasize the criticality of the flow states. In the plots, the gray area represents the bottom topography and the initial water level is marked with a thin dashed line. The x-axis limits are adapted to the RPs.

Riemann problem 1 (Figure 2.10) is a dam break over a bottom jump. The solution consists of a left rarefaction wave, a stationary shock associated with the
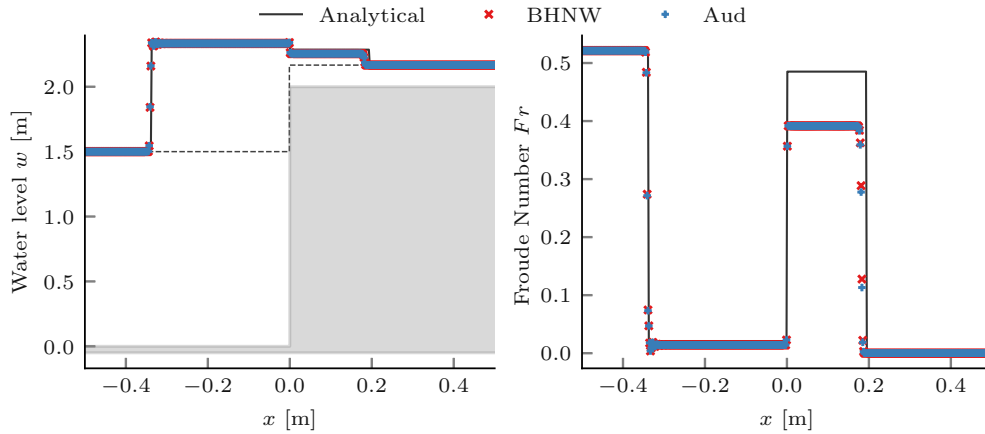
Fig. 2.11. Riemann problem 2. Subcritical flow onto a partially-wet bottom step. Both schemes produce acceptable results, however, they are not able to converge to the analytical solution.

bottom jump and a right shock. As all interfaces are fully wet, the combination of adaptive reconstruction and different source treatment does not have any visible effect. Therefore, the second-order Audusse scheme produces almost exactly the same results as the BHNW scheme, both are in good agreement with the analytical solution.

Riemann problem 2 (Figure 2.11) is a two shock case over a bottom jump. In this case, all interface are fully wet after 0.002 s and therefore the second-order Audusse scheme again produces almost exactly the same results as the BHNW scheme. However both schemes fail to accurately predict the state at the top of the bottom jump. These first two Riemann problems can also be found in Murillo and García-Navarro (2010) and Murillo and García-Navarro (2013).

In Riemann problem 3 (Figure 2.12), we test a supercritical regime over a downward bottom step. The state at the right of the bottom jump is also supercritical, it is not accurately captured by both the Audusse and the BHNW scheme. In Riemann problem 4 (Figure 2.13), we test a resonant regime over a small downward bottom step. In the resonance regime, the emerging solution pattern is quite complex and involves critical intermediate states or transcritical waves. As the stationary shock associated with a bottom jump is not allowed to cross the boundaries of strict hyperbolicity, the left-most wave has to be a rarefaction wave from the subcritical left state to a critical state. Then, this critical state connects via a stationary shock to the supercritical states at the right. Again, the supercritical state at the right of the bottom jump is not accurately captured by both schemes. RP 3 and RP 4 are taken from LeFloch and Thanh (2011).

In Riemann problem 5 (Figure 2.14), we test a dam break over a medium downward bottom step. The left-most wave is a rarefaction from the subcritical left state to a critical state, which then goes into a stationary hydraulic jump at the bottom
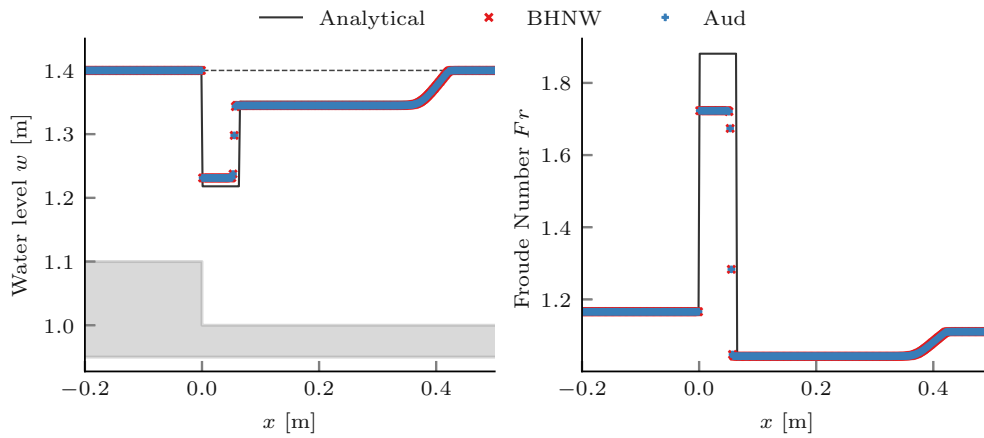
Fig. 2.12. Riemann problem 3. Supercritical regime over a small bottom step. All interfaces are wet, thus the Audusse scheme and the BHNW scheme produce nearly exactly the same solution. Both schemes are not able to converge to the analytical solution, but are in relatively good agreement with it.
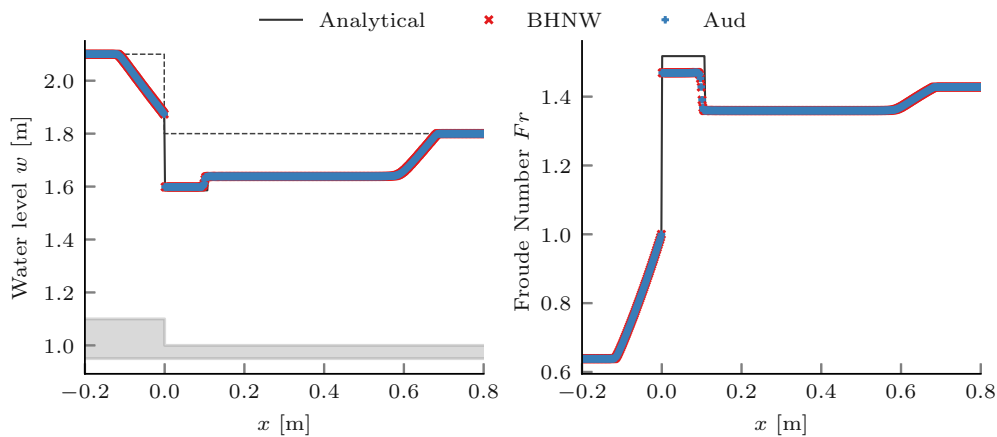

Fig. 2.13. Riemann problem 4. Resonant regime on a fully wet domain connecting a left subcritical state with a right supercritical state. Both schemes capture the complex emerging wave pattern. However they are not able to converge to the unique solution, but are close to it.
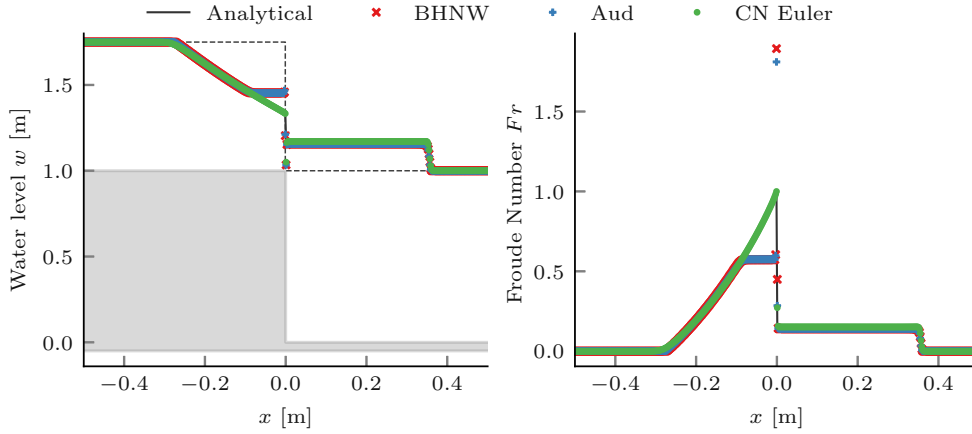
Fig. 2.14. Riemann problem 5. Dam break over a medium step. A hydraulic jump at the bottom discontinuity emerges. The second-order schemes fail to capture the left rarefaction wave in its whole entirety, while the first-order CN scheme is able to converge to the correct solution.

discontinuity. In fact, the analytical solution shows that at the bottom discontinuity $x = 0$ three waves are present. First, a stationary shock shifting the bottom level $b_L = 1$ down to an intermediate bottom level $b_I = 0.5$ accompanied by a supercritical intermediate state. Then, a stationary hydraulic jump causes the supercritical intermediate state to become subcritical, which is then followed by another stationary shock that shifts the bottom level down to $b_R = 0$. The left rarefaction wave is not fully captured by both schemes, instead a wrong intermediate state emerges that connects the left state with the subcritical state at the right of the bottom jump. This is an artefact of the second-order reconstruction as the first-oder CN scheme is able to capture the critical state, see Figure 2.14. We remark that simply using the classical minmod-limiter, i. e. $\theta = 1$, is not enough.

In Riemann problem 6 (Figure 2.15), we again test a resonant regime over a downward bottom step, but this time with the right water level below the left bottom elevation. The emerging solution pattern is quite complex and similar to Riemann problem 3. Again, the first left wave is a rarefaction from the subcritical left state to a critical state, which then connects via two more shocks to the right subcritical state. Since at the bottom jump, the interface is partially wet, the adaptive reconstruction enables the BHNW scheme to capture the rarefaction wave at the left. To make this point clearer, we also compare the BHNW without adaptive reconstruction against the Audusse scheme with adaptive reconstruction in Figure 2.16. In fact, none of these two variants is able to capture the left rarefaction wave. This demonstrates the necessity for the adaptive second-order reconstruction. Moreover, the BHNW scheme provides a better estimate of the right state of the bottom discontinuity, when compared to the scheme of Audusse et al.

Riemann problem 7 (Figure 2.17) is a resonant regime over a large downward bottom step, that connects a subcritical left state with a supercritical right state.
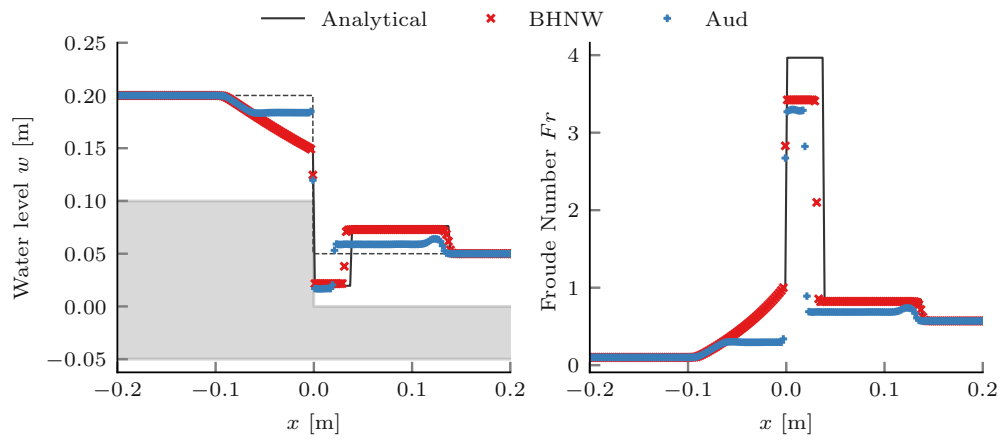
Fig. 2.15. Riemann problem 6. Partially-wet resonant regime over medium downward step connecting subcritical initial states. The BHNW scheme gets the full wave pattern right.
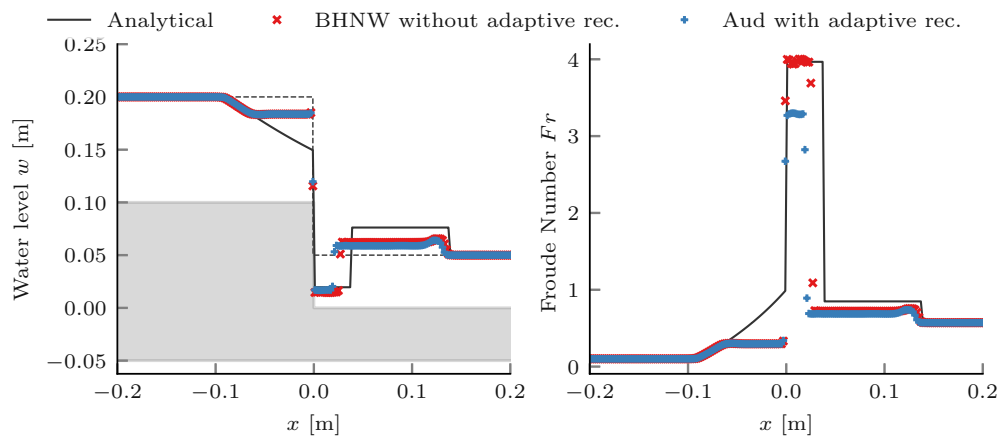

Fig. 2.16. Riemann problem 6. We compare two variants, the BHNW scheme without adaptive reconstruction and the Audusse scheme with adaptive reconstruction. Both fail to match the full wave pattern.
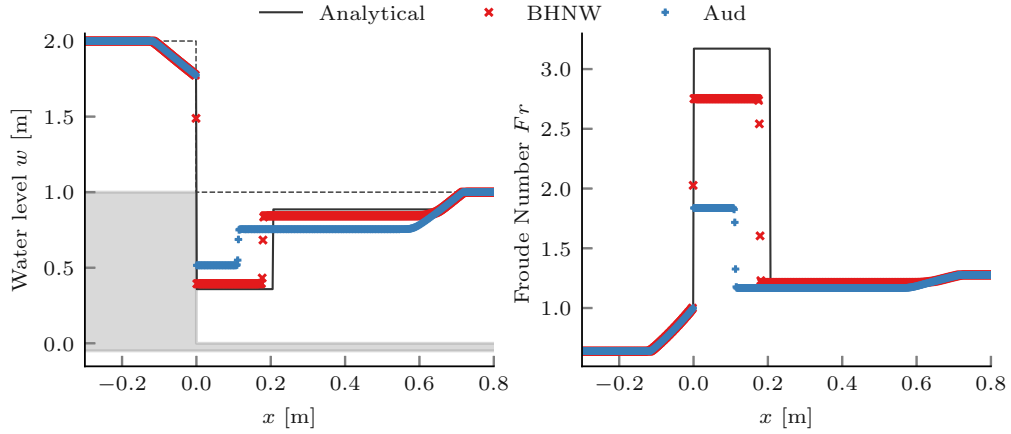
Fig. 2.17. Riemann problem 7. Partially-wet resonant regime over large downward step connecting a subcritical left state with a supercritical right state. The BHNW and Audusse's scheme capture the full wave pattern, however the BHNW provides better estimates of the right supercritical states.

The emerging solution pattern is similar to Riemann problem 6, except that the right-most wave is now a rarefaction wave. Here, also the scheme of Audusse et al. gets the left rarefaction right, however the BHNW achieves superior predictions of the right supercritical states.

Concluding this section of Riemann problems, we observe that the new BHNW scheme is able to outperform the scheme of Audusse et al. in the partially wet cases, while never performing worse than it.

2.3.4 Thacker's planar solution

Thacker's planar solution, sometimes also referenced as the parabolic basin, is a classical test case for validation. Thacker (1981) provides an analytical solution. It describes time-dependent oscillations of a planar water surface in a parabolic basin. It is widely used for comparing different numerical schemes (Asunción et al., 2013; Gallardo et al., 2007; Horváth et al., 2015; Liang and Marche, 2009; Sampson et al., 2006). Recently, Sampson et al. (2006) extended the solution of Thacker to support bed friction. However, their solution is limited to one dimension. In this two-dimensional case, we use the same setup as Holdahl et al. (1999), where the bathymetry is given by

$$b(x,y) = D_0 \left(\frac{x^2 + y^2}{L^2} - 1 \right), \tag{2.84}$$

where $L = 2500$ m, $D_0 = 1$ m.

First, we use a constant water level $w = 0$ m to show well-balancedness (Figure 2.18). We can see that the velocity errors are within the accuracy of single floating-point numbers, which we used in our implementation.
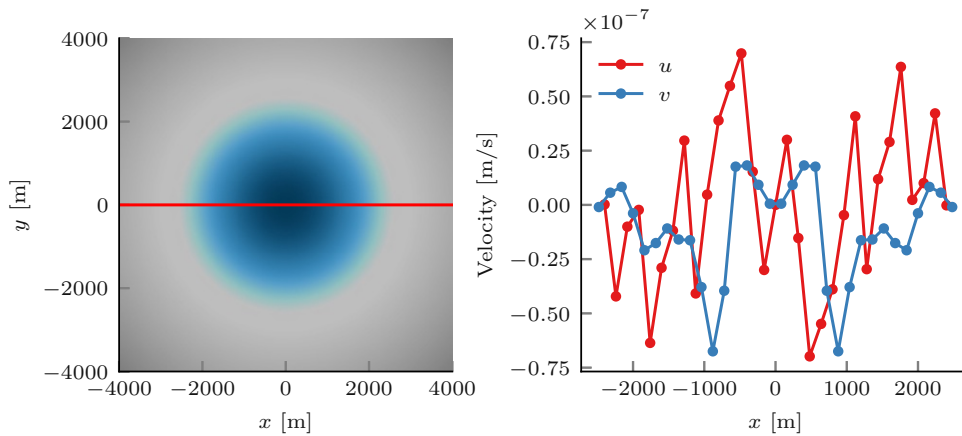
34

Fig. 2.18. Parabolic basin, well-balancedness. An initial lake at rest with constant water level $w = 0$ m for a parabolic basin is simulated for 1390 s on a grid with a cell size of 160 m. At the cross-section $y = 0$, which is marked with a red line, we extract the velocities of wet cells. The magnitude of the velocities is within single-precision floating-point accuracy for our proposed BHNW second-order scheme, thus it numerically preserves the lake at rest steady-state.
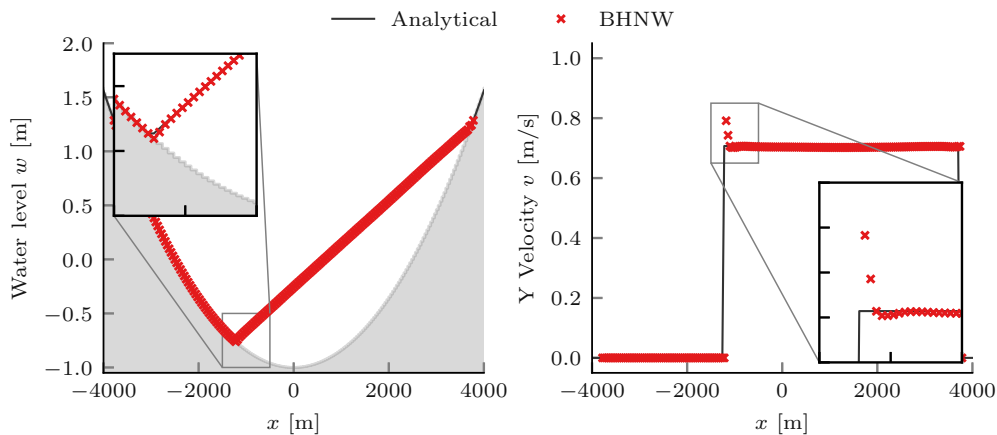

Fig. 2.19. Parabolic basin. Profiles along $y = 0$ of the water level and the velocity v in y-direction for the parabolic basin after one cycle at $T = 11120$ s. Approximations of the dry-wet boundary in the insets with a zoom factor of 3.0. The new second-order scheme (BHNW) approximates the analytical solution quite well on a grid with cell size $\Delta x = \Delta y = 80$ m.
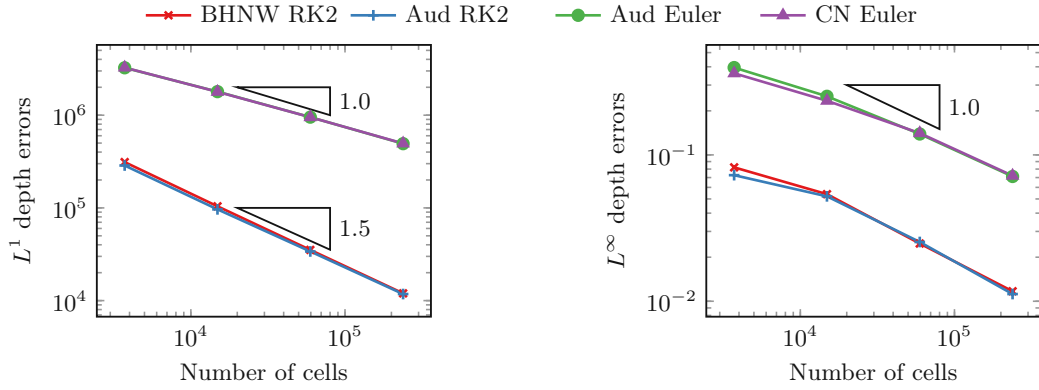
Fig. 2.20. Parabolic basin. Water depths error analysis after 11120 s for the and the second order schemes (BHNW RK2) and (Aud RK2) and the first-order schemes (CN Euler) and (Aud Euler)

Table 2.3. Parabolic basin. Water depths error analysis for the proposed second-order BHNW scheme and the second-order scheme of Audusse et al. (Aud RK2).

	BHNW RK2				Aud RK2		
Δx	L^1 Error	L^1 EOC	L^∞ Error	Δx	L^1 Error	L^1 EOC	L^∞ Error
160	311,910		0.0822	160	286,592		0.0727
80	104,038	1.60	0.0539	80	96,429	1.55	0.0521
40	35,221	1.56	0.0248	40	33,902	1.51	0.0254
20	11,976	1.57	0.0117	20	11,773	1.53	0.0112

Second, we test against analytically given time-dependent water surface elevation and velocities

$$w(x,y) = \frac{2AD_0}{L^2}\left(x\cos\Omega t + y\sin\Omega t + Lb\right),\tag{2.85}$$

$$u(x,y) = -A\Omega\sin\Omega t,\tag{2.86}$$

$$v(x,y) = A\Omega\cos\Omega t,\tag{2.87}$$

$$\Omega = \sqrt{\frac{2D_0}{L^2}},\tag{2.88}$$

where we choose $A = L/2, b_0 = -A/2L$, and the gravitational constant $g = 1 \text{ m}^2/\text{s}$ for our simulations. Then, the water level

$$w(x,y) = \frac{D_0}{L}\left(x\cos\Omega t + y\sin\Omega t + Lb\right),\tag{2.89}$$

is a plane rotating with an angular frequency of $\Omega \approx 5.66 \cdot 10^{-4}$.

We let our simulation run for one full period, and compare our results at $T = 11120$ s (Figure 2.19). A numerical error analysis shows that our scheme has second-order accuracy, see Figure 2.20 and Table 2.3. Reduced convergence due to the wet-dry boundary is also reported by others (Hou et al., 2013b; Delis et al., 2011).
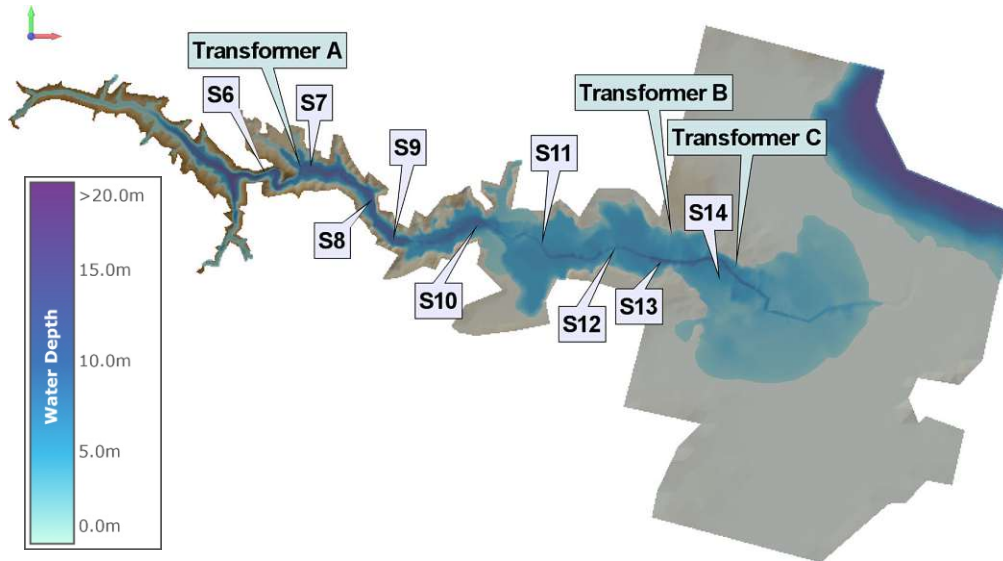
Fig. 2.21. Malpasset dam break, France. Water extent 2000 seconds after the dam break. Labels show the nine gauge locations (S6-S14) of the laboratory experiments and the three voltage transformers (A-C) in the real world.

2.3.5 Malpasset dam break

The Malpasset dam in southern France collapsed in 1959, resulting in a 40 m high water wave flooding the Reyran valley. The event was exhaustively studied in recent years (Brodtkorb et al., 2012; George, 2011; Hou et al., 2013b; Hou et al., 2013a; Singh et al., 2011; Valiani et al., 2002). We investigate the dam break on a structured grid with a cell size of 20 m. Friction is included with a uniform roughness coefficient of $n = 0.033$ m$^{1/3}$/s, corresponding to weedy, stony earth channels and floodplains with pasture and farmland. We compare simulation results with laboratory experiments of a 1:400 scaled model (Frazao et al., 1999; Hervouet and Petitjean, 1999). In this experiment, arrival times of the wave front (Frazao et al., 1999) and maximum water levels (Hervouet and Petitjean, 1999) were recorded at 14 gauge locations, labelled S1 to S14 in Figure 2.21. No data are available for the first 5 gauges, thus we use gauge locations S6 to S14 in our validation (Figure 2.22a, 2.22b). Additional data is also available for the shut-down time of voltage transformers of the historical event (Figure 2.22c). The locations of the gauges and transformers, as well as the inundated area after 2000 s is displayed in Figure 2.21. Small discrepancies between the scale model and the numerical results were also reported in other studies (Brodtkorb et al., 2012; George, 2011; Hou et al., 2014), and our results are consistent with these. When compared with the scheme of Audusse et al. (2004), minor differences only occur for gauges S8 to S10 for the water levels and for gauges S11 and S14 for the wave arrival times, with the new BHNW scheme obtaining comparable or slightly better results for most of the gauges except for the maximum water level at gauge S8. Regarding performance, our scheme is slightly
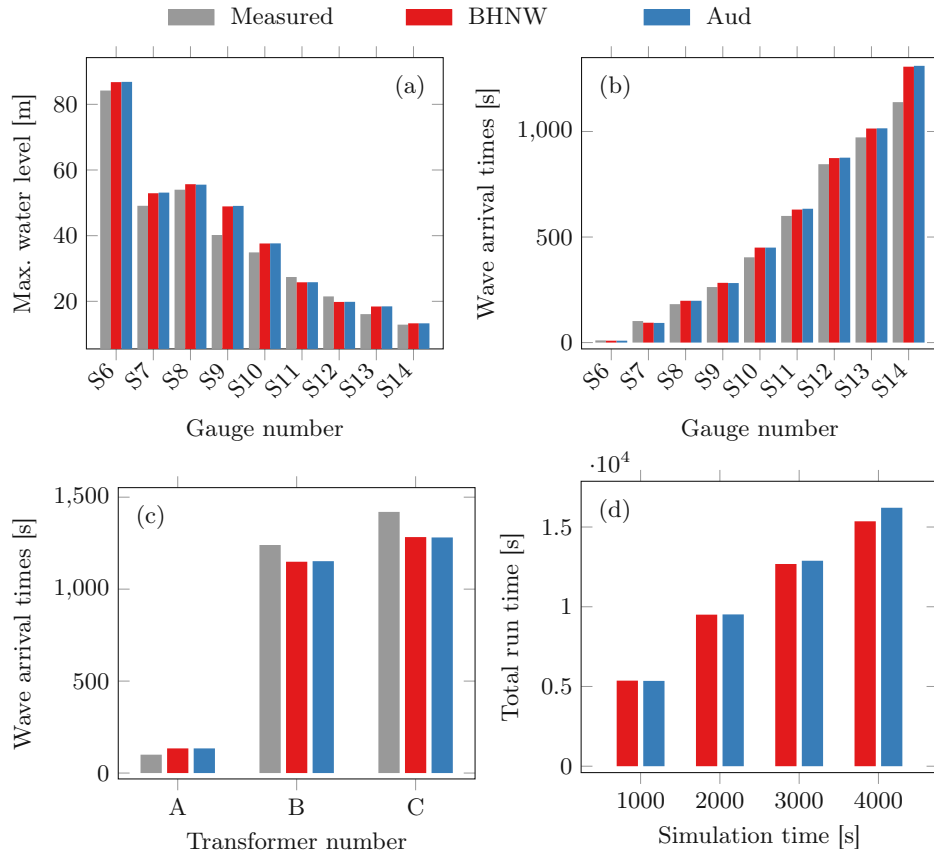
Fig. 2.22. Malpasset dam break, France. a) Maximum water elevations at the gauge locations (S6-S14). b) Wave arrival times at the gauge locations (S6-S14). c) Wave front arrival times at the three voltage transformers (1-3). d) CPU run times for different simulation times.

faster, 0.3 per cent run time reduction for the first 2000 simulated seconds, than the second-order scheme of Audusse et al. on a parallel implementation running on a machine with a 4-core Intel i5-4960K CPU at 3.5 GHz. Our proposed scheme performs better with increased simulation time because of the different reconstruction and source term treatment in regions with small water depths and complex terrain (Figure 2.22d).

2.3.6 Lobau

The Lobau is a floodplain east of Vienna, in Lower Austria, located at the left bank of the Danube. It consists mostly of floodplain forests and is regularly flooded. We simulate a flood that occured in January 2011 with a CUDA GPU implementation on a NVIDIA GeForce GTX 1070. The initial time is set to 13 January 2011, 1am, and the initial state comprises several still-water bodies and the Danube (Fig-
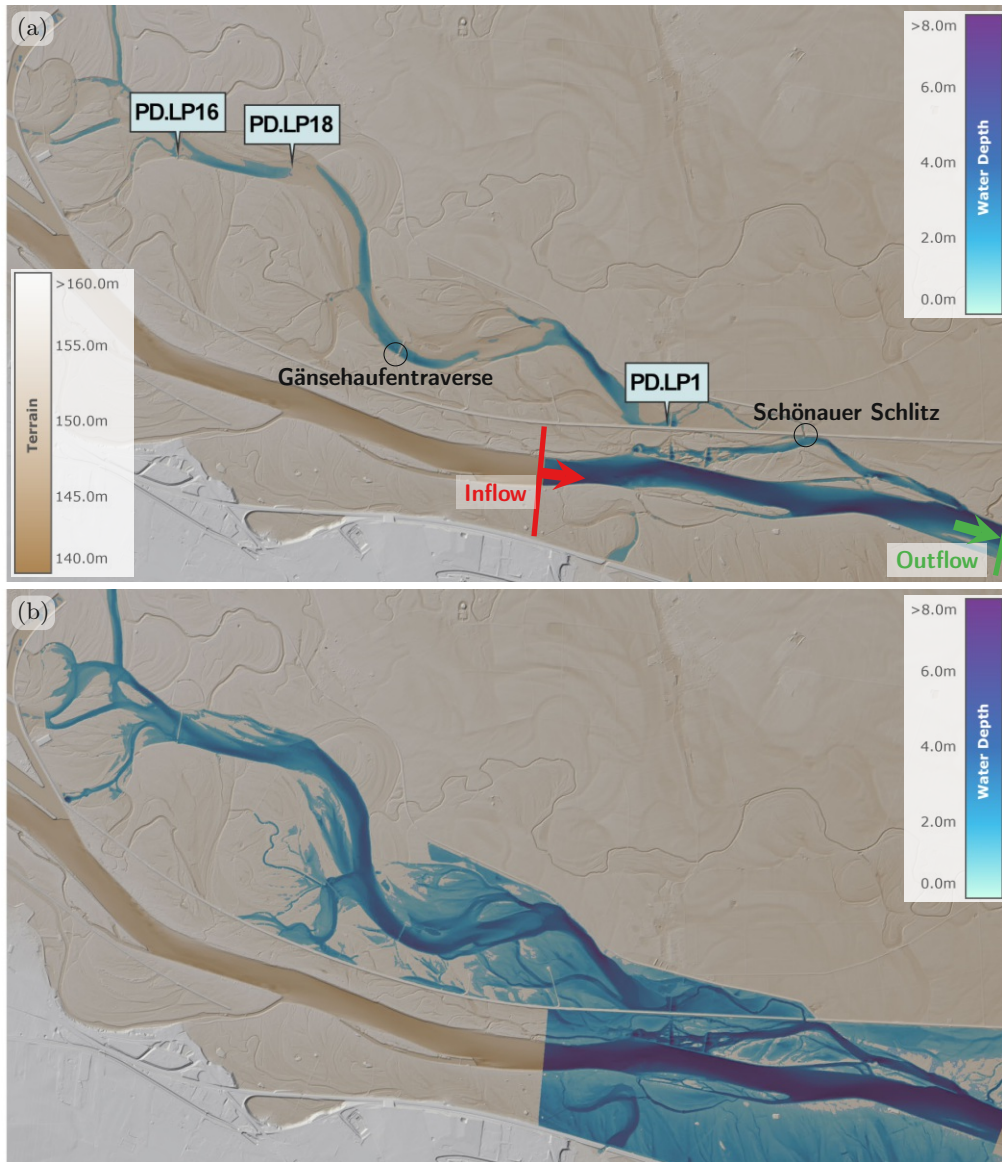
Fig. 2.23. Lobau historical flood, Austria. a) Bathymetry, initial water depths and location of the 3 gauges PD.LP1, PD.LP16 and PD.LP18 and the inflow and outlet hydrographs at the Danube. b) Flood extent and water depth after 2.5 days.

ure 2.23a). The water is flowing from the Danube into the Lobau only through a small slot, the "Schönauer Schlitz". The terrain is quite complex, featuring several small channels, which render simulations challenging.

We apply an inflow BC upstream of Fischamend and an outflow BC downstream of Fischamend (Figure 2.24a). The inflow BC is applied as a discharge BC (Pankratz et al., 2007), and the otuflow BC is implemented as a flux boundary condition based on water levels (Dutykh et al., 2011; Ghidaglia and Pascal, 2005). The simulation

39
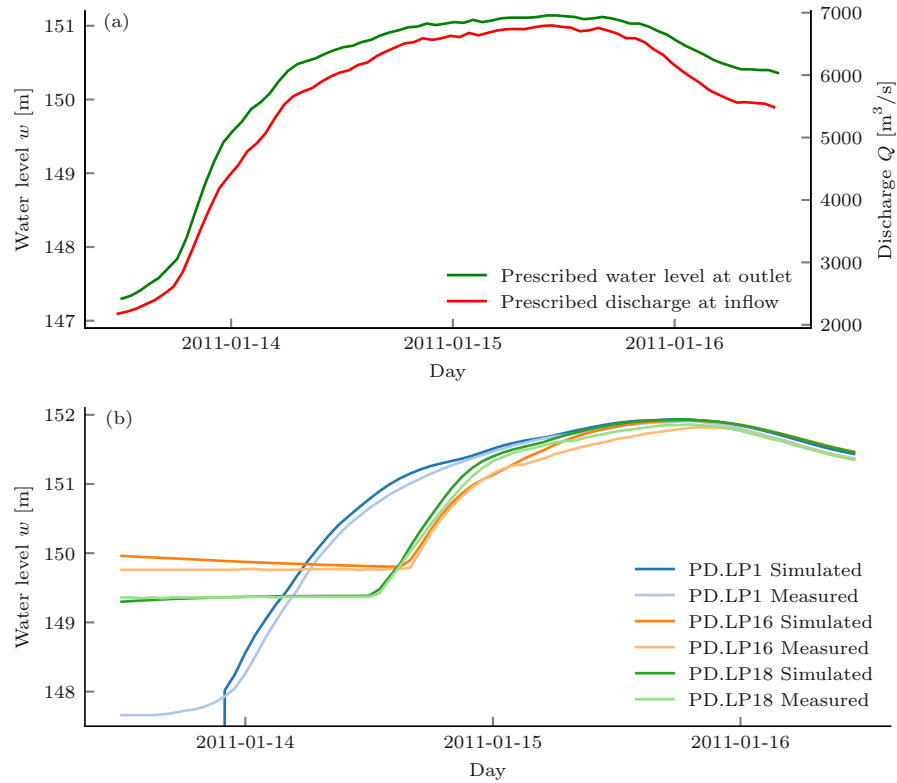
Fig. 2.24. Lobau historical flood, Austria. a) Discharge and water level time series used as boundary conditions at the Danube. b) Simulated and measured water levels at the gauges.

domain is roughly 10×7 km^2 large and the simulation cell size is set to 4 by 4 metres. The bathymetry is given on a raster with 2 m resolution. The Manning roughness coefficient n varies spatially between 0.03 and 0.13 m$^{1/3}$/s. It is estimated based on the land use. Hourly measured water levels are available at three locations, PD.LP1, PD.LP16 and PD.LP18. They are displayed alongside the simulated data in Figure 2.24b. The simulated water extent after 2.5 days is displayed in Figure 2.23b. The exact initial state is unknown and there is also an operated weir at the Gänse-haufentraverse, which might explain the small differences between the observed and the simulated flood waves at the gauge locations as it was modelled as a constant bathymetry modification. Taking into account those uncertainties, the measured water levels are predicted very well by the simulation.

2.4 Conclusion and future work

We derive and test a new formally second-order FVM scheme for the shallow water equations. The scheme is well-balanced, as it preserves both the still water and lake at rest steady states, and does not exhibit any oscillations. Instead of reconstructing

the discharge slopes, we reconstruct the velocity slopes to obtain robust choices of the wave speeds at wet-dry fronts, ensuring fast simulations. The scheme is particularly suited for implementations on GPUs, thus enabling faster than real-time simulations for large domains.

A numerical convergence analysis demonstrates that the scheme is second-order accurate. Validation against several benchmark tests, including multiple Riemann problems, reveals that the scheme converges against the reference solutions in most cases. Still, there are some scenarios where the solver does not produce satisfactory results. The scheme is able to reproduce real-world flood events such as the Malpasset dam break and a historical river flood in Austria. On test cases with shallow flow over abrupt topography, the new scheme achieves superior results than existing schemes. These improvements are due to an improved HR procedure and a novel adaptive second-order reconstruction strategy, which enables accurate resolution of shallow flow down a bottom step. Moreover, our proposed scheme only requires modification of a few lines of code when compared to the HR scheme of Audusse et al. To sum up, the scheme is able to capture complex flows over complex terrains accurately and efficiently as shown in the numerical test cases, all the more in the presence of thin water layers.

The scheme can be applied to unstructured grids, as the source terms are evaluated on a subcell basis, only the slope reconstruction needs to be revisited. In real world cases, the friction term plays an important role in predicting the correct evolution of the flood extent. We are planning to improve our scheme by balancing moving water in the presence of friction to gain better estimations of water levels and wave arrival times. Further work is directed to combine the scheme with an infiltration model for rainfall-runoff simulations.

3 Locally relevant high-resolution hydrodynamic modeling of river floods at the regional scale

The present chapter corresponds to the following scientific publication in its original form:

A. Buttinger-Kreuzhuber, J. Waser, D. Cornel, Z. Horváth, A. Konev, M. H. Wimmer, J. Komma, and G. Blöschl (2021). Locally Relevant High-Resolution Hydrodynamic Modeling of River Floods at the Regional Scale. Submitted to Water Resources Research.

Abstract

This paper deals with the simulation of inundated areas for a region of 84,000 km^2 from estimated flood discharges at a resolution of 2 m. We develop a modeling framework that enables efficient parallel processing of the project region by splitting it into simulation tiles. For each simulation tile the framework automatically calculates all input data and boundary conditions required for the hydraulic simulation on-the-fly. A novel method is proposed that ensures regionally consistent flood quantiles. Instead of simulating individual events, the framework simulates the flood quantiles by adjusting streamflow at river nodes. The model accounts for local effects from buildings, culverts, levees, and retention basins. The two-dimensional full shallow water equations are solved by a second-order accurate scheme for all river reaches in Austria with catchment sizes over 10 km^2, totalling to 33,380 km. Using graphics processing units (GPUs) a single NVIDIA Titan RTX simulates a period of 3 days for a tile with 50 million wet cells in less than 3 days. We find good agreement between simulated and measured stage–discharge relationships at gauges. The simulated flood hazard maps also compare well with local high-quality flood maps by achieving critical success index scores of 0.6 to 0.79.

3.1 Introduction

Climate change has modified river floods in Europe (Blöschl et al., 2019) and other parts of the world (Alfieri et al., 2017). In order to assist flood management agencies, regional planners, and insurance companies in adapting to the changing hazard, large-scale inundation maps associated with a given return period are needed. Recently, extensive research has been carried out on continental and global inundation mapping (Alfieri et al., 2014; Sampson et al., 2015; Dottori et al., 2016; Bates et

al., 2021), but bridging the gap between continental scale and local models is still challenging because of limitations regarding simulation accuracy and cost.

First, the accuracy of the hydraulic simulation is controlled, among other factors, by the numerical scheme and the resolution of the computational domain. Resolutions of a few meters are required to resolve terrain features such as levees and small channels. However, they require an efficient processing of a large amount of possibly heterogeneous data for large areas. Traditionally, two-dimensional (2D) hydrodynamic simulations were considered unviable for areas larger than 1000 km^2 and resolutions at the meter scale (Teng et al., 2017) due to the high computational costs, even though the value of a high resolution is clear (Ernst et al., 2010; Fewtrell et al., 2011; Shustikova et al., 2019; Xia et al., 2019; Horváth et al., 2020). Various approaches have therefore been proposed for speeding up simulations. One example are linked 1D/2D models (Morales-Hernández et al., 2013; Falter et al., 2016; Hoch et al., 2019; Rajib et al., 2020), but they have disadvantages related to complex data preprocessing, implementation of the linking model and the need for a case-by-case decision if the linked model is indeed significantly faster than a 2D model. Another possibility consists of simplifying the physical processes, e.g. neglecting advection or inertia terms (Neal et al., 2012). While in general this seems to be a computationally very efficient alternative, efficiencies may drop for urban regions (Costabile et al., 2020) and for receding flows including wet-dry boundaries (Cozzolino et al., 2019). Cozzolino et al. (2019) conclude that numerical issues in these problematic regions may originate from simplifying the shallow water equations (SWEs) while discretizations of the full SWEs are not subject to these limitations. For large-scale river flooding the usage of a second-order scheme instead of its first-order counterpart should be preferred as demonstrated in Horváth et al. (2020), even if the runtimes of the second-order scheme are higher. A more promising approach to reduce simulation runtimes is the parallelization of the code. In particular the use of graphics processing units (GPUs) may lead to a drastic reduction of runtimes (Brodtkorb et al., 2012; Horváth et al., 2016; Vacondio et al., 2016; Echeverribar et al., 2019) when compared to central processing units (CPUs). Simulations of flood events on GPUs may be faster than realtime for domains of hundreds of km^2 and resolutions of a few meters (Xia et al., 2019; Morales-Hernández et al., 2021).

Second, an efficient approach to simulate large regions with numerous streams is needed. Typically, a single processing unit in a computer cluster or a so-called computational node is not able to accommodate the entire domain. Thus the entire domain is split into subdomains with their sizes bound by the computational capability, e.g. memory, of the individual computational node. Common approaches involve a decomposition of the domain into individual river reaches allowing only small changes in flood discharges (Alfieri et al., 2014; Sampson et al., 2015; Bates et al., 2021). At the boundary of the subdomain, streamflow hydrographs are usually prescribed as inflow boundary conditions (BCs). The peaks of the streamflow hydrographs typically correspond to the flood quantiles of the return period of interest. For large simulation tiles, however, changes of the river flood quantiles along the stream network within the subdomain can no longer be ignored because of lateral

inflows including tributaries. Moreover, at confluences the downstream flood quantile is not simply the sum of the upstream quantiles as the upstream flood quantiles are typically not fully correlated in space.

Third, the accuracy of the inundated areas also depends on the accuracy of hydrologic and topographic input data, dense upstream streamflow boundary conditions (Rajib et al., 2020), and detailed models to capture local flow dynamics. Local relevance is thus not only achieved by high spatial resolution, but also by the inclusion of small-scale local features. For example, underpasses usually appear closed in digital terrain models (DTMs), but may actually be open during a flood event. The inclusion of levees and dams is required to ensure protected areas remain dry in the inundation model (Bates et al., 2021; Wing et al., 2017). Also the way buildings are treated has an effect on the small-scale dynamics of the water flow (Dottori et al., 2013). Culverts and power plants are often included in local models, but usually neglected in large-scale models. Inclusion of these detailed structures is needed for locally relevant, regional flood simulation, especially in densely inhabited areas. The accuracy of the models can be assessed by comparing the flood areas with carefully designed local models (Wing et al., 2017), with remotely observed flood inundation extents (Rajib et al., 2020), with observed high water marks (Wing et al., 2021), and with insurance claims (Zischg et al., 2018).

Fourth, multiple steps are required for setting up the input data and the BCs for hydraulic simulations. In a traditional modeling setup these steps are usually carried out manually to allow for the handling of special cases which almost always occur in real world applications. An automatic execution of the workflow requires a consistent approach to process the steps, e.g. a dataflow consisting of linked submodels that share data via input and output connections. Ideally, the whole modular dataflow is controlled by one interactive automation framework (Sampson et al., 2015) that allows for localized data corrections and automatically triggers only local resimulations.

In this paper, we present a framework for simulating river floods with a resolution of 2 m for all of Austria (84,000 km^2) as illustrated in Figure 3.1. This paper goes beyond the existing literature by simulating a river network of 33,880 km with a second-order scheme that discretizes the full SWEs. We demonstrate the effectiveness of accelerated computational models to enhance the accuracy and local relevance of the simulations. We propose a novel method to ensure consistent flood quantiles across the entire river network of large simulation domains. Starting from raw input data for an entire country, we describe an automated simulation setup that derives BCs on-the-fly for the derivation of inundated areas. The proposed model introduces streamflow hydrographs for all catchments greater than 10 km^2 and accounts for levees, buildings, and culverts to provide locally relevant inundation maps. We also perform a combined validation against rating curves of stream gauges and against detailed local flood maps.
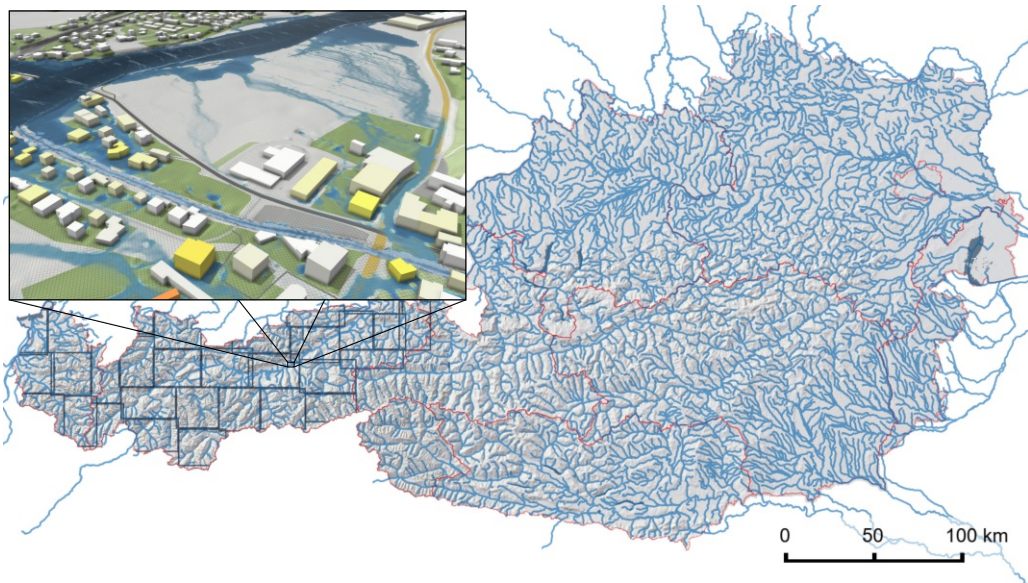
Fig. 3.1. Simulated rivers in Austria with decomposed simulation domains shown in the west. The inset image shows the simulated maximum water depths on the 2 m grid. The high resolution together with regionally consistent flood quantiles result in detailed, locally relevant inundation maps.

3.2 Methods

3.2.1 Integrated setup as a Visdom dataflow

In order to obtain inundation maps from raw input data, a cascade of submodels needs to be executed. A simplified version of the cascade of submodels, the so-called modular dataflow, used in our approach is shown in Fig. 3.2. The raw input data comprise land use, stream gauge records, the river network, river thalweg and river bank lines, the DTM, and measured river bed profiles, as shown at the top of Fig. 3.2.

For a given simulation domain, the dataflow then assembles all the necessary data for the hydraulic simulation including the roughness, the boundary conditions (BCs), the hydrologically enforced digital terrain model (DTM-H), and an initial state of water levels. The roughness is estimated from land use in the floodplains and from calibrated roughness at stream gauges. The BCs account for buildings and hydraulic structures, such as culverts and power plants. Moreover, at the boundary of the simulation domain and at river origins, the BCs prescribe flood hydrographs statistically estimated based on discharge measurements, the river network topology, and other information. This sub-dataflow is visualized on the left of Fig. 3.2.

The DTM-H represents a DTM that has been prepared for hydraulic modeling, e. g. bridges have been cut-out and river beds have been burned in to allow free flow. For most of the larger rivers in Austria bed measurements exist. Thus, we choose
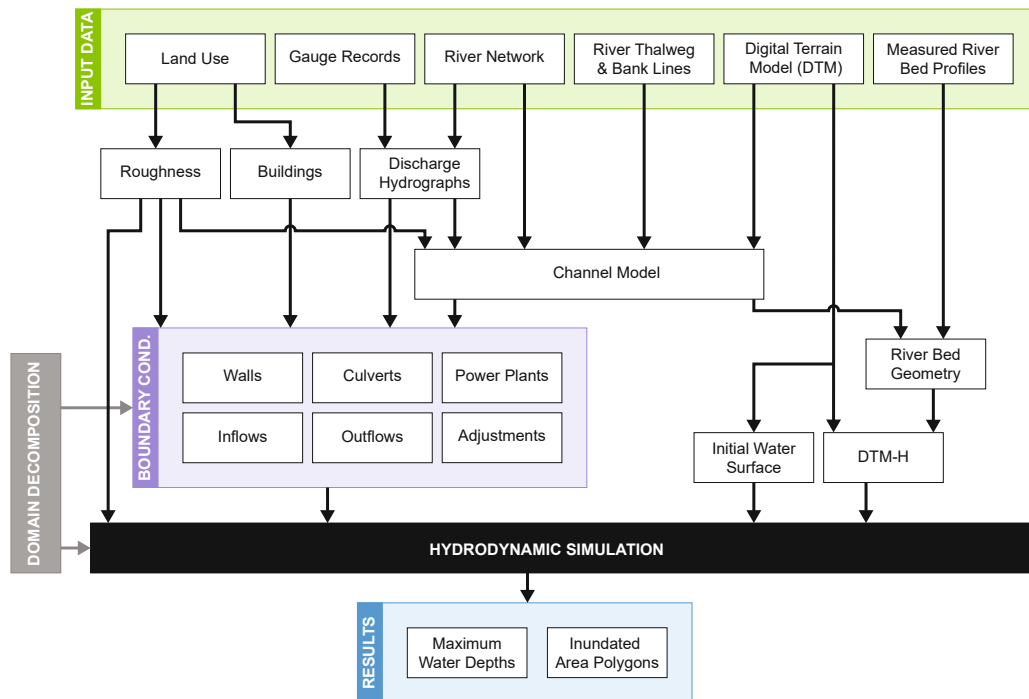
46

Fig. 3.2. Simplified dataflow of the flood inundation model in the proposed automation framework.

a dual approach. Where measurements exist, the river bathymetries are used to modify the DTM. Where no measurements exist, we estimate a trapezoidal profile based on discharge, the river network topology, the river thalweg and the river bank lines, and the DTM. This sub-dataflow is visualized on the right of Fig. 3.2.

The entire study region is split manually into rectangular tiles. There are no restrictions on the domain decomposition from the input data. Given any domain, instationary BCs are specified automatically. The only step involving manual manipulations are corrections of data errors, e. g. of river bed measurements or the coordinates of river thalweg and bank lines. The manual corrections and the domain decomposition are stored as "actions" in separate layers which are later applied automatically to the relevant data. For each of the tiles, BCs are automatically generated and the computation of the required input data for the hydrodynamic simulation is triggered. Initial water depths for the hydraulic simulation are obtained by subtracting the DTM-H from the original DTM. The simulation then computes water depth fields and velocity vector fields. Finally, at the bottom of the cascade, the flood hazard maps are identified from the simulated maximum water depths.

Ideally, the execution of the dataflow should not involve any manual intervention. Here we use the interactive automation framework Visdom (Waser et al., 2011; Schindler et al., 2013), which determines the execution order by itself and executes the cascade of submodels in a fully automated way. Moreover, Visdom features
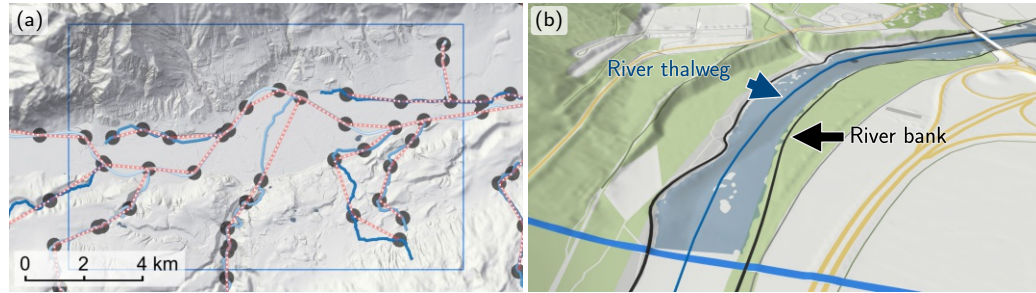
Fig. 3.3. (a) River network around Innsbruck, Austria. The network consists of nodes (gray circles) linked by the river. The nodes hold the hydrologic data, such as flood discharges. (b) Detail of river thalweg lines and river bank lines.

an interactive visual representation of the dataflow consisting of several dozens of modular units and hundreds of connections. In reality the dataflow is more complex than the illustrative dataflow shown in Fig. 3.2. Visdom allows interactive changes to the dataflow in an accessible graphical user interface throughout the entire project period. Moreover, the graphical representation greatly facilitates the comprehension of the dependencies between submodels.

3.2.2 Input data and pre-processing

Terrain model

The digital terrain model (DTM) covers all of Austria with a spatial resolution of 1 m and is based on light detection and ranging (LIDAR) data. The vertical precision of airborne laser scanning is at the order of a few centimeters (Pfeifer and Briese, 2007; Kraus, 2011). However, the accuracy of the DTM, which is interpolated from the DTM, also depends on other factors not fully represented by ALS data, e. g. water bodies and vegetated river banks. The acquired point clouds completely lack information about submerged topography, such as river beds, which has to be added. Bridges and non-monotonic terrain levels along rivers are eliminated from the DTM and the gaps are filled by adaptive river course interpolation between the unobstructed parts to obtain the DTM-H (Wimmer et al., 2021).

River network

The digital river network consists of nodes and their directed connections. Each node is allowed to only have one downstream node. Nodes are placed at conflu-ences (Fig. 3.3a) and where stream discharges change significantly, for example downstream of power plants. The nodes hold the hydrologic data, such as flood discharges. In total, the river network consists of 19,479 nodes. The river thalweg lines are automatically realigned with thalweg lines derived from the DTM. In cases of doubt, manual checks and revisions are performed (Wimmer et al., 2021). Ad-ditionally, a left and a right river bank line representing the extent of the water
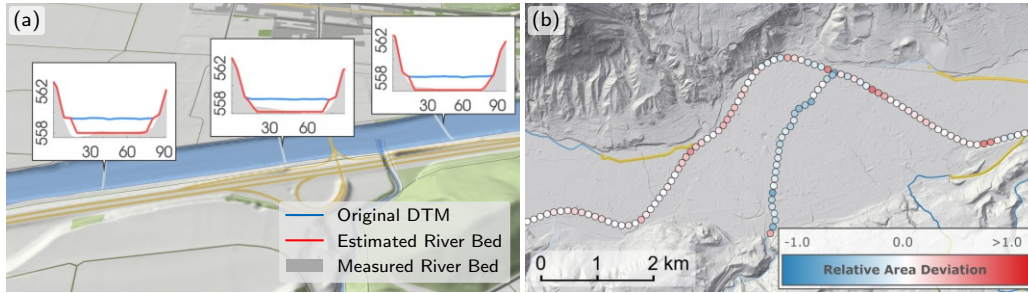
Fig. 3.4. (a) Example validation of the estimated trapezoids (red) burned into the original DTM (blue) against the measured bottom topography (grey) at the Inn river. Numbers are length across the river (m) and level (m). (b) Comparison of the burn-in approach against measured cross-sectional data along the Inn river and a tributary in terms of their relative wet area deviation. Red indicates an overestimation of the computed wet areas, blue an underestimation. The yellow lines indicate culverts, where the river bed was not burned in.

body in case of bank-full flow are generated (Fig. 3.3b). In total, 33,880 river km are delineated representing all Austrian streams with a catchment size greater than 10 km^2.

Streamflow boundary conditions

Streamflow boundary conditions are given by synthetic flood discharge hydrographs of the form

$$Q(t) = Q_B + (Q_T - Q_B) \left(\frac{t}{t_P} \exp \left(1 - \frac{t}{t_P} \right) \right)^{\gamma}, \tag{3.1}$$

where Q_B is the mean annual discharge, Q_T is the peak discharge of the flood peak for the associated return period, e.g. $T = 100$ years, and γ is set to 3 based on hydrograph analyses in the study area. The time to peak parameter t_P, Q_B and Q_T are estimated by a statistical regionalization method based on Top-Kriging (Skøien et al., 2006) following Merz et al. (2008).

River bed geometry

In Austria, 18.6% of all river km are covered by measured profile data, mostly at the larger rivers. Following Bures et al. (2019) and Fleischmann et al. (2019), we adopt a combined approach and construct the river bed from measured river bed profiles and estimated trapezoidal cross-sections. The cross-sectional river width is based on the distance between the left and right river bank lines. The depth is determined by Manning's equation under the assumption of a trapezoidal cross-section with a bank slope of 60°. The Manning's roughness value is set to the same value as used in the SWEs (see Section 3.2.2). The slope of the energy grade line is determined by sampling the original DTM including water bodies along the river thalweg line. The discharge consistent with the time of the DTM survey is assumed to be proportional

to the mean annual discharge. A proportionality factor of 0.7 was backcalculated from measured profile data. A factor smaller than 1 is in line with the practice of conducting DTM surveys in autumn when stream flow is low in Austria (Merz et al., 1999). Fig. 3.4a shows a comparison of estimated trapezoidal cross-sections and measured river bed geometries for a reach of the Inn river and Fig. 3.4b shows the associated relative wet area deviations defined as the ratios of estimated wet areas over measured wet areas. For the major river flowing from west to east (the Inn river) the bed is approximated very well. For the southern tributary the estimated cross-section is slightly too deep.

Roughness

The spatially distributed roughness coefficient is compiled from different sources. In the floodplains, a mapping from land use type to Manning roughness coefficients is adopted from (Chow, 1959). Inside the river channel, we calibrate the roughness with water level and discharge data from 420 stream gauges. A calibration with the full 2D high-resolution model throughout Austria's gauges requires an excessive computational effort, so we choose to calibrate the roughness at each gauge individually with Manning's equation, in a similar way as in the derivation of the trapezoidal cross-sections. The estimated roughness values are interpolated on the river nodes with Top-Kriging. To reduce the influence of only locally valid high roughness coefficients at some gauges, we average the estimated roughness values with a default roughness value of 0.03 $s/m^{1/3}$. The resulting Manning roughness coefficients along all rivers are displayed in Fig. 3.5a. For a number of reaches (3350 river km), roughness coefficients are available from detailed local analyses carried out in previous local studies. In these regions, they are averaged with the roughness coefficients based on land use and the ones interpolated from the stream gauges. A detail of the final spatially distributed roughness field is shown in Fig. 3.5b.

3.2.3 Automatic boundary conditions

Tiling

The flood modeling region of Austria is split into 182 rectangular simulation tiles on the basis of the following criteria: The tiles are specified in such a way that power plants are far enough away from an inflow, so that backwater effects are fully captured. Cities and large confluences are sought to be in the middle of a tile to avoid boundary effects. The tiles are required to overlap with each other to capture all flooded areas originating from levee overtoppings several kilometres up- or downstream in the case of large rivers. The entirety of all 182 simulation tiles covers the complete Austrian terrority.

To balance these goals, the tiles are adjusted manually. The tile size is limited by the available memory on the GPU to a total number of around 150 million wet cells. Thus, given a resolution of 2 m, we limit the tiles to an area of 1000 km^2, assuming a maximum of 60 % wet cells. In contrast to tightly coupled distributed
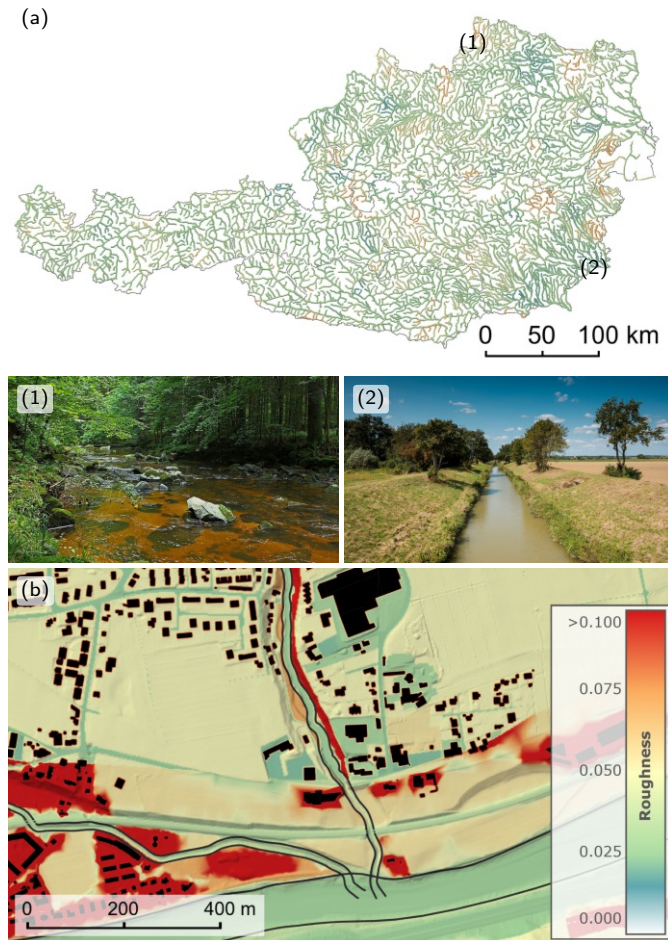
Fig. 3.5. (a) Roughness coefficients in the river channel interpolated from coefficients calibrated at the stream gauges to the river network with Top-Kriging. The photos give an impression of the river characteristics of locations with (1) a high roughness of around 0.06 s/m$^{1/3}$ for a natural stream in rocky hills and (2) a relatively low roughness of 0.02 s/m$^{1/3}$ for a regulated stream in the lowlands. (b) The spatially distributed roughness coefficients in the floodplains are based on land use. The roughness legend is valid for both (a) and (b). Image Copyright: (1) https://commons.wikimedia.org/wiki/File: Die_Lainsitz_im_Gabrielental_bei_Weitra_01_NDM_GD-103.jpg, CC BY-SA 3.0 AT. (2) Hydro Burgenland, Heiligenbrunn / Strem. Permission granted.
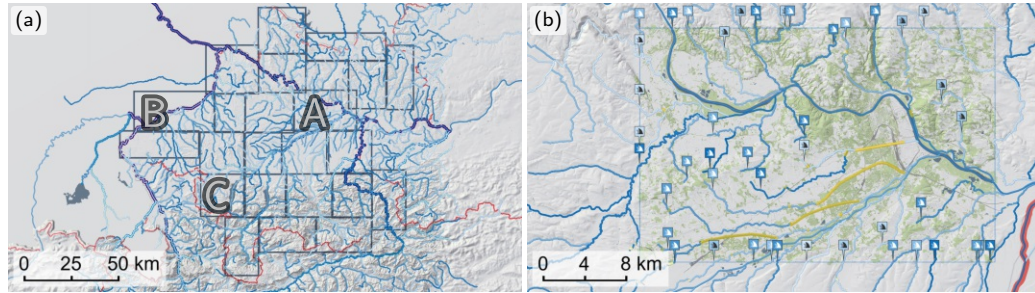
Fig. 3.6. (a) Domain decomposition of Upper Austria into 24 tiles which are simulated in parallel. The size of a tile is limited by the memory of a single GPU. The tiles labelled A, B, C show slow simulation performance (Fig. 3.11). (b) Close-up of tile A with all BCs. Inflows and outflows are displayed as wave icons. Culverts are indicated as dark yellow lines.

simulations, where state variables of the simulation tiles are shared at each time step, here, the tiles are simulated completely independent of each other enabling fast parallel processing. In a post-processing step, the simulated inundated areas of each tile are then aggregated as specified in the last paragraph of Section 3.2.4, resulting in a flood hazard map covering all of Austria. A detail of the tiling for a subregion (Upper Austria) is shown in Fig. 3.6 along with the locations of the automatically derived boundary conditions, including inflows and outflows shown as wave icons.

Automatic inflows

Whenever a river enters a simulation tile or starts inside a simulation tile, upstream BCs are derived (Fig. 3.7a). The flood hydrograph at the inflow positions is calculated by Eq. (3.1) from interpolated hydrologic parameters (Fig. 3.7b). In order to account for the travel times of the flood waves, the hydrographs are shifted in time by a recursive algorithm (Section 3.2.3). The inflow geometry is identified by constructing a cross-sectional line normal to the river line and intersecting it with the river bank lines. This line is extended by a fixed factor on both sides and based on trial and error a factor of two was chosen (Fig. 3.7c). At the rasterized cell interfaces of the extended cross-sectional line, we prescribe a fraction of the discharge given by the hydrograph. The fraction at each interface is assumed to be proportional to the water depth ensuring a natural distribution of the discharge, as only neighboring wet cells receive a water influx.

Adjustments for consistent quantiles

We propose a new method that allows maintaining the same return period of flood peaks for the entire stream network. Traditionally, flood simulations are performed for scenarios representing individual events in a mass-conserving way. In contrast, in this study we perform simulations where the return period of the peak flows are
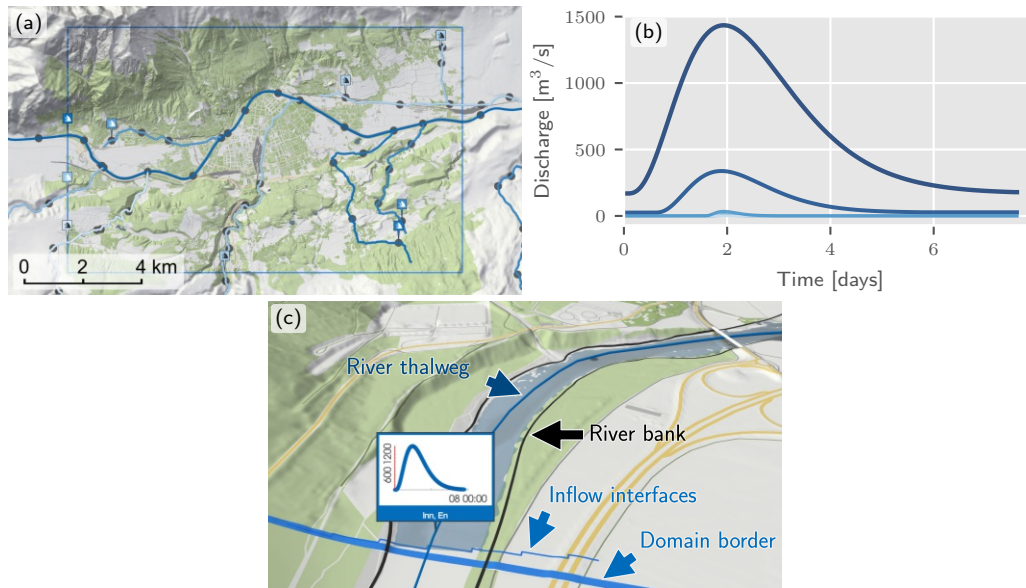
Fig. 3.7. Automatically derived inflows for an arbitrarily chosen domain. (a) Inflows are placed at the start of rivers and when streams enter the domain. (b) At each of the nine inflows shown in (a), a flood hydrograph is calculated from the interpolated hydrologic parameters of the upstream node. (c) At an inflow, the discharge is then distributed on the rasterized inflow interfaces of the cross-sectional line normal to the river thalweg.

maintained across the entire stream network. In order to achieve this, water needs to be added or removed in a precisely specified way. Small tributaries, which are not explicitly resolved in the river network, contribute to an increase in flood discharges along a river. In such a case, water is added along the river to ensure return periods are maintained.

More importantly, confluences are considered in a similar fashion. Such a situation is illustrated in Fig. 3.8a for the Inn–Sill confluence. In Fig. 3.8b the corresponding hydrographs of the tributary before the confluence, as well as the hydrographs of the main river before and after the confluences are plotted. The sum of the tributaries peak discharge and the peak discharge of the main river upstream of the confluence is generally greater than the peak discharge downstream of the confluence. This is because of the probability of a joint occurence of floods at both streams is usually significantly smaller than 1 (Bender et al., 2016; Guse et al., 2020). For a confluence node, the adjustment is given by the difference between the sum of the upstream hydrographs and the downstream hydrograph associated with that node. The resulting difference hydrograph at the confluence is negative around the peak time (Fig. 3.8b). Therefore, at a confluence typically water needs to be removed from the hydraulic simulation to ensure the same return period. This adjustment is performed at rasterized adjustment polygons related to the river geometry (indicated in green in Fig. 3.8a). In these cells, a specific source term is introduced in the SWEs, which applies the adjustment to the wet cells in the polygon.
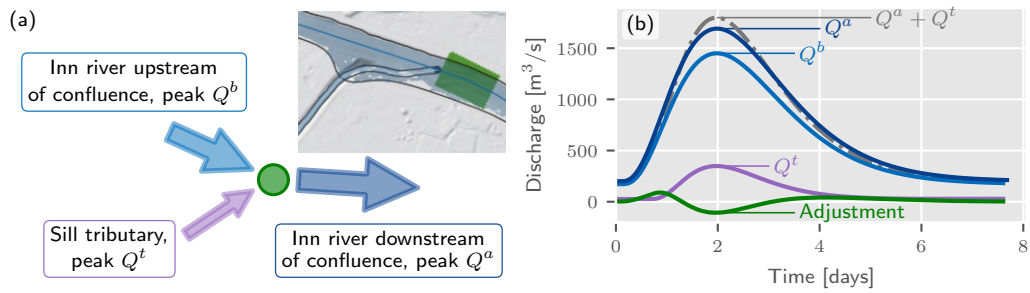
Fig. 3.8. Hydrographs at the Inn–Sill confluence for a 100-year flood. (a) A schematic illustration of the confluence with an inset image of the real-world situation. (b) The hydrographs at the confluence with the hydrograph of the tributary shown in violet. The adjustment is made at specific cells (indicated in green in (a)) via a source term.

Temporal relationship between streamflow hydrographs

At each node, a hydrograph is specified by the statistical regionalisation described in Section 3.2.2. For aligning the hydrographs in time in a consistent way, we adopt the following procedure.

First, we need to approximate the wave travel time in the two-dimensional hydraulic simulation of a flood hydrograph from a river network node to its downstream neighbor. We estimate the travel time with a uniform wave approximation and the velocity obtained from Manning's law using the median water depth, the average roughness and slope along the reach as well as the river width, assuming the wave celerity is not vastly different from the flow velocity.

Second, as far as the timing is concerned, we assume that flood waves at confluences peak simultaneously. This assumption ensures that the differences in the discharge time series are smaller in magnitude than for non-synchronous flood peaks, which improves numerical stability. We illustrate the effects of these two assumptions in Fig. 3.9a and b, respectively, on a small domain shown in Fig. 3.9c.

Third, if a simulation tile is divisible into multiple smaller independent river networks, the peak time at the outflows is set to occur at the same time. This rule increases simulation performance as it ensures fast simulations until the common flood peak, as the simulation is faster before the flood peak than after the flood peak due to the comparably smaller percentage of wet areas.

Based on the above assumptions, a recursive algorithm determines all the time shifts needed for the adjustment and inflow hydrographs. The required simulation time of a tile is controlled by the node with the maximum hydrograph duration. The hydrograph duration is determined by the time to peak parameter and the travel time needed for the wave at that node to leave the domain. The required simulation durations range from 1.7 days in steep terrain to 31 days in tiles with lakes and large rivers.
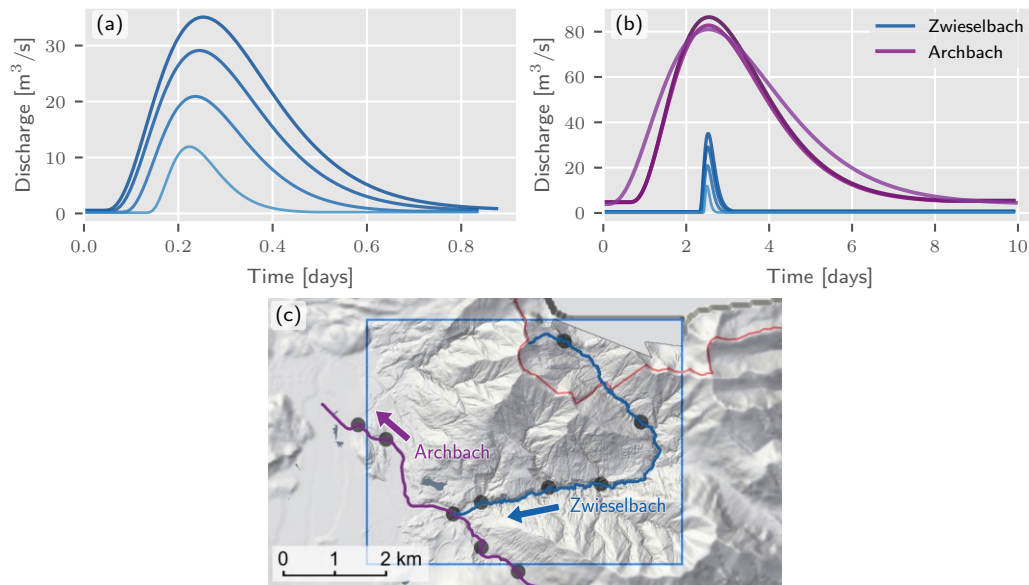
Fig. 3.9. (a) Streamflow hydrographs at the river network nodes of a single river reach, the Zwieselbach in Tyrol. The peaks are slightly shifted by time lags computed from an uniform wave approximation. (b) Streamflow hydrographs at the nodes of the main river, the Archbach, and a tributary, the Zwieselbach. At the confluence the peaks are exactly aligned. The river with the shorter hydrograph duration, in this case the Zwieselbach, is shifted towards the river with the longer hydrograph duration. (c) Associated nodes and domain.
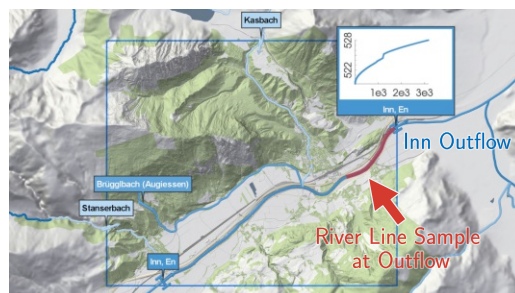
Fig. 3.10. Outflow rating curve automatically derived from the water level slope along the river thalweg line, the roughness along the river and along the outflow cross section. Simulated outflow discharges are mapped to a water level at every time step.

Rating curve outflows

Whenever a river leaves a tile, outflow BCs are automatically derived. The geometric setup is similar to the inflows, however we extend the cross-sectional line only by 20% at each side in contrast to the 100% for inflows. We specify an absorbing BC at the domain boundary allowing water to freely leave the domain. Thus, if water bypasses the specified outflow interfaces, it can leave the domain at the boundary. To

ensure numerical stability, we prescribe a dynamic water level BC at the outflows. Specifically, we employ a rating curve to dynamically map the currently simulated discharge that leaves the domain through this outflow BC to the corresponding water level (Fig. 3.10). Assuming uniform flow, we use Manning's equation to derive the rating curve. We emphasize that here dynamic means that the water level time series is not a priori set from recorded gauge data (Horváth et al., 2020), but computed at every time step via the rating curve. This dynamic outflow condition ensures a correct specification of the water level accounting for changes of the flood wave inside the simulation domain, such as peak discharge reduction due to dike overtoppings or floodplain spills, and avoids a possibly incorrect propagation of a priori converted peak water levels at the downstream boundaries into the simulation domain.

Buildings, culverts and power plants

Given the resolution of 2 m, all buildings in the domain are rasterized as wall cells where no water can enter. In urban regions, culverts and sewers may affect the inundation area. While the representation of urban sewer systems is beyond the scope of this paper, we do use a simple culvert model supporting culverts without bifurcations that are fed by streams and aligned with river thalweg lines. The cross-sectional geometry is automatically derived from the river thalweg and river bank lines at the culvert ends. The discharge is computed taking into account the pressure heads and the cross-sectional geometry at the in- and outlet. In total, there are 1475 culverts.

Additionally, run-of-river and high-head power plants are considered. For large rivers, the weirs of run-of-river power plants that are opened during floods are represented in the DTM-H. The retention effects of high-head power plants are simulated by specifying water level-discharge relationships of the outlets. Downstream of the reservoirs, hydrographs are set as upstream BCs analogously to the inflows in Section 3.2.3.

3.2.4 Hydrodynamic simulation

The hydrodynamic simulation engine solves the full two-dimensional shallow water equations (SWEs)

$$\partial_t \mathbf{U} + \partial_x \mathbf{F}\left(\mathbf{U}\right) + \partial_y \mathbf{G}\left(\mathbf{U}\right) = \mathbf{S}_b\left(\mathbf{U}, b\right) + \mathbf{S}_f\left(\mathbf{U}\right) + \mathbf{S}_c, \tag{3.2}$$

where $\mathbf{U} = \left[h, hu, hv\right]^T$ is the vector of conserved variables and $\mathbf{F}$ and $\mathbf{G}$ are the flux functions

$$\mathbf{F} = \begin{bmatrix} hu \\ hu^2 + \frac{1}{2}gh^2 \\ huv \end{bmatrix}, \quad \mathbf{G} = \begin{bmatrix} hv \\ huv \\ hv^2 + \frac{1}{2}gh^2 \end{bmatrix}. \tag{3.3}$$

The bed slope term $\mathbf{S}_b$ models the fluid's acceleration due to gravitational forces,

$$\mathbf{S}_b = \begin{bmatrix} 0 \\ -gh\partial_x b \\ -gh\partial_y b \end{bmatrix}. \tag{3.4}$$

Flow resistance is modeled by the friction term $\mathbf{S}_f$,

$$\mathbf{S}_f = \begin{bmatrix} 0 \\ -gn^2 h^{-1/3} u\sqrt{u^2+v^2} \\ -gn^2 h^{-1/3} v\sqrt{u^2+v^2} \end{bmatrix}. \tag{3.5}$$

In these definitions, h represents the water height, hu is the discharge along the x-axis, hv is the discharge along the y-axis representing the conserved variables. Furthermore, u and v are the average flow velocities in x and y-direction respectively, g is the gravitational constant, and b is the bathymetry (assumed to be time-independent), and n is the Manning roughness coefficient. The source and sink term $\mathbf{S}_c$ is only active in adjustment cells with prescribed positive or negative discharges (Section 3.2.3).

For the spatial discretization of the SWEs, the finite volume method (FVM) is used on a uniform Cartesian grid of 2 m. We employ a second-order accurate scheme (Buttinger-Kreuzhuber et al., 2019). The bed source term is discretized to preserve still-water steady states, i.e. the scheme is well-balanced. The scheme properly handles flow states across bed discontinuities and achieves second-order accuracy in space through a minmod limiter. The minmod-parameter is set to one, in order to ensure robust and fast simulations (Horváth et al., 2020). At wet-dry boundaries only the velocities are set to zero below a cut-off water depth threshold, set to 0.0001 m, thus ensuring mass conservation up to floating-point precision. The friction source term $\mathbf{S}_f$ is evaluated in a semi-implicit manner by splitting it into a coefficient-wise product of an implicitly evaluated state and an explicitly evaluated friction term (Brodtkorb et al., 2012). For the second-order time integration we use Heun's method (Buttinger-Kreuzhuber et al., 2019).

The FVM enables straightforward parallelization on regular grids. The scheme is implemented on GPUs for substantially faster runtimes relative to CPUs. A simulation tile is split into thousands of blocks consisting of 14 by 14 cells. When a block is dry and not at risk of flooding, it is excluded from the hydraulic simulation. Therefore, only wet blocks have an impact on the simulation runtime. The implementation is heavily optimized and relies on Kepler shuffles for fast processing of the numerical stencil (Horváth et al., 2016). Well-constructed datastructures consisting of mostly single-precision floats guarantee that the GPU achieves maximum performance. We use 10 NVIDIA Titan RTX GPUs in parallel, each equipped with 24 GB of video memory. For the second-order accurate scheme, each GPU is able to process a maximum of approximately 150 million wet cells. The exact number depends on the distribution of the wet cells, input data size of the BCs and other minor factors.

Table 3.1. Wet areas, average model runtimes, and average simulated time by Austria's regions for a 100-year flood. For each region, the model runtimes are given in the average values per km² of simulated wet area (per 250,000 wet cells).

Region	Sim. Wet Area [km²]	Runtime [hours/km²]	Simulated Time [days]
Carinthia	372.1	2.40	7.80
Lower Austria	1463.7	1.80	7.24
Salzburg	209.4	1.92	5.93
Styria	636.9	1.28	4.71
Tyrol and Vorarlberg	307.5	1.79	4.44
Upper Austria	541.9	2.51	9.87
Austria	3531.5	1.88	6.54

The tiles specified in Section 3.2.3 are processed in parallel and independent of each other. Each GPU processes one tile and does not need to exchange data with another simulation. For a cluster of 10 GPUs, 10 tiles are processed in parallel. Whenever a GPU is ready for work, after finishing its previous job, the next tile in the queue is assigned to it automatically by the dataflow system (Section 3.2.1). Once all tiles are processed they are aggregated with a weighted interpolation operator with weights depending on the distance from the tile boundary. This results in a unique maximum water depth for every location in Austria. Finally, polygons of the inundated areas are delineated from the cells where the maximum water depth exceeds 5 cm.

3.3 Results and discussion

3.3.1 Model runtimes

An overview of the average model runtimes per km² of simulated wet area and the average simulated times for the regions of Austria is given in Table 3.1. The model runtime is defined as the cumulative wall clock time that a single GPU needs to process the specified area. The simulated time specifies the duration of the simulated timespan which is given by the duration of the streamflow hydrographs inside the domain and is larger in regions with lakes, e.g. in Carinthia and Upper Austria. For a 100-year flood, the accelerated computational model ensures that a tile is processed with a runtime of a quarter of the maximum hydrograph duration in average. With a cluster of 10 GPUs the actual model runtime is approximately one tenth of the runtime specified in Table 3.1 resulting in an overall runtime of not even a month for all of Austria.

For the tiles of Upper Austria, which are shown in Fig. 3.6, the model runtimes per tile (for one GPU) are displayed in Fig. 3.11a. Tiles that are covered by large inundated areas require longer runtimes, as can be seen by comparing tiles A, B and C in Fig. 3.11b. In tile A, more than 20 million cells are wet, i.e. an area of 80 km² is flooded. Only tiles with large lakes differ from the general pattern, e.g. in tile C
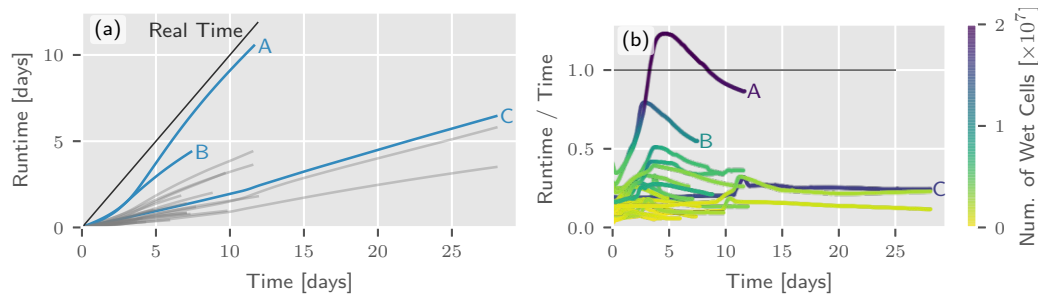
Fig. 3.11. (a) Model runtimes for each of the 25 tiles of Upper Austria for a 100-year flood. Simulation of a tile is performed on a single GPU. (b) Depending on the number of cells and the wave speeds inside these tiles, the simulation of a single tile is between real time and 20 times faster than realtime. The number of wet cells in a tile ranges between 1 and 20 million.
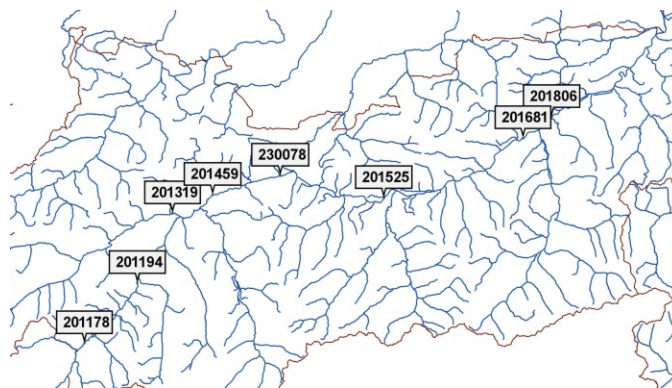

Fig. 3.12. Locations of the stations in Tyrol.

the lake Attersee is responsible for a wet area of 46 km^2. The ratio between model runtime and simulated time in Fig. 3.11b does not not show any kinks indicating that no high speeds occur which shows the robustness of the underlying scheme. As a side note, doubling the resolution increases the runtime by a factor of 5 to 7 times (Horváth et al., 2020). The factor is larger than 4 because of the shorter timestep according to the Courant–Friedrichs–Lewy (CFL) condition.

3.3.2 Comparison with measured rating curves

To validate the accuracy of the simulations, we compare them with measured rating curves at eight stream gauges along the Inn river (locations in Fig. 3.12; rating curves in Fig. 3.13), where measured river bed profiles exist. Very good agreement is found for the top six gauges and slightly poorer agreement is found for Jenbach-Rotholz and Brixlegg. The rating curve of Jenbach-Rotholz shows a bias of around 30 cm which may be due to an inaccurate representation of the measured river profiles in the neighborhood of the gauge. Additional surveys would be needed to shed light
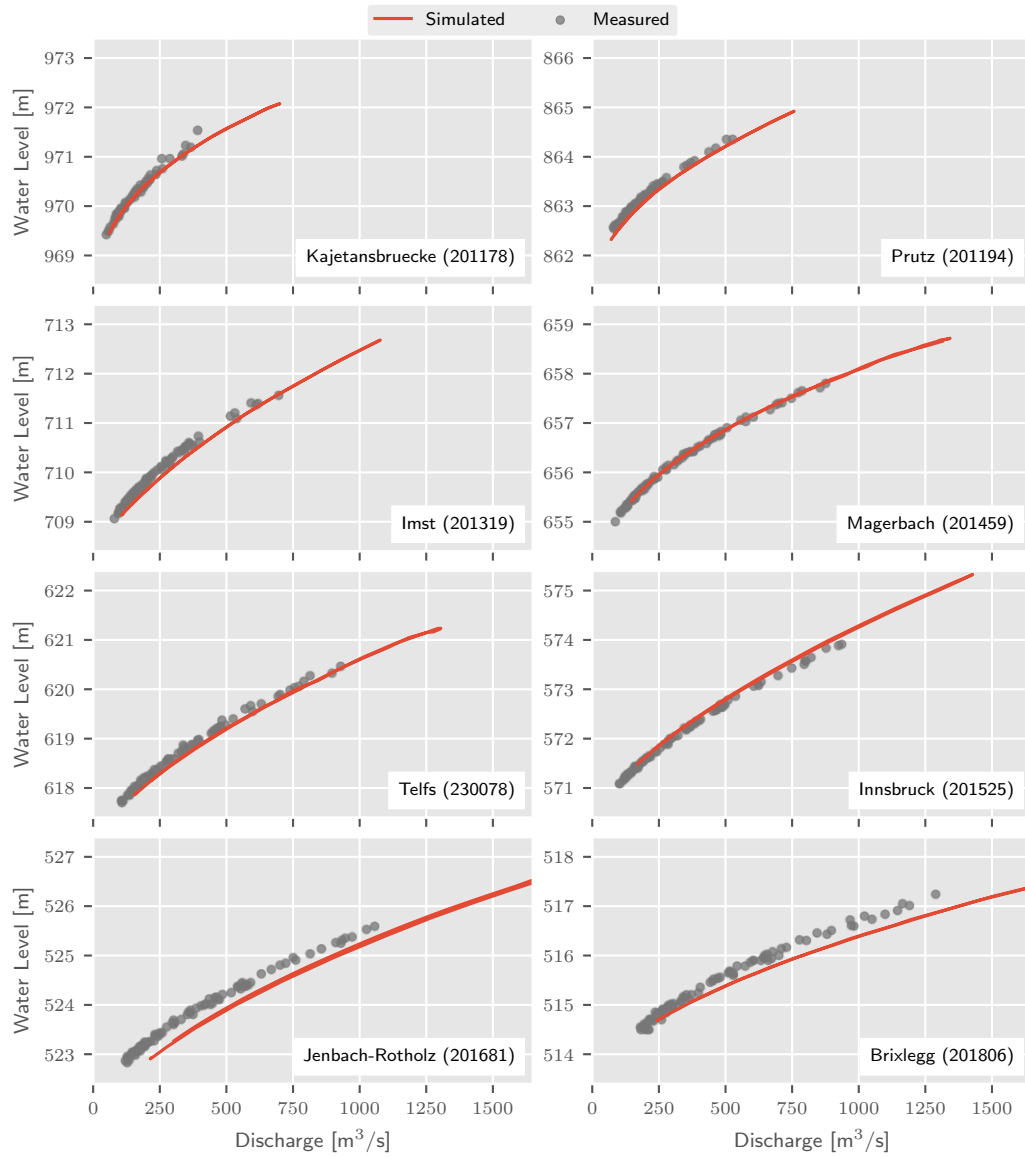
Fig. 3.13. Simulated (red lines) and observed (gray points) discharges and water levels at eight Inn gauges in Tyrol. The reference measurements are monthly maxima collected between 2010 and 2017. Catchment areas of the gauges range from 2162 to 8504 km^2. Station names and numbers are given in the panels.

on this issue, but this is beyond the scope of this article. At Brixlegg, simulated water levels tend to deviate from measured water levels for high discharges. In this case, an inaccurate representation of the flow at several bridges downstream of the gauge explains the low simulated water levels at high flows, since bridges are not explicitly considered in the simulations. Another reason may be an underestimation of the channel roughness which might be addressed by local recalibration.

3.3.3 Comparison with local flood hazard maps

For a spatially distributed validation, we compare the simulated inundated areas against local flood hazard zones, which have been developed in local studies for individual river reaches and approved by the respective authorities. Both the local hazard polygons used as reference (R) and the simulated flood zones are sampled on a 8 by 8 m^2 grid. This results in two possible states for each cell in the reference benchmark data, either wet (R_1) or dry (R_0), if the reference polygons covers more or less than half of the respective grid cell. In the model M, a cell is considered wet (M_1) if a threshold of 5 cm is exceeded at the cell center, otherwise it is dry (M_0). Four performance measures are used. The first is the hit rate (HTR), defined by the number of cells that are wet in both the model and the reference over the number of wet cells in the reference data, i.e.

$$\text{HTR} = \frac{|M_1 R_1|}{|R_1|} \in [0, 1]. \tag{3.6}$$

The hit rate provides information whether the model can correctly replicate the wet cells, ignoring however if the model overpredicts flood extents. The false alarm ratio (FAR) accounts for the overprediction of the flood extent as it is directly proportional to the number of false alarms, i.e. cells wet in the model but dry in the reference data.

$$\text{FAR} = \frac{|M_1 R_0|}{|M_1|} \in [0, 1]. \tag{3.7}$$

A FAR equal to zero indicates that there are no false alarms. The critical success index (CSI) provides a measure of fit by relating the correctly predicted wet cells to the total number of wet cells in either model or reference or both, i.e.

$$\text{CSI} = \frac{|M_1 R_1|}{|M_1 R_1 + M_0 R_1 + M_1 R_0|} \in [0, 1]. \tag{3.8}$$

A CSI of one describes a perfect match of the model flood extents and the reference data. Finally, the error bias (EBS) shows if a model tends towards overestimating (EBS greater than one) or underestimating (EBS smaller than one) flood extents. The error bias describes the number of false alarms over the number of cells that the model missed, i.e.

$$\text{EBS} = \frac{|M_1 R_0|}{|M_0 R_1|} \in [0, \infty]. \tag{3.9}$$

Table 3.2. Performance metrics for Austria's regions for a 100-year flood. The metrics include the critical success index (CSI), hit rate (HTR), false alarm ratio (FAR), error bias (EBS), the area $A_{M_1 R_1}$ that is wet in both the model and the reference, and the maximum and median of the catchment areas A_C.

Region	CSI	HTR	FAR	EBS	$A_{R_1 M_1}$ [km^2]	Max. A_C [km^2]	Median A_C [km^2]
Carinthia	0.71	0.84	0.18	1.13	113.8	7065.8	205.2
Lower Austria	0.68	0.88	0.25	2.48	630.7	130804.6	123.7
Salzburg	0.60	0.71	0.21	0.64	54.4	6124.1	181.0
Styria	0.73	0.81	0.12	0.55	380.5	9829.6	95.3
Tyrol & Vorarlberg	0.61	0.76	0.23	0.95	118.0	9531.1	96.2
Upper Austria	0.72	0.81	0.14	0.66	279.3	92515.6	74.7

Not all simulated rivers are covered by the reference flood hazard maps, thus a buffer zone around rivers covered in the reference flood polygons is computed. The buffer zone width w_b depends on the catchment area A_c, i. e. $w_b = 200 + 15\sqrt{A_c}$. Furthermore, lakes and buildings are excluded in the buffer zone for a fair comparison. Model evaluation was subsequently restricted to this buffer zone.

For Austria, a critical success index (CSI) score of 0.69 and a hit rate of 83 % is achieved. In Table 3.2 these performance measures are evaluated per region. The CSI ranges between 0.61 and 0.74, the highest value is achieved in Styria, the lowest in Salzburg. The hit rate ranges between 0.71 and 0.88, the highest rate is achieved in Lower Austria. The false alarm ratio (FAR) ranges between 0.11 in Styria and 0.24 in Lower Austria. In Lower Austria, hit rate, FAR, and error bias are high due to a modest overestimation of inundated areas in the large floodplains along the Danube and its tributaries. In Styria, the good fit may be explained by the fact that rivers flow mostly through natural floodplains in hilly lowlands or alpine valleys. In Carinthia, Tyrol and Salzburg the floodplains lie in clearly defined alpine valleys where the hinterland is often protected by highways used as levees. These levees frequently have small openings for tributaries or streets, which can be closed if a flood only occurs at the main river, and are therefore mostly considered closed in the reference flood maps. However, in the proposed regional approach used here, they remain open to facilitate free flow of the tributary. Thus, model performance is worse in alpine valleys where rivers are constrained by highways used as levees, e. g. Salzburg and Tyrol, than in regions where most levees do not have a secondary purpose, e. g. in Lower and Upper Austria. These findings suggest that accurate hydrodynamic modeling of rivers constrained by complex defensive protection measures is more involved than that of rivers flowing through natural floodplains.

For a historical reach-scale scenario with manual calibration of roughness parameters, a CSI value of 0.89 against observed high water marks was reported in Echeverribar et al. (2019). Aronica et al. (2002) report CSI values of 0.7 to 0.85 for the best pick of ensemble scenarios. Thus, CSI values of 0.9 seem to represent an

upper limit for local models. For two continental-scale models (Alfieri et al., 2014; Wing et al., 2017), CSI values are in the range of 0.44 to 0.65, and 0.51 to 0.9, respectively. However, comparisons across regions need to be considered in light of the complexity of the floodplain topography, e. g. if the floodplain is defended or developed, as it has an effect on the model performance (Wing et al., 2017).

Fig. 3.14a shows the CSI values aggregated on a grid with 2.5×2.5 km^2 cells for Tyrol. Illustrative examples of the inundated areas of the model and the reference dataset are shown in Fig. 3.14b–d. In the following, we give reasons for the differences of the two data sets in order of their importance.

First, the inundated areas of the reference flood hazard maps are constructed for single reaches using simulations that are mass preserving. Typically, in these simulations the discharge of the main stream corresponds to that of the return period of the scenario, while the discharges of the tributary are reduced to the extent to make the confluences mass conserving. Normally, discharges of the tributaries correspond to return periods of 3 to 5 years, while the main stream maintains a 100-year flood quantile. The reference areas thus describe a realization of a single possible event. In contrast, the proposed model represents a regional pattern of the ensemble of multiple hypothetical events for a water level consistent with a 100-year flood quantile everywhere (Fig. 3.8a). Thus, in our simulations inundated areas tend to be larger upstream of confluences, and smaller downstream than in the reference map. This is particularly apparent in Fig. 3.14b,c.

Second, rivers exist that are included in the dataset used here but are not included in the reference dataset and vice versa. Modeled inundated areas of tributaries are sometimes inside the buffer zone even if they are not included in the reference flood hazard maps. In this case, flooding of small rivers in the present model are incorrectly treated as false alarms.

Third, the DTMs are different as the data source and date of the ALS campaigns are not the same. The reference flood hazard maps include underpasses which are considered closed in the reference but open in our model and vice versa, thus causing differences in the flooded areas as is shown in Fig. 3.14d. In general, levees are resolved and protected areas remain dry (Fig. 3.14b). In rare cases, mobile walls or concrete walls with a width smaller than 2 m, which are resolved in the reference data set but not here, cause an overestimation of wet areas. In general, uncertainties are larger in urban areas, which is also in line with the findings of Dottori et al. (2013), Wing et al. (2017), and Annis et al. (2020).

As the reference flood hazard maps are also created from a shallow water model in addition to comparisons with observed flood cases, and some of the data are shared between the models (e. g. river bed), this test is not fully independent and may not reveal all the biases. A validation against remotely observed inundation patterns, observed flood marks or against validation claims of individual inundated buildings could help to further improve the modeling approach (Wing et al., 2021; Zischg et al., 2018).
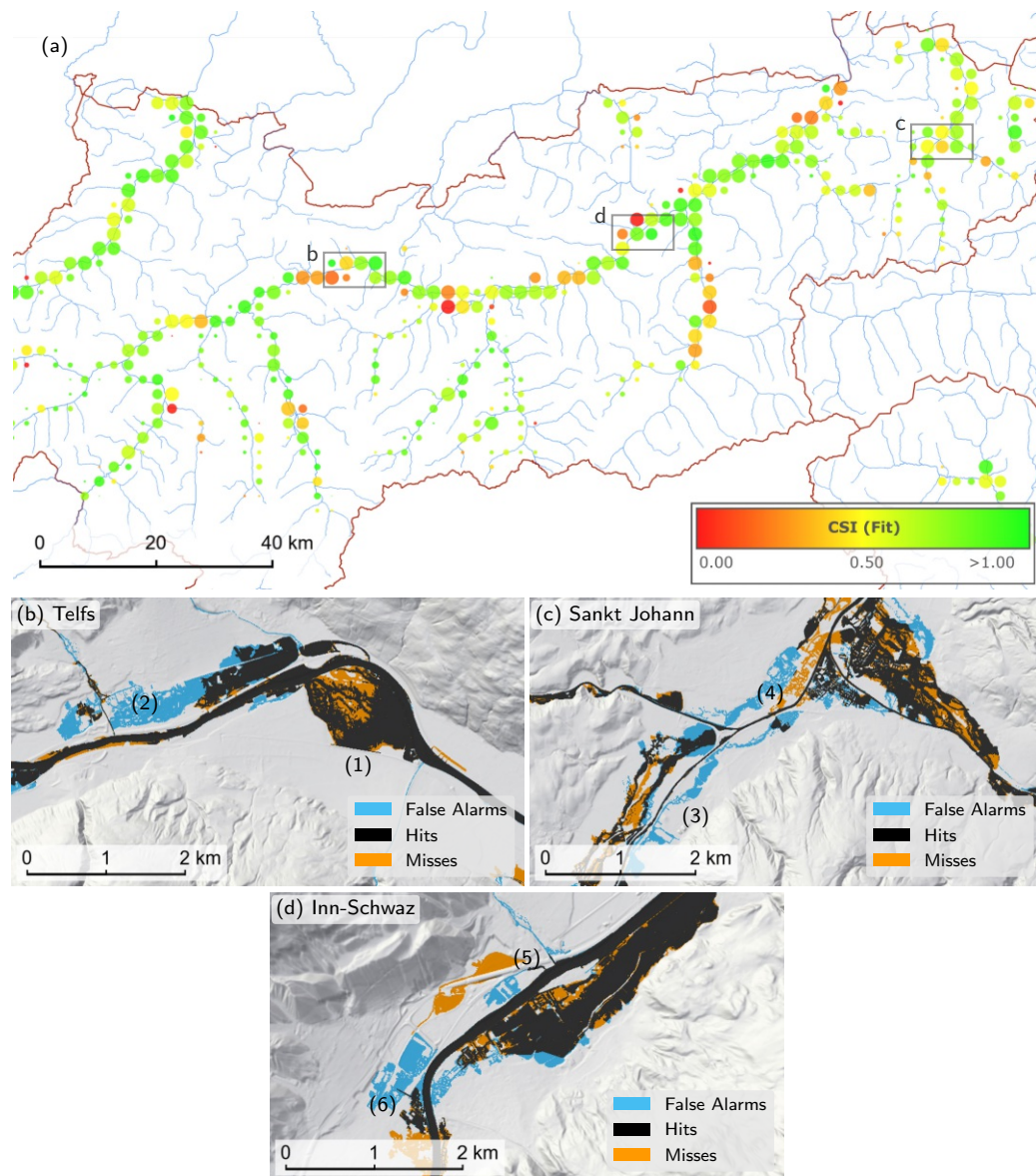
Fig. 3.14. (a) Critical success index (CSI) scores in Tyrol aggregated on a 2.5 by 2.5 km² grid. (b) Both models resolve levees (1) at the Inn around Telfs, but the adopted regional model causes larger inundation areas for the northern tributaries (2). (c) In Sankt Johann, flooded areas deviate due to the proposed regional modeling approach including the adjustments. Upstream of the confluence the flood quantiles are higher than those of the local reference dataset resulting in larger modeled indundation areas (3),(4). (d) At the Inn in Schwaz an underpass is included in the reference dataset, but not in the DTM used here (5) and vice-versa (6).

3.4 Discussion

Previous large-scale flood hazard simulations have often used coupled 1D/2D models (Falter et al., 2016) or resolutions too coarse to explicitly resolve fine structures, e.g. levees and small rivers, in the terrain model (Alfieri et al., 2014; Wing et al., 2017). A resolution of 2 m as adopted in this study allows for a direct incorporation of such terrain features. As a consequence, additional techniques, such as subgrid simulation or downsampling algorithms (Neal et al., 2012; Schumann et al., 2014), are not required. Due to the high resolution openings in levees, e.g. street underpasses, can be represented explicitly. This opens up new questions regarding the modeling of underpasses since, without additional information, it is not clear from the DTM whether they will be closed or not in an emergency case. Overall, the direct inclusion of levees and buildings enables a detailed representation of flow in urban regions. The high detail also allows for the direct estimation of building damage and other socio-economic impacts (Ernst et al., 2010).

In these types of large-scale applications, the storage capacities needed for the entire domain almost always exceeds what can be accomodated on a single computational device, so some tiling is always necessary. One option is to couple the subdomains through overlapping halo and ghost cells and perform tightly coupled simulations where the state variables are exchanged at every simulation time step (Xia et al., 2019; Morales-Hernández et al., 2021). For example Xia et al. (2019) distributed one simulation run for a catchment with a size of 2500 km^2 and a resolution of 5 m (i.e. 100 million cells) on several GPUs. However, this tightly coupled approach tends to increase runtimes as the global timestep is restricted by the highest numerical speed in all the subdomains due to the CFL condition. This introduces a synchronisation barrier at every time step of the hydraulic simulation. Moreover, when simulating multiple non-overlapping catchments, every catchment needs to be simulated for the maximum flood duration of the entire region. Thus, the runtime tends to increase even further with the number of subdomains. In light of these issues, we favor the proposed less tightly coupled approach where the domain is subdivided into tiles, each of which is simulated independently and in parallel on one GPU. Consequently, differences emerge in the simulated wet areas where the tiles overlap. Occasionally, they are noticeable, for example if the BCs are poorly estimated, but in general the differences in the water depths are in the order of centimeters and therefore not problematic.

In the proposed model the region of interest is tesselated into rectangular tiles rather than into individual river reaches, as for example in Sampson et al. (2015), Wing et al. (2017), and Bates et al. (2021). The proposed approach allows the simulation of flood discharges associated with a consistent return period across all river reaches. As a consequence the simulated flood areas do not correspond to a possible event, but rather represent the combined result of a multitude of events. We consider this an attractive alternative to long-term stochastic simulations (e.g. (Falter et al., 2015)), because of the much faster runtimes. The application of a probabilistic sampling approach (e.g. with copulas (Bender et al., 2016)) to

numerous confluences in ungauged catchments requires thousands of simulations which would render the spatial resolution adopted here unfeasible.

3.5 Conclusion and perspectives

In this paper, we present a modeling framework for large-scale hydraulic simulations of river floods. With a focus on accuracy and simulation speed, we employ a second-order finite-volume scheme that discretizes the full, transient shallow water equations (Buttinger-Kreuzhuber et al., 2019) implemented on graphics processing units (GPUs). Inundated areas are simulated for the whole of Austria (84000 km^2) with quadratic cells of 2×2 m^2. We achieve local relevance through the number of included streams and through the high resolution of the DTM and the simulation grid, which allows explicit representation of dams, buildings and small rivers. Inflow boundary conditions (BCs) are automatically prescribed from hydrologic data. Hydraulic sub-models of high-head power plants and culverts provide an accurate description of local effects. Dynamic outflow BCs account for instationary two-dimensional effects, e. g. from retention basins.

In order to efficiently map the inundated areas, we propose a workload distribution based on simulation tiles that allows adaptation to the capabilities of the individual computational devices. The approach allows for arbitrarily placed tiles with a domain size not constrained by hydrological data, but only bound by current hardware limitations. For tiles with sizes of around 600 km^2, the GPU-accelerated robust hydraulic engine ensures fast hydrodynamic simulations. For all of Austria, 182 tiles are processed in parallel on a distributed setup of 10 GPUs. The effective runtime for the entire region of Austria is less than a month for a 100-year flood simulation, which results in 3532 km^2 of inundated areas or 883 million wet pixels.

By providing additional adjustment source terms to the hydraulic engine, a novel approach to maintain consistent flood return periods across the river network is presented. With these adjustments, we are able to simulate all rivers in a tile in one run. The adjustments violate mass conservation at confluences, thus results deviate from conventional mass-conserving flood hazard maps. This approach provides an efficient way to map inundated areas at confluences without the need for ensemble simulations.

The automation framework Visdom (Waser et al., 2011) controls the complete dataflow including the automated generation of the inputs to the hydraulic simulations, their execution, and the post-processing without the need for manual interventions. Manual work is only required for a few specific tasks, e. g. tiling of the region of interest or providing data corrections. A flexible setup ensures that changes and manual corrections are automatically integrated and propagated forward to the simulations.

We regard the presented model as a prototype for a new standard that brings local relevance to large-scale high resolution modeling. The simulated rating curves show good agreement at stream gauges when compared with measured rating curves.

The model delivers flood hazard maps comparable to flood hazard maps created in local studies with a critical success index (CSI) score of 0.69 and a hit rate of 83 % across Austria. The individual CSI scores across Austria's regions range from 0.61 to 0.74. Deviations from local reference maps emerge due to the consistent flood return periods or due to differences in the DTM, e. g. open underpasses. In future work, uncertainties in the model cascade and the effects of climate change could be addressed. One possibility would be ensembles of simulations that investigate changing streamflow conditions from climate projections.

4 An integrated GPU-accelerated modeling framework for high-resolution simulations of rural and urban flash floods

The present chapter corresponds to the following scientific publication in its original form:

A. Buttinger-Kreuzhuber, A. Konev, Z. Horváth, G. Blöschl, and J. Waser (2021). An integrated GPU-accelerated modeling framework for high-resolution simulations of rural and urban flash floods. To be submitted to Environmental Modelling & Software.

Abstract

This paper presents an integrated modeling framework aiming at accurate predictions of flash flood hazard from rainfall in rural and urban settings. The spatially distributed runoff model integrates an infiltration component based on the Green–Ampt equation, an interception component, and a surface flow routing component. The surface flow is discretized either by a first-order or by a second-order accurate scheme solving the full shallow water equations. For urban systems the model is coupled with the Storm Water Management Model (SWMM). The model is validated and tested on laboratory, rural and urban scenarios. In terms of the workload–accuracy tradeoff, the first-order scheme outperforms its second-order counterpart. A GPU implementation of the runoff model yields speedups of 1000 times compared to a sequential CPU implementation. The GPU-accelerated modeling framework simulates flash floods at resolutions of 1 m for areas up to 200 km^2 in realtime.

4.1 Introduction

Floods are increasing in many parts of the world due to climate and land use change (Chen et al., 2018; Blöschl et al., 2019) causing disproportionally high damage in urban regions (Jongman, 2018). To mitigate future flood damage, detailed models that assist in assessing the flood hazard spatially are crucial (Rosenzweig et al., 2021). In contrast to lumped models, spatially distributed models allow for an explicit representation of spatial variations and inhomogeneities in input data, such as topography, vegetation, soil characteristics, and urban features. Notwithstanding scale issues (Grayson and Blöschl, 2001), there is a lot of value in spatially distributed high-resolution modeling for management purposes. However, higher resolutions lead to slower simulations. In addition, ensemble simulations that quantify the uncertainty of the predictions and provide insights into the effects of parameter

variation increase the computational burden even further. Thus, the challenge is to advance the capabilities of numerical modeling while balancing simulation performance and model accuracy.

To accurately represent the topography, the resolution of the simulation grid should be chosen accordingly. As a rule of thumb, terrain features should be covered by at least 3 cells to be represented explicitly (Gallegos et al., 2009; Fewtrell et al., 2011; Horváth et al., 2020). For urban areas, a resolution of 2 m or less is considered necessary to accurately represent buildings, curbstones, and other features (Fewtrell et al., 2011; Dottori et al., 2013; Xing et al., 2018). Moreover, simulations at submeter resolutions are useful for assessing the benefits of small-scale alteration of street topography for flood risk management purposes at low costs (Almeida et al., 2016).

The shallow water equations (SWEs) are typically used for describing surface flow. Due to the Courant–Friedrichs–Lewy (CFL) condition, a high spatial resolution requires a fine temporal discretization. Therefore, the total amount of computational work increases and in turn slows down simulation runs. To accelerate the simulations, one possibility is to simplify the shallow water model, for example, using diffusive wave (sometimes also called zero-inertia) or kinematic wave approximations (Neal et al., 2012; Le et al., 2015; Fry and Maxwell, 2018; Yang et al., 2020). For urban regions, the full or dynamic SWEs in combination with shock capturing schemes are able to reproduce observed hydraulic behavior and velocities more accurately than simplified models (Kvočka et al., 2015; Costabile et al., 2020). Cozzolino et al. (2019) conclude that the preferred model for floodplain simulations should be the full 2D SWEs as simplified models often suffer from a poor representation of receding flows and bed discontinuities. Still, issues such as wetting and drying over complex terrain pose a numerical challenge and constitute an active area of research (Chen and Noelle, 2017; Xia et al., 2017; Buttinger-Kreuzhuber et al., 2019). If not treated properly, numerical instabilities occur and lead to slow simulations. The full SWE offer a model to simulate both complex open channel hydrodynamics and overland flow processes (Costabile et al., 2013; Fernández-Pato et al., 2016), in particular at high resolutions (Caviedes-Voullième et al., 2020). Recent studies (Costabile et al., 2017; Aricò and Nasello, 2018; Caviedes-Voullième et al., 2020) point out that solvers for the full SWEs might in fact require less computational time than their zero-inertia counterparts. A more promising way to achieve computational speedups is the execution in a massively parallel fashion on supercomputers (Noh et al., 2018; Kuffour et al., 2020) or on graphics processing units (GPUs) (Lacasta et al., 2015; Le et al., 2015; Xing et al., 2018; Xia et al., 2019; Morales-Hernández et al., 2021). Cutting-edge flash flood models are on the verge of handling resolutions of 5 m for large regions of up to 2500 km^2, or, 100 million cells (Xia et al., 2019). Traditionally, cities are split into multiple smaller simulation regions that tend to underestimate inundation (Xing et al., 2018). Thus, high-resolution simulations at large scales, e. g. spanning entire cities, are needed.

A variety of infiltration models exist, including the empirical Soil Conservation Service (SCS) curve number method (Chow et al., 1988; Aureli et al., 2020), the

empirical Horton model (Fernández-Pato et al., 2016; Fernández-Pato and García-Navarro, 2018), the semi-empirical Green–Ampt model (Fiedler and Ramirez, 2000; Simons et al., 2013; Delestre et al., 2017; Fernández-Pato et al., 2016), and more complex models such as Richards equation (Maxwell, 2013; Le et al., 2015; Kuffour et al., 2020) although capturing macropore flow (Zehe et al., 2007) remains a challenge. The model's ability to capture the local effects of green infrastructure (GI), such as green roofs, rain gardens, or bioswales, is important in urban flood resilience planning (Berland et al., 2017; Fry and Maxwell, 2018; Rosenzweig et al., 2021). For urban flood hazard modeling, the flow in sewer systems and its interaction with the overland flow may be relevant. The Storm Water Management Model (SWMM) is an established tool for routing stormwater in sewer systems. It is developed by the Environmental Protection Agency (EPA) as an open-source software package (Rossman, 2017). A widely used approach to bidirectionally couple urban drainage networks to overland flow are dual drainage models (Leandro and Martins, 2016; Yang et al., 2020; Li et al., 2020; Rosenzweig et al., 2021). The interaction terms are commonly based on the water level differences between the sewer nodes and the surface water (Djordjević et al., 2005; Chen et al., 2016; Rubinato et al., 2017; Fernández-Pato and García-Navarro, 2018).

In this paper, we present a coupled modeling framework for fast simulations in urban and rural settings. The framework includes several components considered relevant in rainfall–runoff modeling and flash flood hazard assessment, that is, spatially distributed interception and infiltration, an accurate representation of overland flow, and subsurface flow in sewer networks. We go beyond current modeling practice by using both a spatially distributed GPU-accelerated infiltration model and a fully bidirectional coupling of the sewer network accounting for drains and overflows at larges scales and very high resolutions. We validate and test the framework in laboratory, rural and urban scenarios. We answer the question whether first-order or second-order schemes in the surface flow discretization of the full 2D SWEs should be favored in terms of the workload–accuracy tradeoff. Moreover, we highlight the influence of resolution and of the individual model components. Finally, we address the extent of computational acceleration on a modern GPU for high-resolution simulations of entire cities.

4.2 Methods

4.2.1 Surface flow model

The full shallow water equations (SWEs) are used to describe the surface flow and may be written in vector form as

$$\partial_t \mathbf{U} + \partial_x \mathbf{F}\left(\mathbf{U}\right) + \partial_y \mathbf{G}\left(\mathbf{U}\right) = \mathbf{S}_b\left(\mathbf{U}, b\right) + \mathbf{S}_f\left(\mathbf{U}\right), \tag{4.1}$$

where $\mathbf{U} = [h, hu, hv]^T$ is the vector of conserved variables, h represents the water height, hu is the discharge along the x-axis, and hv is the discharge along the y-axis.

$\mathbf{F}$ and $\mathbf{G}$ are the flux functions,

$$\mathbf{F} = \begin{bmatrix} hu \\ hu^2 + \frac{1}{2}gh^2 \\ huv \end{bmatrix}, \quad \mathbf{G} = \begin{bmatrix} hv \\ huv \\ hv^2 + \frac{1}{2}gh^2 \end{bmatrix}. \tag{4.2}$$

The bed slope term $\mathbf{S}_b$,

$$\mathbf{S}_b = \begin{bmatrix} 0 \\ -gh\partial_x b \\ -gh\partial_y b \end{bmatrix}, \tag{4.3}$$

models the fluid's acceleration due to the gravitational forces. The friction term $\mathbf{S}_f$,

$$\mathbf{S}_f = \begin{bmatrix} 0 \\ -gn^2 h^{-1/3} u\sqrt{u^2+v^2} \\ -gn^2 h^{-1/3} v\sqrt{u^2+v^2} \end{bmatrix}, \tag{4.4}$$

accounts for the bed friction. Here, u and v are the average flow velocities in x and y directions respectively, g is the gravitational constant, b is the bathymetry (assumed to be time-independent), and n is the Manning friction coefficient.

To integrate the interception and infiltration processes of the runoff model and the sewer model with the surface flow, coupling terms $\mathbf{S}_r$ and $\mathbf{S}_s$, respectively, are added on the right hand side of Eq. (4.1). The coupling term for the sewers $\mathbf{S}_s$ accounts for the specific sewer exchange discharge q_e (m/s). The source terms $\mathbf{S}_r$ and $\mathbf{S}_s$ are given by

$$\mathbf{S}_r = \begin{bmatrix} r_e(t) \\ 0 \\ 0 \end{bmatrix}, \text{ and } \mathbf{S}_s = \begin{bmatrix} q_e(\mathbf{U}) \\ 0 \\ 0 \end{bmatrix}. \tag{4.5}$$

The runoff rate r_e (m/s) is the difference between the effective precipitation rate and the effective infiltration rate. Its precise application is defined in Section 4.2.4.

4.2.2 Spatio-temporal discretization of the surface flow

For the spatial discretization of the SWEs, the finite volume method (FVM) was chosen on a uniform Cartesian grid. The FVM discretizes the conserved variables $\mathbf{U}$ as cell averages yielding a system of ordinary differential equations for the cell averages $\mathbf{U}_{j,k}(t)$. For the simulation of the overland flow, we employ either a first-order accurate or a second-order accurate scheme. The first-order CN scheme (Chen and Noelle, 2017) preserves still-water steady states, i.e. it is well-balanced. Moreover it enables a better handling of flow states across bed discontinuities than the original hydrostatic reconstruction (HR) scheme proposed by Audusse et al. (2004). A second-order accurate extension of the first-order CN scheme is presented in

(Buttinger-Kreuzhuber et al., 2019), to which we will refer as the BH scheme. The second-order accuracy in space is achieved through a minmod limiter. The minmod parameter is set to 1 in order to ensure robust and fast simulations (Horváth et al., 2020). At wet-dry boundaries only the velocities are set to zero below a cut-off water depth threshold. In the simulations this threshold is set to 0.1 mm. The surface flow is discretized in time by the explicit Euler's method for the first-order CN scheme with a CFL constant of 0.5 to guarantee numerical stability and non-negativity of the water depths. The second-order BH scheme is integrated in time with Heun's method and the CFL constant is set to 0.25. Both schemes are mass conserving. The friction source term $\mathbf{S}_f$ is evaluated in a semi-implicit manner by splitting it into a coefficient-wise product of an implicitly evaluated state and an explicitly evaluated friction term $\widetilde{\mathbf{S}}_f$ (Brodtkorb et al., 2012; Buttinger-Kreuzhuber et al., 2019).

4.2.3 Runoff model

The spatially distributed runoff simulation integrates the surface flow routing component with an interception and an infiltration component determining the effective surface runoff. First, part of the rain is stored in the canopy of vegetation through interception. Second, infiltration occurs as surface water percolates into permeable soils. The remaining water effectively materializing during a rain event runs off the surface as overland flow.

The rainfall intensity is given by a time- and space-dependent precipitation rate p. The integrated interception component reduces the effective precipitation and accounts for micro-topographic depressions and losses due to vegetation. The cumulative interception $I(t)$ until time t is modeled with a constant non-negative rate i until a predefined storage capacity I_S is reached. Thus, the spatially distributed effective precipitation rate is given by

$$p_e(t) = \begin{cases} p(t) - i & \text{if } I(t) < I_S, \\ p(t) & \text{else.} \end{cases} \tag{4.6}$$

The infiltration process is modeled by the Green–Ampt equation, the cumulative infiltration F up to time t is

$$\int_0^{F(t)} \frac{F}{F + (\psi + h)\,\Delta\theta}\, dF = \int_0^t K_s\, dt, \tag{4.7}$$

where K_s is the saturated hydraulic conductivity. The difference $\Delta\theta$ between the initial water content and the saturated water content of the soil is usually called soil porosity. The suction head ψ represents the capillary attraction of the water towards the soil voids. Solving Eq. (4.7) for the infiltration rate f, the time derivative of F, we obtain

$$f(t) = \frac{dF}{dt} = K_s \left[\frac{(\psi + h)\,\Delta\theta}{F(t)} + 1 \right]. \tag{4.8}$$

The proposed dynamic infiltration model accounts for the surface water pressure via the surface water height h. A shortcoming of the presented Green–Ampt model is the inability to account for multi-layered soils, limited storage capacity, soil water redistribution in dry phases and macropores. Extensions to overcome these limitations have been proposed (Corradini et al., 2000; Gowdish and Muñoz-Carpena, 2009; Mohammadzadeh-Habili and Heidarpour, 2015; Leandro et al., 2016).

4.2.4 Temporal discretization of the runoff model

The Green–Ampt (GA) model is discretized in time with the implicit Euler method solving equation (4.8) at every cell for every time step. The infiltration depths F at time step t^{n+1} is given by

$$F^{n+1} = \frac{1}{2}\left(F^n + K_s \Delta t\right)$$
$$+ \frac{1}{2}\sqrt{\left(F^n + K_s \Delta t\right)^2 + 4\, K_s \Delta t\, \Delta\theta\, (h_0^n + \Psi)}. \tag{4.9}$$

We note that, even though the infiltration rate is undefined for $F = 0$, the implicit Euler method yields a well-defined infiltration depth close to zero, in contrast to the explicit Euler method. If the infiltration depth increment ΔF, defined by $\Delta F^n = F^{n+1} - F^n$, exceeds the available surface water depth, it is restricted to ensure a nonnegative surface water depth. The effective infiltration rate is then given by

$$f_e^n = \frac{1}{\Delta t^n}\min(\Delta F^n, h^n), \tag{4.10}$$

where Δt^n is the CFL-limited timestep of the overland flow for timestep n. For the runoff model, it is enough to perform a simple integration for both the effective precipitation and infiltration rate. We combine the precipitation and infiltration increment into a single effective runoff increment Δr_e^n,

$$\Delta r_e^n = \Delta t^n \left(p_e^n - f_e^n\right). \tag{4.11}$$

The overland flow and runoff models are tightly coupled, every step in the surface flow simulation is synchronized with the computation and application of the runoff update.

As the surface water depths and the infiltrated depths might be orders of magnitude larger than the runoff increment Δr_e, we add the runoff increment using the compensated summation principle (also known as the Kahan summation algorithm). For a precise addition, we add the runoff increment of the current time step to a pending runoff state. Then, the respective parts in the pending runoff state are added to the surface water depths and the infiltrated depths. The high-order difference between the updated and the previous surface depth is then subtracted from the pending runoff state. The low-order difference, which is too small for being accounted for in the addition to the surface depth, remains in the pending runoff state and is included in future time steps. With this technique, we keep track of the lower-order part of the runoff increments over the entire simulation period, which efficiently guarantees mass conservation.

4.2.5 GPU implementation of the runoff model

The spatial discretization of the surface flow with the FVM enables straightforward parallelization on regular grids, as only neighboring cells need to be considered when computing the next time step. For the first-order CN scheme, only the direct neighbors are accessed. For the second-order BH scheme, the computation of the minmod-limited gradient requires a neighborhood of two cells to be accessed in the four axis-aligned directions. On the GPU, a simulation tile is split into blocks of 16 by 16 cells. This effectively results in 14 by 14 cells for the first-order CN scheme or in 12 by 12 cells for the second-order BH scheme due to the different number of halo cells required. The GPU implementation for the surface flow uses the CUDA platform of NVIDIA and uses shuffles introduced with the Kepler microarchitecture (Horváth et al., 2016). Both the surface state and the infiltration state are stored in single-precision floating-point variables. Due to the use of single-precision floating-point state variables, the memory burden is lower and floating-point operations are faster, even if it requires the compensation technique introduced in the previous section. On a modern GPU with 24 GB of video memory the domain size in our computational model is limited to around 175 million active (wet) cells for the second-order BH scheme with dynamic runoff. For the first-order CN scheme, the domain size is limited to around 225 million active cells as the first-order time integration does not require the storage of an intermediate state.

4.2.6 Sewer network model

In the Storm Water Management Model (SWMM), a sewer network is represented by a set of nodes connected by links (Rossman, 2017). Links transmit pipe discharges Q from one node to another. A so-called node assembly consists of the node and half of the links connected to the node. At each node assembly, the change in the hydraulic head is modeled by the continuity equation. The pipe flow is governed by the transient 1D SWEs and is solved with a finite difference scheme. Thus, at each link, momentum and continuity are conserved, in contrast to the nodes, where only continuity is conserved. The continuous state variables in the time differences are approximated with their average values over the conduit length. SWMM 5.1 uses an implicit backwards Euler method for the time discretization, which is solved iteratively with Picard's method. We use the Preissmann slot model, implemented in the latest version of SWMM 5.1.013, which is integrated in our coupled model setup. SWMM 5.1.013 is written in C++ and is easily incorporated into existing C++ software such as the proposed modeling framework.

4.2.7 Bidirectional sewer–surface coupling

The sewer–surface discharge exchange term depends on the water level at the surface w, the hydraulic head at the manhole H and the bed surface elevation b. In the following, A_m and D_m are the manhole's area and diameter, respectively, d_i is the distance between the surface and the invert level of the pipes entering the node. The

invert level refers to the lowest elevation admitting water flow. Following Djordjević et al. (2005), Chen et al. (2016), Rubinato et al. (2017), and Fernández-Pato and García-Navarro (2018), we distinguish between four cases:

1) inflow into a non-pressurized node,

2) inflow into a pressurized node, where the surface flow depth is small when compared to the node width,

3) inflow into a pressurized node, where the surface flow depth is large when compared to the node width,

4) outflow onto the floodplain.

If the head in the pipe network is lower than the surface elevation, i.e. $H < d_i$, the discharge exchange Q_e (m^3/s) is given by the free weir equation

$$Q_e = -\frac{2}{3} c_{d,w} \pi D_m (2g)^{1/2} h^{3/2}. \tag{4.12}$$

If the head in the pipe network exceeds the surface elevation, i.e. $H > d_i$, the discharge exchange is either given by the submerged weir equation,

$$Q_e = -c_{d,sw} \pi D_m (2g)^{1/2} h (h + d_i - H)^{1/2}, \tag{4.13}$$

as long as $h < A_m/\pi D_m$. If $h \geq A_m/\pi D_m$ the node is considered fully submerged, the submerged orifice equation

$$Q_e = -c_{d,o} A_m (2g)^{1/2} (h + d_i - H)^{1/2}, \tag{4.14}$$

is considered a more appropriate description. For example, for circular manholes, the orifice equation is applied if $h > D_m/4$. The discharge coefficients for the free weir, the submerged weir, and the orifice equations are set to $c_{d,w} = 0.56$, $c_{d,sw} = 0.11$, and $c_{d,o} = 0.2$, respectively (Rubinato et al., 2017). If the head in the pipe system exceeds the water level of the surface flow, an orifice equation is used (Djordjević et al., 2005). Assuming that the surface velocity is negligible, the discharge exchange is given by

$$Q_e = c_{d,o} A_m (2g)^{1/2} (H - h - d_i)^{1/2}. \tag{4.15}$$

This equation also holds for dry surface cells, i.e. when $h = 0$.

With these four cases, all exchange flow conditions are properly handled. A negative exchange discharge Q_e indicates flow into the sewer network from the surface, a positive value indicates sewer overflow. Sewer overflow also occurs if water flow from the roofs of the surrounding buildings exceeds the sewer inflow capacity. Consequently, water spills over at this node. In this case, the roof water is directly added to the sewer overflow and not reduced by the sewer–surface exchange equations, Eqs. (4.12)–(4.15).

The sewer–surface coupling takes place only at the cells where manholes and inlets are connected to the surface. To this end, the geometry of the manholes and inlets is rasterized on the simulation grid. Effectively, at each cell the perimeters and areas of all intersecting manholes and inlets are collected. Furthermore, we also collect the contributions of each cell to each sewer node. Both cases where multiple manholes intersect the same cell, as well as cases where multiple cells contribute to the same node are resolved. For each rasterized cell, we keep track of the corresponding node head by averaging over all nodes connected to the specified cell. The sewer node exchange discharge Eqs. (4.12)–(4.15) are solved on a per-cell basis, where we account for the relative contributions,

$$Q_e = \sum A_{j,k} q_{ej,k}. \tag{4.16}$$

The specific sewer exchange term for the surface model is limited by the water availability in the case of sewer inflow, i. e.,

$$-q_{ej,k} = \min\left(\frac{h_{j,k}}{\Delta t}, -q_{ej,k}\right). \tag{4.17}$$

In time, the sewer network model is interleaved with the surface and runoff model with an a priori defined coupling timestep ΔT_C. If not stated otherwise, it is set to 1 s. A time step of the coupled model is illustrated in Fig. 4.1 and subdivided into the following steps:

1) Exchange sewer-surface coupling data, i.e. provide node heads and pending overflows to the surface flow simulation, and provide exchange discharges to the sewer model.

2) Advance the simulators in parallel from time T^i to $T^i + \Delta T_C$.

3) Compute the exchange data, including reconciliation of applied exchange discharges in both the surface simulator and in the sewer simulator.

Each simulator performs multiple routines at each of these steps (see Fig. 4.1). When coupling data need to be exchanged, the simulators are required to wait for the other simulator at synchronization barriers. Synchronization barriers are set only at the beginning and the end of a coupled simulation time step, but not in the individual simulator's advance methods. The loop for the time steps in the advance step is executed independently of the other simulator. To advance from T^i to $T^i + \Delta T_C$, each simulator only needs the minimal amount of time steps required for its own numerical stability.

For the sewer simulation, the exchange discharges are obtained from the surface simulation and applied to the sewer network. Additional inflows from external sources, e. g. roofs, are applied and compared with the sewer network's inflow capacities. These excess discharges contribute to the pending node overflow. SWMM routes the water flow in the sewer network. Then, the sewer network state (node
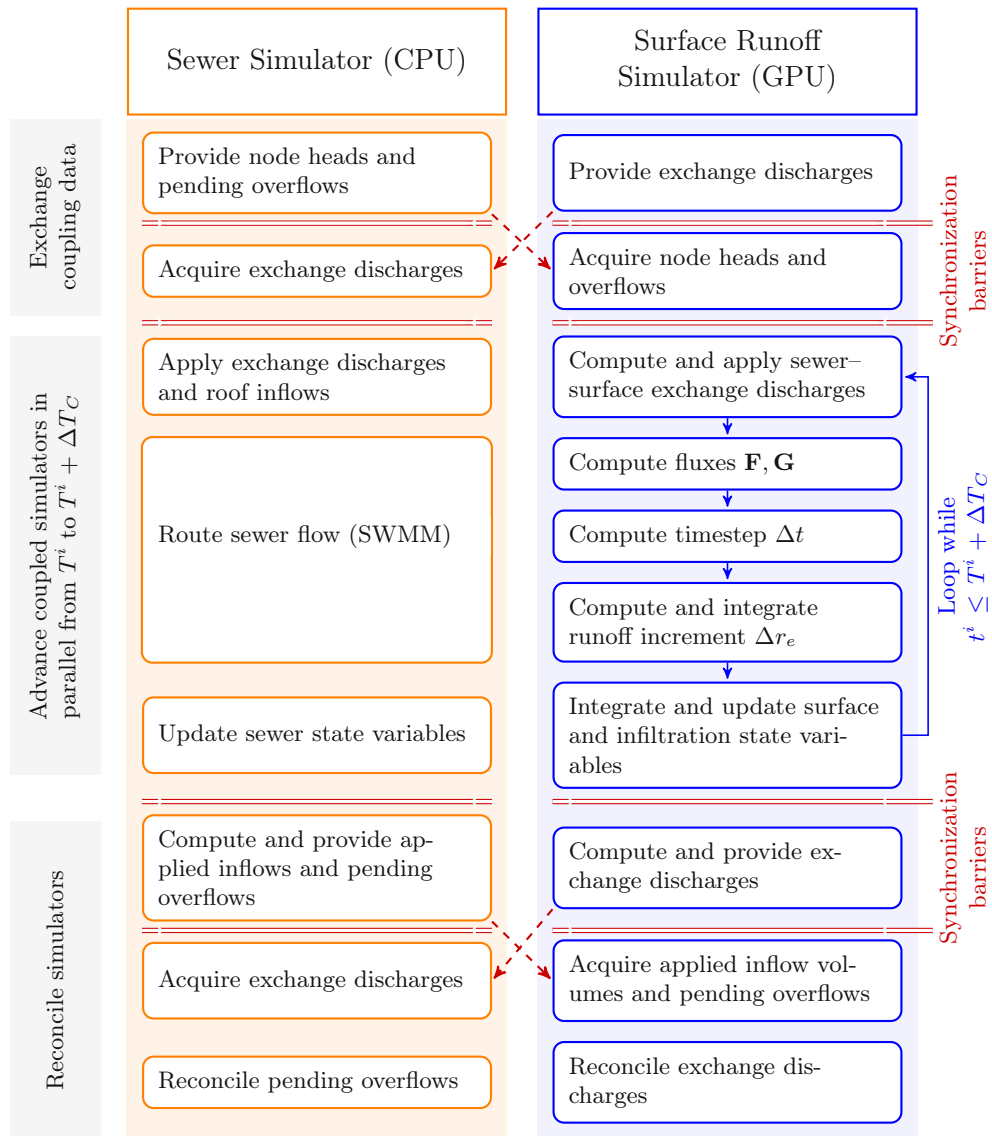
Fig. 4.1. In a single time step of the coupled sewer–surface model, three major substeps (indicated in gray at the left) with associated routines are performed in each simulator. The sewer and the surface simulator are executed in parallel, but they need to be synchronized for data exchange. These synchronization barriers (indicated with double red lines) are needed for data exchange between the two simulators (indicated with the dashed red arrows). With this less tightly coupled approach, each simulator is able to advance independently of the other.

depths and heads, link discharges and volumes, inflow volumes, and pending over-flow volumes) is updated. Pending node overflows and applied inflow discharges are then provided to the surface runoff simulation. In turn, the sewer simulation acquires the exchange discharges applied in the surface simulation. During the parallel execution of the coupling time step, the state of the surface variables remains fixed for the sewer simulation and vice versa. As the sewer inflows computed by the sewer simulation might exceed the available surface water, the discrepancy between the applied inflow in the sewer network simulation and the actual water removed in the surface simulation needs to be resolved. Therefore, a harmonization step is necessary to reconcile mass balance.

For the simulation of the surface flow and runoff, node heads from the sewer simulation are necessary for the computation of the sewer–surface exchange discharges. Once acquired, the surface runoff simulation is able to advance independently of the sewer simulation. The routines in the surface runoff advance step are performed on the GPU and looped until the next coupling time step $T^i + \Delta T_C$ is reached. The surface state variables (water depth and level, surface flow discharges) and the infiltration state variables (infiltration depth, pending runoff) are updated after timesteps Δt^n according to Section 4.2.4. After the loop, the computed and applied exchange discharges are provided to the sewer simulation. In turn, the applied inflow discharges into the sewer network and pending node overflows are acquired. The exchange discharges of the surface runoff simulation are then reconciled with the acquired discharges from the sewer simulation to resolve the discrepancies. This harmonization guarantees that the mass balance errors remain small or vanish for a simulation converging towards a steady state.

The coupled simulation time steps are executed until the simulation end time is reached. As the sewer simulation and the surface runoff simulation are executed in parallel, the execution time of the coupled surface–sewer model is determined by the execution time of the slower simulator and not by the sum of the execution times as it would be the case for a sequential coupled simulation. Usually, the one-dimensional sewer network simulation is faster than the two-dimensional surface flow simulation (Noh et al., 2018).

4.3 Results and discussion

We demonstrate the capabilities of the coupled model on laboratory and real-world test cases. The scenarios include a small-scale rainfall–runoff plot experiment, a rural catchment, and a full-scale urban test case including sewer coupling. More specifically, we simulate the Thiès plot experiment, the HOAL catchment at Petzenkirchen, Austria, and the city of Cologne, Germany. Furthermore, we validate the sewer–surface coupling approach on a laboratory experiment presented in (Rubinato et al., 2017). The validation results for the sewer–surface coupling are in Appendix A1.

The numerical simulations were performed on a desktop PC equipped with 10

Intel i9-9820X cores at 3.3 GHz and 128 GB RAM. The GPU utilized for the test cases was an NVIDIA Titan RTX in TCC mode. It features 4608 CUDA cores and has 24 GB memory. In the following, the term *runtime* describes the cumulative execution time of the simulation measured via wall clock timing. The runtime neither includes the initialization process, such as reading input data, nor postprocessing steps, such as writing results to the disk. However, the GPU runtime includes data transfer between the GPU and the CPU during simulation.

4.3.1 Thiès plot experiment

We validate the model with measurements performed at in Thiès, Senegal, by (Tatard et al., 2008). The experiment was carried out on a 10×4 m^2 plot. The plot has an average slope of 1%, and the resolution of the digital terrain model (DTM) is 0.1 m. Rainfall was simulated with a constant rate of 70 mm/h for a duration of 1 h on the sandy soil. In the reference data set of (Mügler et al., 2011), measurements of mean flow velocities are available at 62 locations across the plot (Fig. 4.2a). Following (Simons et al., 2013), Manning's roughness coefficient was set to a constant value of 0.014 m$^{1/3}$/s throughout the entire plot. We compare the results from the first-order CN and second-order BH scheme for the steady state after 1 h. The simulated water depths show a slightly clearer depiction of the flow paths in the second-order scheme, compare Fig. 4.2b–c. The simulated velocities are shown as arrows in Fig. 4.2b–c for the CN and BH scheme.

In Fig. 4.3a, we compare the simulated velocities with the measured velocities. Second-order schemes are computationally more involved than first-order schemes, but are supposed to yield superior results due to the improved accuracy. The root mean square error (RMSE) of the velocities is defined by

$$\text{RMSE} = \sqrt{\frac{1}{N} \sum_i (v_s^i - v_o^i)^2}, \tag{4.18}$$

where N is the total number of all observed velocities v_o^i. The RMSEs of the velocities are consistently lower for the second-order scheme for all resolutions from 0.05 to 0.25 m, as is shown in Fig. 4.3b, and the achieved RMSE of 0.026 m/s is in line to results in the literature (Tatard et al., 2008; Mügler et al., 2011; Simons et al., 2013; Caviedes-Voullième et al., 2020). However, we emphasize that a proper discretization of the source term is important for the simulation of runoff processes, even more so in the case of first-order accurate schemes. The superiority of the first-order CN scheme above the popular HR scheme (Audusse et al., 2004) is noticeable from the velocity errors in Fig. 4.3a and b. The simulated velocities of the HR scheme are consistently lower than for the CN scheme, as the HR scheme is not able to fully account for the bed slope in the case of shallow flow (Delestre et al., 2012). Switching to second-order accuracy in the HR scheme fixes this issue, albeit at the cost of a higher computational workload. The velocities of the second-order HR scheme are only slightly deviating from the BH scheme, therefore they were excluded from the plots in Fig. 4.3.
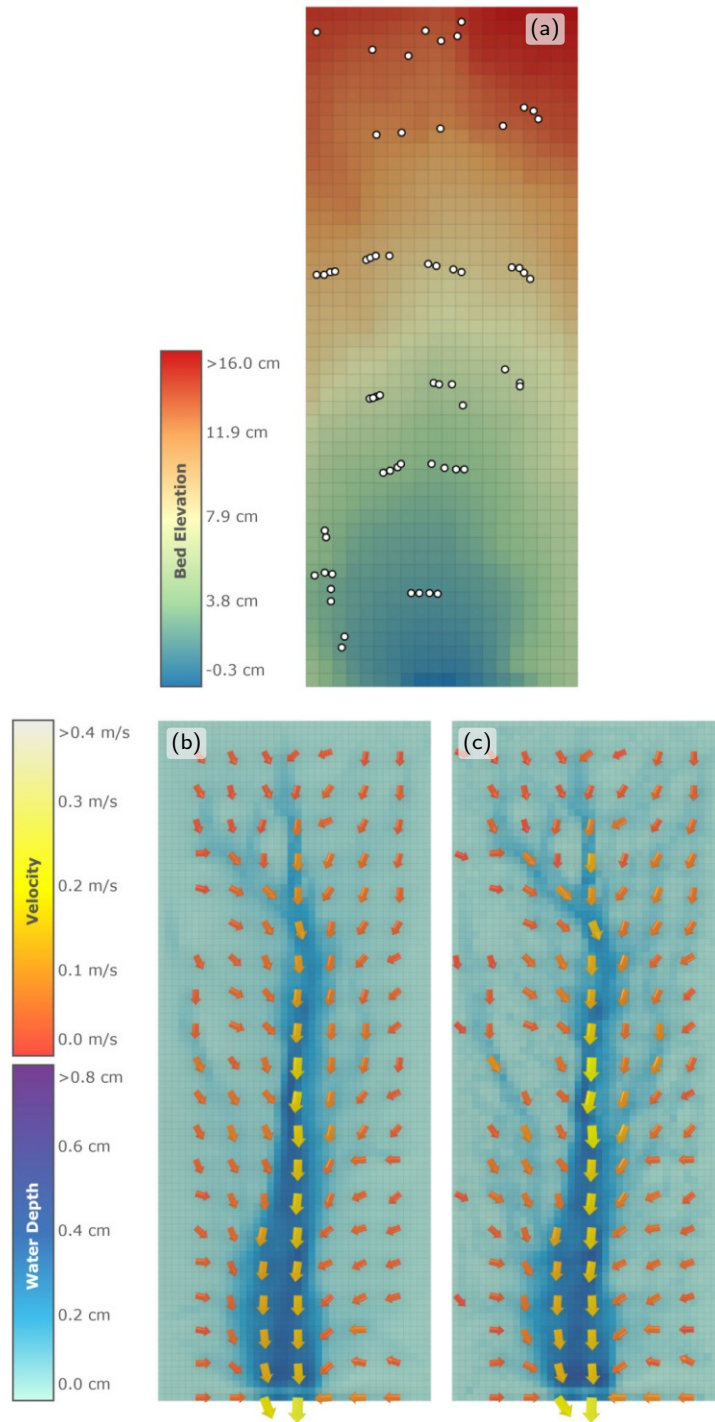
Fig. 4.2. Thiès experiment on a plot of 10×4 m^2. (a) Terrain with velocity measurement locations (white dots). (b) Simulated water depths after 1 h and velocities (colored arrows) of the first-order accurate CN scheme and a resolution of 0.1 m. (c) Simulated water depths after 1 h and velocities (colored arrows) of the second-order accurate BH scheme and a resolution of 0.1 m. The flow patterns of the first-order and second-order scheme are comparable for this fine resolution.
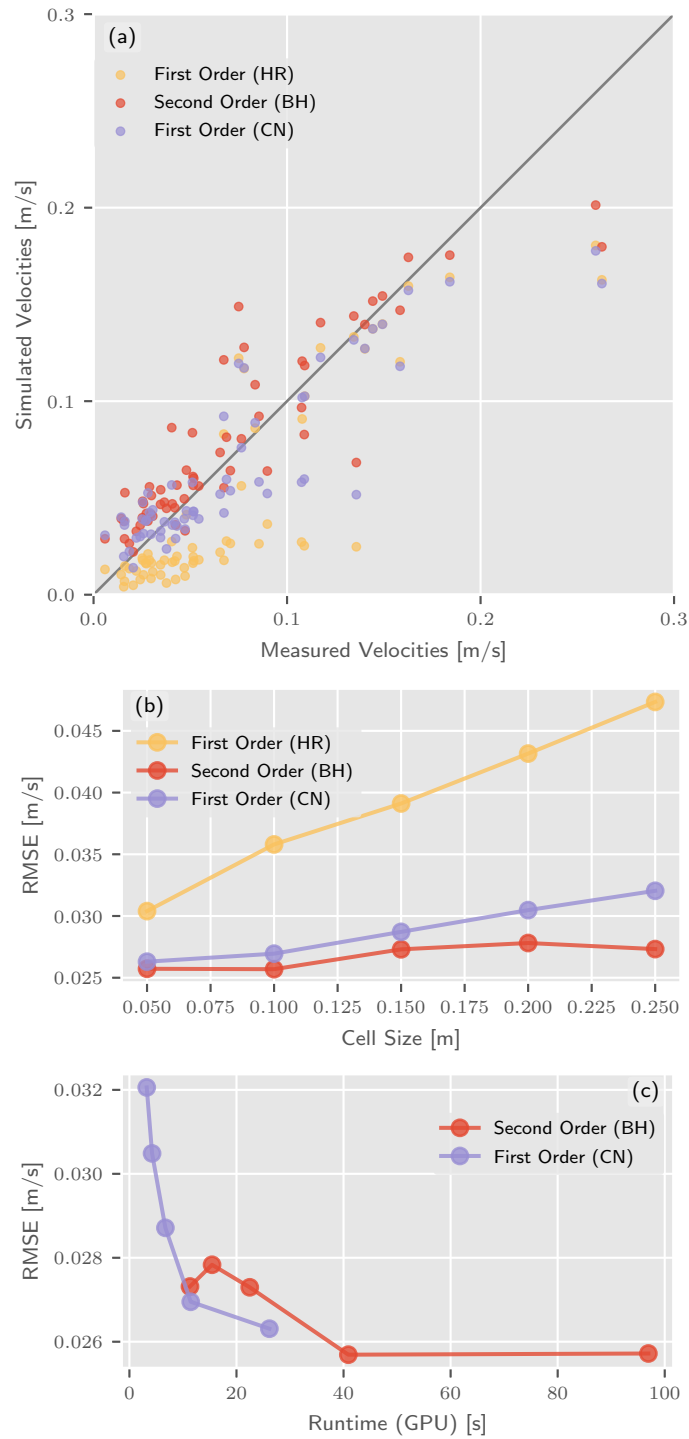
Fig. 4.3. Thiès. (a) Simulated velocities over measured velocities at steady-state conditions for a resolution of 0.1 m. The second-order scheme develops higher velocities than the first-order scheme. (b) Root mean square errors (RMSEs) over cell sizes. For the first-order scheme, the error decreases with resolution. For the second-order scheme the trend is not as pronounced. (c) RMSEs over GPU runtimes. For the same amount of computational time spent, the first-order CN scheme produces better results than the BH scheme.
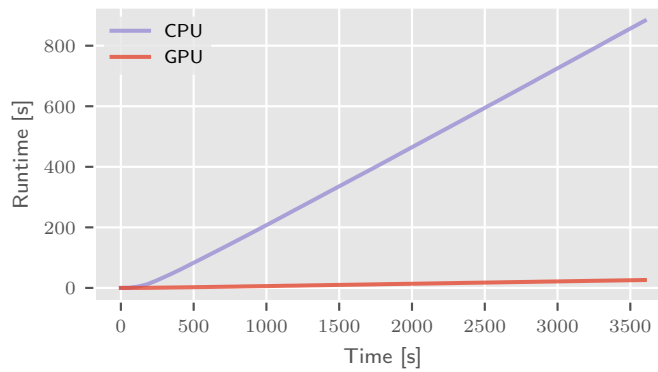
Fig. 4.4. Thiès. Runtimes for the sequential CPU and the GPU implementation of the first-order CN scheme for a resolution of 0.05 m. The smooth, nearly linear line indicates that wet-dry boundaries are treated properly and no high speeds develop.

In line with numerical theory, the RMSE decreases with grid refinement as shown in Fig. 4.3b. However, the RMSEs of the second-order scheme do not exhibit such a clear trend as the RMSEs of the first-order scheme. For the second-order scheme, the theoretical convergence order with regard to mesh refinement is limited, as the water surface is highly irregular in rainfall–runoff simulations. Typically, for smooth solution surfaces the second-order accurate scheme is expected to be more efficient when considering the accuracy versus runtime tradeoff (Horváth et al., 2020). However, wet–dry boundaries weaken this advantage already for analytical test cases, as for example in the parabolic basin test case (Thacker, 1981; Buttinger-Kreuzhuber et al., 2019). There, the theoretical convergence order of 2 for a second-order scheme degrades to 1.5 for the conserved variables, i. e. the water depths and the discharges.

When the corresponding runtimes of the CN and the BH schemes are compared in Fig. 4.3c, the first-order CN scheme produces better results for the same amount of computational time spent. In terms of the tradeoff between computational workload and accuracy, this suggests the use of finer grids together with first-order schemes for the surface flow in rainfall–runoff simulations. Summarizing, we conclude that fast first-order schemes, which properly resolve the source term, are sufficiently accurate for rainfall–runoff simulations.

The runtimes increase smoothly with simulation time (Fig. 4.4), which indicates that no high numerical speeds are encountered. Otherwise, they would slow down the simulation due to the CFL condition. This underlines the fact that the first-order CN scheme is robust, as no unphysical high velocity spots emerge. The parallel GPU implementation is more than 30 times faster than the sequential CPU implementation. In this case, due to the low number of cells in the domain, that is 16 000 cells for a resolution of 5 cm, the GPU can not fully exploit its parallel capabilities. The modest speedup in this small-scale experiment is therefore not representative of large real-world test cases.
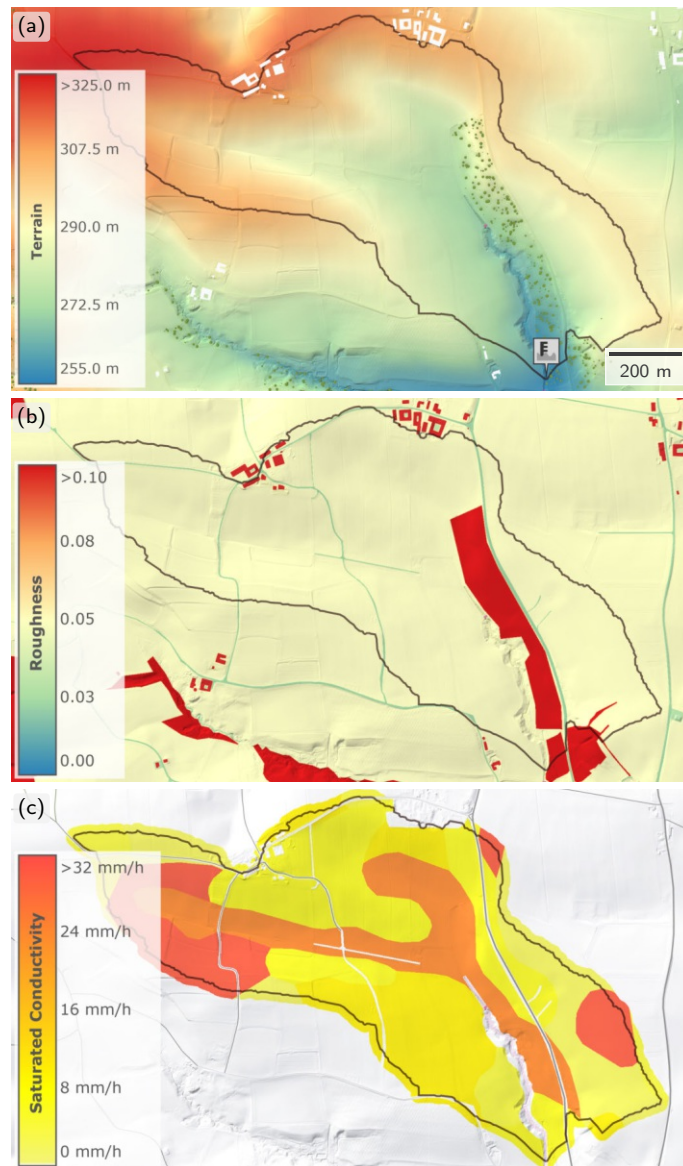
Fig. 4.5. HOAL Petzenkirchen. (a) Terrain elevation with the catchment outlet in the south east indicated by the label. (b) Spatial distribution of Manning's roughness coefficient $(s/m^{1/3})$ based on land use. (c) Spatial distribution of the saturated hydraulic conductivity based on soil types.

4.3.2 HOAL Petzenkirchen

This scenario analyzes a rainfall event in June 2013 in the Hydrological Open Air Laboratory (HOAL) catchment in Petzenkirchen, Lower Austria. The HOAL catchment is used to test hydrological hypotheses under natural conditions. The catchment is 0.66 km^2 in size and is mainly covered by arable land (87%) and grass-

84
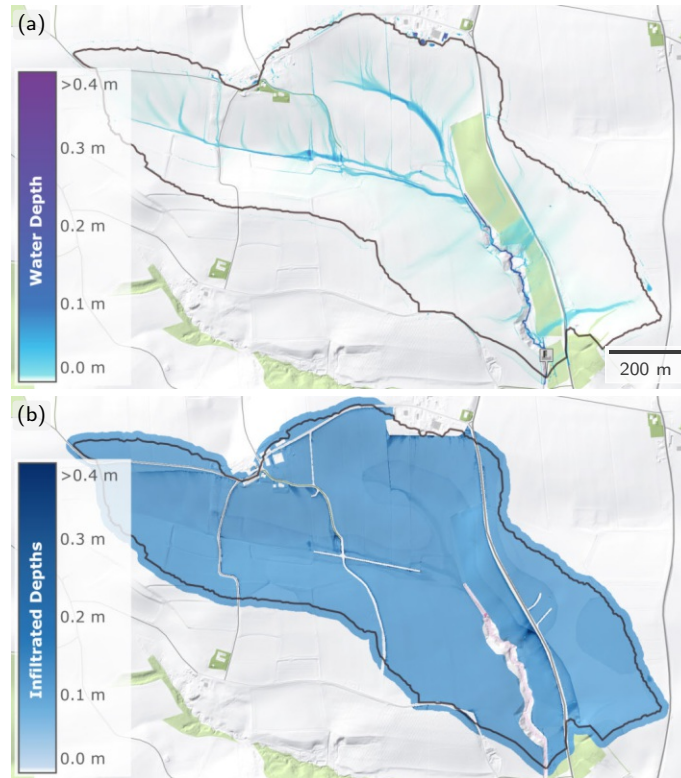
Fig. 4.6. HOAL Petzenkirchen. (a) Simulated water depths at the peak of the second rain block after 27.8 h. (b) Infiltrated depth F after 39 h at the end of the 1 m simulation.

land (10%) (Blöschl et al., 2016). A high resolution (0.5 m) DTM of 2012 was used. The topographic elevation of the catchment ranges from 255 to 325 m.a.s.l. (Fig. 4.5a). Manning's roughness coefficient is set to 0.1 s/m$^{1/3}$ for the riparian forest, to 0.05 s/m$^{1/3}$ for grassland and arable land, and to 0.03 s/m$^{1/3}$ everywhere else (Fig. 4.5b).

The top soil consists mostly (95%) of silt loam and silty clay loam. An analysis of the saturated hydraulic conductivity K_s with double-ring infiltrometers has been performed in 2018 for twelve plots (Picciafuoco et al., 2019). Three of the twelve plots are located on arable land, the other nine plots are located on small strips of grassland. The 131 measured values vary by two orders of magnitude, with a minimum of 1 mm/h and a maximum of 130 mm/h. The spatial distribution of the saturated conductivity follows soil types (Fig. 4.5c). The saturated conductivities range from 1 to 32 mm/h and are set according to literature values (Rawls et al., 1983; Carsel and Parrish, 1988; Smith et al., 2002) and measured values. Streets and the river bed are assumed to be impermeable. We specified an interception storage capacity of 5 mm for the riparian forests around the outflow (colored in light green in Fig. 4.6a) and of 2 mm for the arable land and grassland.
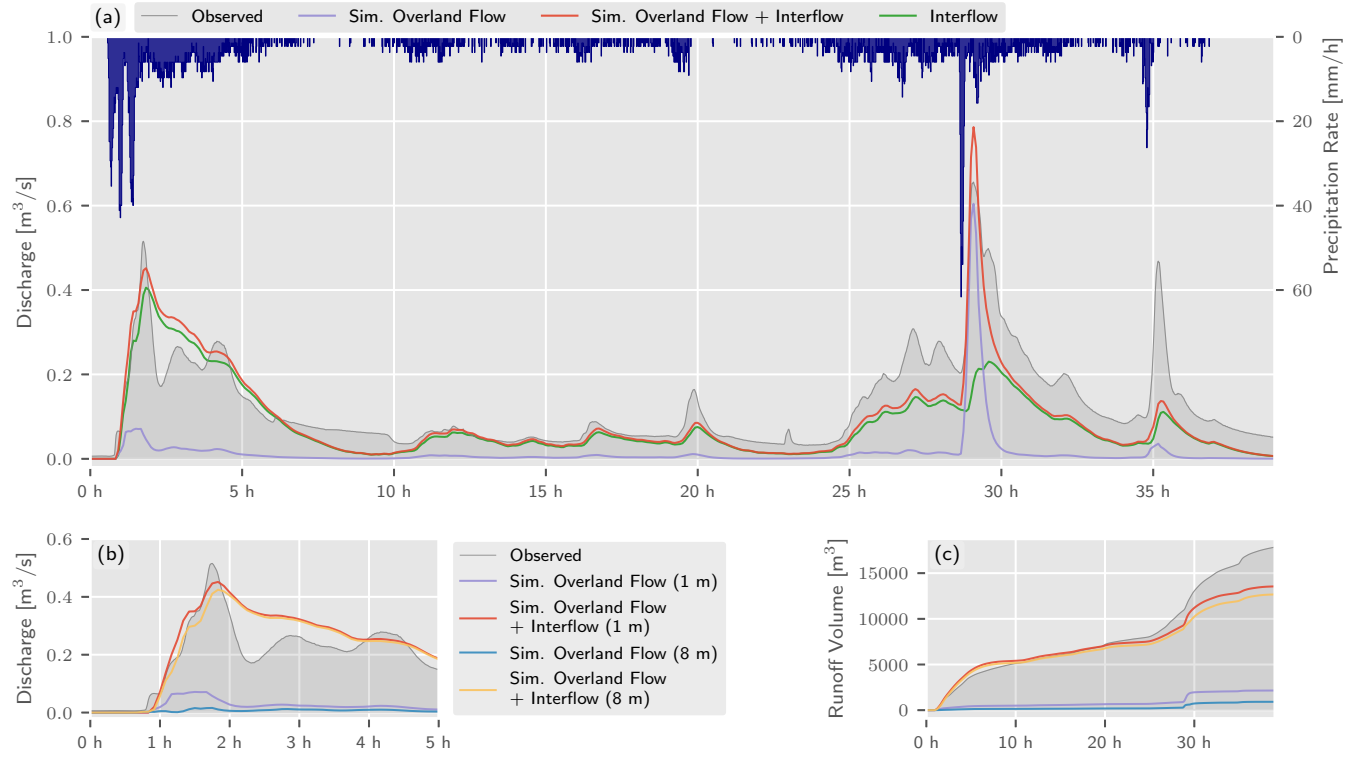
Fig. 4.7. Hydrological Open Air Laboratory (HOAL) Petzenkirchen. (a) Simulated catchment runoff discharges without interflow (violet) and with interflow (red) against observed outlet discharges (gray) for the simulation on the 1 m grid. The interflow component (green) accounts for return flow from previously infiltrated water. (b) Close-up of the first rain block for resolutions of 1 m and 8 m. The higher resolution causes a higher catchment runoff at the outlet. (c) Catchment runoff volumes.

Table 4.1. Hydrological Open Air Laboratory (HOAL) Petzenkirchen. The root mean square error (RMSE) and the Nash–Sutcliffe efficiency (NSE) of the discharges show good agreement between model and measured data for resolutions Δx below 4 m. The runoff volume error (RVE) shows that the measured catchment runoff volume exceeds the simulated runoff volume (SRV).

Δx [m]	Scheme	Runtime (GPU) [h]	RMSE [m³/s]	NSE	SRV [m³]	RVE
1.0	Second Order (BH)	0.3525	0.0627	0.6832	2080.2	-0.245
1.0	First Order (CN)	0.0806	0.0628	0.6819	2151.0	-0.241
2.0	Second Order (BH)	0.0702	0.0622	0.6877	1988.8	-0.246
2.0	First Order (CN)	0.0176	0.0626	0.6834	1997.3	-0.245
4.0	Second Order (BH)	0.0221	0.0624	0.6857	1667.5	-0.258
4.0	First Order (CN)	0.0080	0.0627	0.6823	1694.3	-0.256
8.0	Second Order (BH)	0.0106	0.0705	0.5986	943.8	-0.290
8.0	First Order (CN)	0.0054	0.0714	0.5881	917.2	-0.291

The investigated heavy rain event starts on June 23 at 21:00 and is simulated for 1.5 days. There are two distinct blocks of intense rainfall. The first occurs after 1 h, and the second after 28 h. The main flow paths of the surface runoff for the second rain block are clearly visible (Fig. 4.6a). Spatial patterns of the infiltrated depths (F) develop and correlate with available surface water and infiltration capacity (Fig. 4.6b). In this scenario, a linear reservoir model is used as a simple approximation of the interflow (Simons et al., 2013). The interflow discharge Q is given by the ordinary differential equation

$$\frac{d}{dt}Q(t) = \frac{1}{\kappa}(\alpha V(t - \tau) - Q(t)). \tag{4.19}$$

Here, a proportion $\alpha = 0.17$ of the infiltrated volume V, i.e. the sum of the infiltrated depths inside the catchment, is routed through the catchment with an average residence time $\kappa = 1$ h and a temporal offset $\tau = 15$ min. The interflow is directly added to the simulated overland flow discharges at the catchment outlet. The simulated overland flow discharges at the catchment outlet, the simulated catchment runoff discharges including the interflow, and the measured discharges are shown together with the rainfall in Fig. 4.7. Overall, the model is able to predict the discharges of the first rain block well. Improvements to the model's predictive capabilities are possible especially at the second day of the event. Towards the end of the event, smaller precipitation amounts cause higher measured catchment runoff discharges. In fact, the role of groundwater exchange flows seems to become more and more prominent and thus the interflow component has a significant influence. This is also visible in the catchment runoff volumes, where the model predictions for the first rain block are good, but deteriorate towards the end of the event (Fig. 4.7c).

A quantitative analysis of the discharges and volumes is performed in terms of the discharge RMSE and the Nash–Sutcliffe efficiency (NSE),

$$\text{NSE} = 1 - \frac{\sum_i (Q_s^i - Q_o^i)^2}{\sum_i (Q_o^i - \overline{Q_o})^2}, \tag{4.20}$$

Table 4.2. HOAL Petzenkirchen. Total runtimes of the sequential CPU implementation and the GPU implementation of the first-order CN scheme at the end of the simulated 39 h. For this small-scale case, the GPU is exploiting its computational power only at the highest resolutions, for lower resolutions it is not fully occupied and computational resources are left unused.

Resolution Δx [m]	Number of cells	Runtime [h]		Runtime per cell [ms]		
		CPU	GPU	CPU	GPU	Speedup
1.0	748095	146.14	0.081	703.3	0.39	1813.3
2.0	187717	15.64	0.018	300.0	0.34	888.9
4.0	47276	2.18	0.008	166.1	0.61	272.8
8.0	11997	0.42	0.005	126.3	1.62	78.0

where Q_s are the simulated discharges, and $\overline{Q_o}$ is the mean of the observed discharges. The NSE is a measure of fit, an efficiency of 1 represents a perfect fit. Finally, the relative runoff volume error (RVE),

$$\text{RVE} = \frac{V_s(T) - V_o(T)}{V_o(T)}, \tag{4.21}$$

measures the deviation of the simulated catchment runoff volume (including the interflow) V_s from the observed catchment runoff volume V_o at the end time T of the simulated event. Table 4.1 shows a slight beneficial effect of a higher resolution Δx on the NSE. The RMSE does not benefit as much from the higher resolution. This is due to its sensitiveness to extreme values. The surface runoff volume increases with the resolution: the simulation on the 8 m grid only results in approximately half of the total excess runoff volume of the simulation on the 1 m grid. For the 8 m simulation, runoff paths are blocked. Fragmentation of the runoff occurs, and the runoff takes the shape of isolated puddles. This effect is also observed in other studies (Noh et al., 2018). The peaks tend to get broader for higher resolutions. When comparing the second-order accurate BH scheme with the first-order accurate CN scheme, we see that the effect is less prominent. The second-order accurate BH scheme provides slightly better results than the first-order accurate CN scheme, however, at the cost of slower runtimes. The first-order scheme is between 2 to 4 times faster and is tending to become faster with an increasing number of cells. We expect the accuracy–workload tradeoff between first-order and second-order schemes to be in favor of second-order schemes, if the water surface becomes smoother due to the development of larger, connected streams.

Additional measured data that provides spatio-temporal information may shed more light on the involved processes and the quality of the model. A possible technique is hydrograph separation, where the water is attributed to pre-event and the different rain blocks in the event. Furthermore, spatially distributed observation data of the surface depths is crucial (Grayson and Blöschl, 2001; Bernet et al., 2018; Caviedes-Voullième et al., 2020). Such data could be used to determine the contribution of overland flow to total discharge and to assess the advantages of high

resolution rainfall–runoff modeling in more detail. Overall, the model provides a good fit as the NSE values are around 0.68 for resolutions below 4 m.

For the 1 m simulation, 0.75 million cells are wet at the peak of the second rain block, which corresponds to the simulated region of 0.75 km^2 (including a small buffer zone around the catchment). Regarding the runtimes of the sequential CPU and the parallel GPU implementation, speedups of three orders of magnitude are achieved (Table 4.2). The speedup increases with higher resolutions and higher workloads as the GPU is not fully utilized for a low resolution. For a fully occupied GPU, doubling the resolution causes a theoretical increase of the amount of work by eight times as the number of cells quadruples and due to the CFL condition twice the number of time steps are required. For the 1 m simulation, 90% of the computation time on the GPU is spent in the following routines: the reconstruction and flux computation (32%), the time integration and time step reduction (30%), and the computation and integration of the pending runoff (28%). In the latter routines, it is not the amount of floating-point operations but the memory transfers that prevent the GPU from achieving faster runtimes. On the CPU, the distribution is slightly different with 60%, 11%, and 9%, respectively, due to faster memory access rates.

One drawback of the GPU implementation is the comparably longer development time. Parallel CPU implementations are possible (Neal et al., 2010; Noh et al., 2018; Morales-Hernández et al., 2021), but even if the implementation achieves full parallelization speedups, over thousand CPU cores would be needed to match the computational advantage of the GPU. From an economic and ecological perspective the GPU simulation still performs better with regards to the power consumption than a parallel CPU simulation running on a supercomputer. The fast GPU simulation opens up new possibilities for this small catchment, such as uncertainty quantification and calibration tasks in a reasonable time span.

4.3.3 Urban flooding in Cologne

We study two urban scenarios in the city of Cologne, Germany. First, we present a dual-drainage model at the central part of the city, at the eastern bank of the Rhine river, to which we refer as Cologne Center-East. Second, we present a city-scale simulation encompassing the entire city of Cologne with an area of 23.73×27.14 km^2 without sewer coupling.

In the first scenario, the region simulated with the coupled model lies at the eastern bank of the Rhine river and covers an area of 5.41×9.86 km^2. The terrain model is obtained from light detection and ranging (LIDAR) data where solid urban features such as buildings or bridges were removed in a pre-processing step, so that the DTM represents a so-called bare earth DTM. The resolution of the DTM is 1 m with a typical vertical accuracy around a decimeter (Kraus, 2011; Dottori et al., 2013). The terrain is relatively flat, mostly ranging between 40 and 60 m.a.s.l. (Fig. 4.8a). The simulation domain exhibits modest average slopes of 0.3 m/km along the Rhine river from south to north, and of around 1 m/km from east to west.
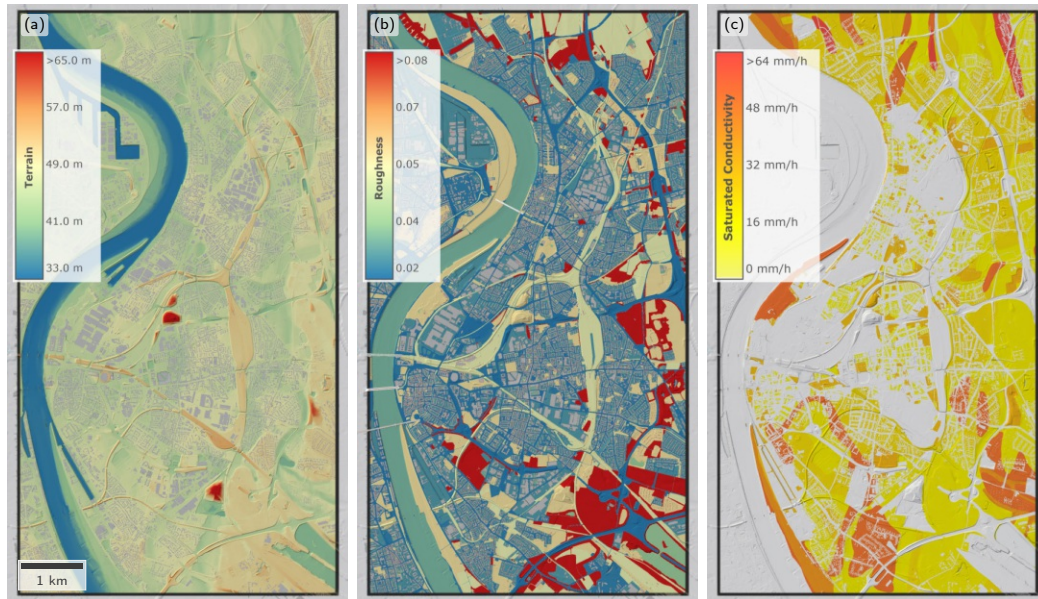
Fig. 4.8. Cologne Center-East coupled simulation. (a) The map of the terrain elevations shows only modest slopes across the simulation domain. The simulated region is heavily urbanized as indicated by the large amount of buildings, displayed in gray. (b) Manning's roughness coefficients ($s/m^{1/3}$) are derived from land use. (c) The spatial distribution of the saturated hydraulic conductivity is based on soil types. Streets and the river bed are set as impermeable zones.

Buildings and land use data are extracted from the official ALKIS data set of 2021 (Caffier et al., 2017). Buildings cover 13% of the area, they are impermeable for the surface flow and water from roofs is routed to sewer nodes in the coupled model, thus building cells remain dry during simulation. Roughness coefficients are mapped from the land use, a detailed overview of the spatial distribution is shown in Fig. 4.8b. The interception parameters are assumed to correlate with land use. Woods and gardens are assigned a storage capacity of 5 mm, public recreational areas and residential areas a capacity of 2 mm. Rivers, streets and parking lots are assumed to not retain rain, thus their storage capacity is set to zero. The infiltration parameters are derived from a soil map, compare the saturated hydraulic conductivity in Fig. 4.8c. Streets and squares as well as rivers and lakes are considered impermeable.

We preprocessed sewer data for SWMM for the eastern bank of the Rhine river, therefore, cells west of the river are excluded from the simulation. The active simulation region is thus restricted to 39 km^2. The sewer network consists of 6392 junction nodes and 7206 conduits linking them with a total length of 245 km. Moreover there are 16 pumps, 16 outfalls and 18 weirs in the simulation domain, which are included in the model. The sewer network and the invalidated region are shown in Fig. 4.9a in yellow and pink, respectively. Exchange between the sewer network and the surface is assumed to occur at the nodes with the parameters specified in Section 4.2.7.
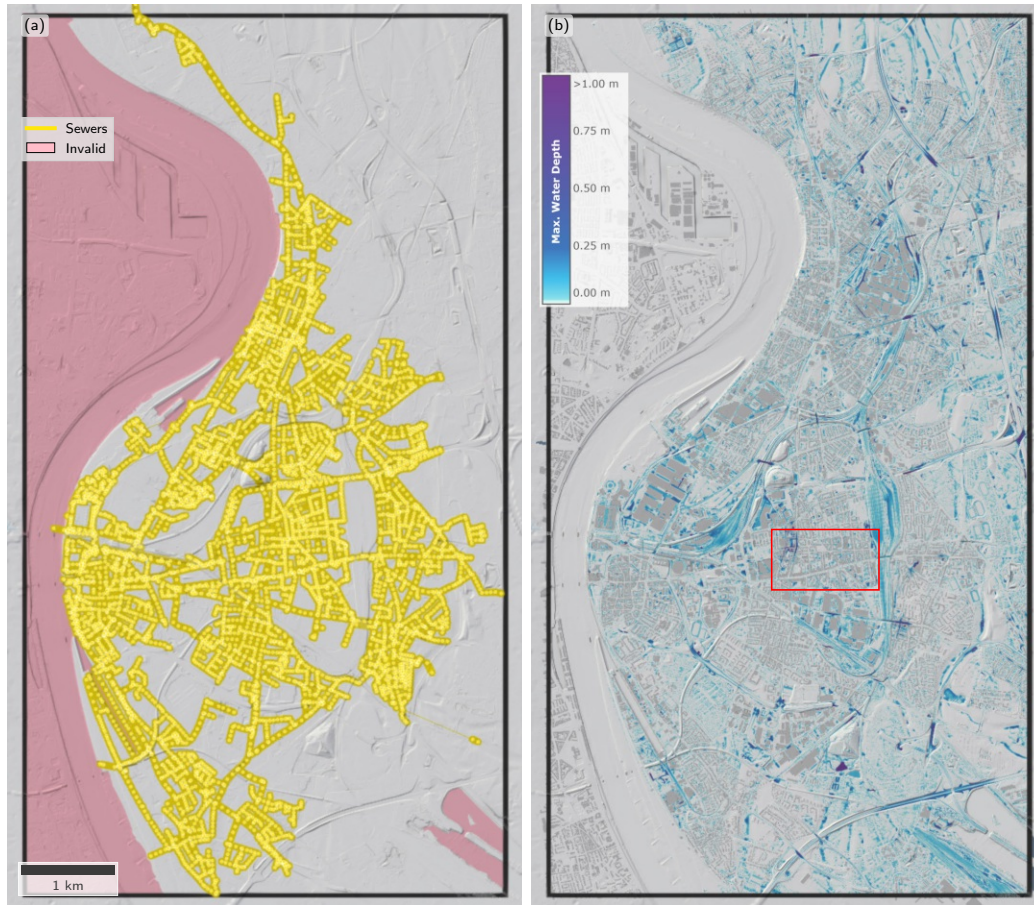
Fig. 4.9. Cologne Center-East coupled simulation. (a) The sewer network (yellow) and regions invalid for simulation (pink). (b) Maximum water depths of the 1 m simulation at the final simulation time $T = 2$ h. Fig. 4.10 focuses on the region marked with the red frame.

Each node has a maximum inflow capacity of 0.1 m^3/s. Rain that falls on buildings is directly routed to an assigned sewer junction node, if the roof water discharge exceeds the capacity, it spills over at the nodes.

We simulate a hypothetical uniform one-hour rainfall of 53 mm/h corresponding to approximately a 100-year event according to the KOSTRA 2010R data set (Junghänel et al., 2017). With a cell size of 1×1 m^2, the grid has nearly 40 million cells valid for simulation. We focus on the region marked with a red frame in Fig. 4.9b to illustrate the effects of the sewers, the resolution, and the order of accuracy of the surface flow scheme. The water depths are aggregated in time during the first-order 1 m simulation resulting in a maximum water depth for each cell at the end of the simulation (Fig. 4.9b).

The water depths of the coupled simulation for the specified region are aggregated in time resulting in maximum water depths (Fig. 4.10a). This heightfield serves as
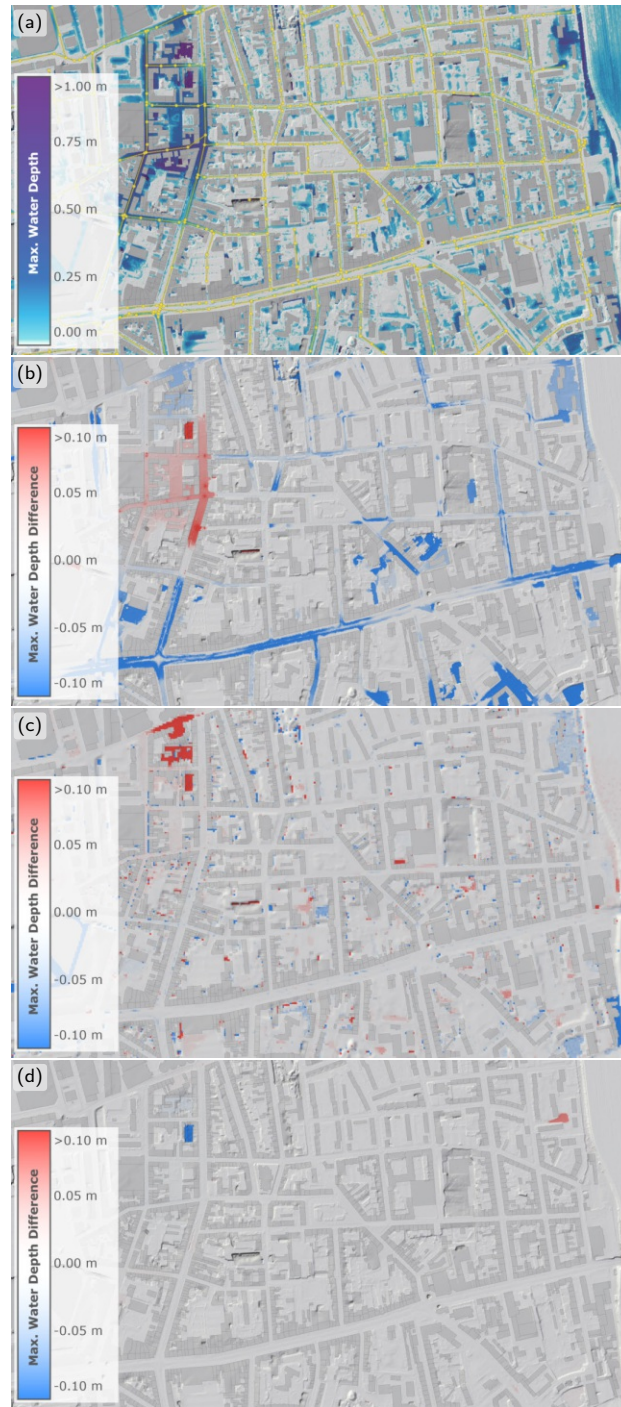
Fig. 4.10. Cologne Center-East detail. (a) Maximum water depths occurring during the coupled sewer–surface simulation with the first-order scheme and a resolution of 1 m. Difference heightfield of the maximum water depths between (b) the 1 m simulations with and without sewers, (c) the 1 m and the 4 m simulations, and (d) the first-order CN and the second-order BH accurate scheme. Regions with positive values (red) indicate higher maximum water depths in the coupled first-order simulation at 1 m shown in (a) than in the corresponding alternative simulations (b–d).

92

Table 4.3. Cologne Center-East coupled simulation. Runtimes of the sequential SWMM CPU solver and the GPU runoff simulation for the simulated timespan of 2 h over different resolutions Δx. For resolutions above 2 m, the sewer simulation on the CPU dominates the runtime of the coupled model.

Resolution Δx [m]	Number of cells	Runtime [h] Runoff (GPU)	Sewers (CPU)	Runoff/sewers runtime ratio
1.0	39023122	0.3657	0.2210	1.655
2.0	9755780	0.0612	0.2015	0.304
4.0	2438945	0.0164	0.2012	0.082

the reference for the difference heightfields, where positive values indicate higher maximum water depths in the reference simulation than in the corresponding alternative simulations. The differences between the simulation with sewer coupling and the one without are spatially restricted to the vicinity of the sewer network (Fig. 4.10b). For the simulation without sewer coupling, we assume that water falling onto roofs can be drained by the sewer network. In regions with positive values (red), the maximum water depths of the coupled simulation (Fig. 4.10a) are higher than the maximum water depths of the simulation without sewer coupling. In terms of the mean absolute error (MAE), the differences amount to 7.37 mm. The mean signed error (MSE), where the results of the runoff simulation without sewers are subtracted from those of the coupled simulation, amounts to -6.60 mm. This indicates that surface water levels do not rise as high in the coupled simulation due to sewer drainage. In fact, more water is drained from the streets than what is spilling onto the streets as excess roof water, which exceeds node inflow capacities. The sewer simulation also induces a water redistribution and causes minor floodings at a few streets due to sewer overflows. Overall, the sewer simulation drains around $250\,000$ m^3 of surface water.

In Fig. 4.10c, the difference field resulting from the subtraction of the maximum water depths computed by a 4 m simulation from the 1 m simulation is displayed. In regions with negative values (blue), the maximum water depths of the 4 m simulation are higher than the corresponding maximum water depths of the 1 m simulation. The difference between the maximum water depths of the 4 m and the 1 m grids are spatially concentrated at certain locations and appear mostly where the DTM shows strong variations at the scale of the employed cell size. For example, major differences occur in the vicinity of underpasses and garage entrances, or at the edge of elevated plateaus. At the edges of buildings, differences appear as boundary cells are rasterized as wall cells in one grid but not in the other. Overall, the MAE between the 4 m and the 1 m simulations is 8.12 mm. For the MAE computation the results of the 1 m grid are downsampled onto the 4 m grid.

In Fig. 4.10d, we compare the first-order accurate CN and the second-order accurate BH scheme. In general, the differences in the maximum water depths between the two surface flow discretizations are marginal. Noticeable deviations are concentrated on a few spots and occur where relatively high velocities up to 1 m/s

develop. This happens for example at sloped entrances to inner courtyards. In the entire simulation domain, the MAE between the two schemes is 1.2 mm and the MSE amounts to −0.1 mm. As we consider differences between the maximum water depths occurring during the event, a non-nil MSE does not indicate a volume error but rather indicates that the surface water travels a greater distance. In fact, the negative MSE reveals that maximum water depths are slightly higher in the second-order BH scheme. In this comparison, the errors are considerably smaller than in the previous comparisons. The relatively small differences have to be considered in light of the mild terrain slopes.

To thoroughly assess the quality of the predictive capabilities of the coupled model, further validation is required. The validation of coupled models on large-scale scenarios is challenging as in most cases the collected data is sparse. Possible strategies to tackle this problem are the collection of crowd-sourced data (Yu et al., 2016; Wang et al., 2018; Xing et al., 2018), imagery from unmanned aerial vehicle sensing (Perks et al., 2016) or insurance claims (Zischg et al., 2018).

A comparison of runtimes of the coupled simulator for resolutions of 1 m, 2 m, and 4 m, in Table 4.3 shows that the GPU-accelerated 2D surface flow simulation is faster than the sequential 1D CPU sewer simulation for low resolutions. This emphasizes once more the massive gain in computing power for the surface flow simulation due to the GPU-acceleration. Usually, solving the continuity and momentum equations for the sewer flow only requires around 0.1% of the total coupled simulation runtime for a sequential implementation (Noh et al., 2018). In the proposed implementation, as the simulations advance in parallel, the runtime per coupling time step is determined by the slower coupling component, which is either the GPU runoff simulation or the CPU sewer simulation. Thus, in order to improve the model performance further, effective parallelization strategies (Burger et al., 2014) of the sewer module are necessary.

For the derivation of pluvial flood hazard maps, we perform benchmark tests regarding large simulation domains with a size of 23.73×27.14 km^2 spanning the entire city of Cologne. We simulate uniform rainfall of 53 mm/h that lasts for 1 h. In order to account for surface flow routing after the rainfall ends, the total simulated duration is extended to 2 h. In this city-scale scenario shown in Fig. 4.11a, infiltration and interception are considered and are set up analogously to the previously studied smaller domain. The 1.5 m simulation grid has a total number of 220 million cells valid for simulation, of which 17 million cells are rasterized buildings. In this scenario, we do not explicitly simulate the sewer network of the entire city, but we assume that water falling onto roofs can be drained by the sewer network, therefore building cells are excluded from simulation. All other input parameters remain unchanged. In Fig. 4.11b, we display the maximum water depths that occur during the simulated event. The computational speed is faster than physical time, with a total runtime of 1.62 h for a total simulated duration of 2 h. The simulation uses up to 23.4 GB of memory on the NVIDIA Titan RTX GPU, close to its limit of 24 GB.

In previous studies, urban regions of 40 km^2 were modeled with an efficient hybrid
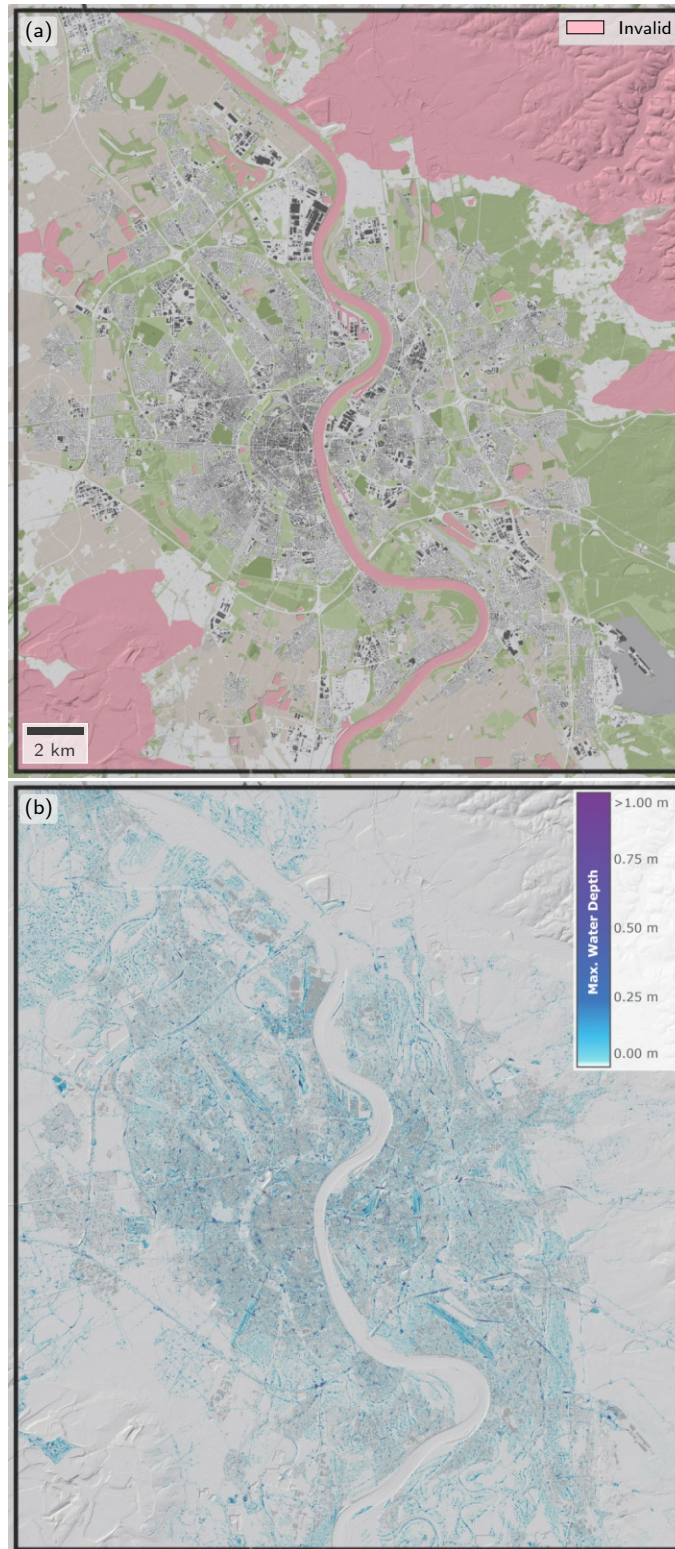
Fig. 4.11. Cologne runoff simulation. (a) Buildings (gray), land use and invalid cells (pink) for the simulated region covering the entire city. (b) Maximum water depth of the 1.5 m runoff simulation without sewer coupling after 2 h, i. e. at the end of the simulation.

parallelization strategy on an adaptive grid with a minimum cell size of 1 m (Noh et al., 2018). Their model uses runoff coefficients depending on land use instead of a dynamic infiltration model as in this work, but dynamic sewer coupling is also integrated. In Xing et al. (2018), the city of Fuzhou, China, is modeled with a resolution of 2 m and a constant drainage loss at streets neglecting bidirectional sewer interaction and water routing in sewers. The simulation involves 66 million cells and runs almost in realtime on a rack of 8 NVIDIA Tesla K80 GPUs. In contrast, the proposed computational model is efficient in terms of memory consumption and performance due to an elaborate implementation relying on single precision floating-point values. We are able to simulate over 200 million cells on a single GPU with 24 GB memory, processing 10 million cells per GB of GPU memory. This is advantageous against multi-GPU implementations as they require inter-GPU communication, which introduce an additional bottleneck and increase computation times (Morales-Hernández et al., 2021). In order to support larger simulation regions and higher spatial resolutions, an extension to multiple GPUs is possible.

4.4 Conclusion and perspectives

In this study, we present an integrated modeling framework for the simulation of rainfall–runoff processes and urban flash floods. The introduced modeling framework accounts for all the major processes needed for an accurate description of flash floods while still accomplishing very fast runtimes.

Infiltration is modeled with the Green–Ampt equations in a fully dynamic and spatially distributed way. An interception module accounts for initial rain abstractions due to vegetation. Instead of applying simple surface flow approximations, we discretize the full 2D shallow water equations (SWEs). In the context of rainfall–runoff simulations, the first-order accurate CN scheme (Chen and Noelle, 2017) was shown to be able to reproduce velocities and discharges accurately. In particular, using higher resolutions in the first-order scheme proved to be more beneficial than using the second-order accurate BH scheme (Buttinger-Kreuzhuber et al., 2019) when considering the tradeoff between accuracy and required computational work. The tradeoff observation is expected to hold as long as the water surface is irregular and not smooth, as it is often the case in rainfall–runoff simulations. We remark that an appropriate bed source term discretization of the surface flow is essential for providing correct velocity estimates. Moreover, in small catchments, resolutions around a meter are required to resolve river beds and the topography along the major flow paths.

For urban flash floods, the rainfall–runoff simulation is coupled with the sewer network simulation from the Storm Water Management Model (SWMM). An effective approach for the bidirectional coupling of the sewer simulation to the surface runoff simulation is developed, where the two simulators advance in parallel in each coupling timestep. The runoff simulation is validated in the Thiès irrigation experiment and in the HOAL Petzenkirchen catchment, where a NSE value of 0.68 was

achieved for a simulation lasting for 36 hours and containing two heavy rain blocks separated by a day. Regarding the validation of the coupled model, we point out that more detailed spatial observations are needed in order to assess the model's predictive performance in a more exhaustive way.

We demonstrate the benefits of using graphics processing units (GPUs) as computational devices to speed up the rainfall–runoff simulations. The GPU-accelerated model enables high-resolution simulations for entire cities with simulation domains involving up to 225 million cells on a single GPU with 24 GB of memory. In other words, we enable simulation of regions up to 220 km^2 with a resolution of 1 m in realtime. This removes the need for inconvenient domain decompositions and multiple localized, small-scale simulations. Speed-ups of up to three orders of magnitude are achieved for simulated regions with around 10 million cells, if compared against a serial CPU implementation. The speedup increases with the number of cells, thus large simulation regions profit even more from GPU acceleration.

In summary, the main contributions of the paper are:

1) a spatially distributed GPU-accelerated rainfall–runoff model combining the Green–Ampt infiltration model and the full SWEs,

2) an efficient bidirectional coupling between the surface flow simulation and the sewer network simulation using an interleaved time-stepping approach,

3) fast coupled simulations for entire cities at resolutions around a meter,

4) validation and performance tests on rural and urban scenarios,

5) the finding that the workload–accuracy tradeoff favors a higher resolution over discretization order for runoff simulation in small or urban catchments.

The efficiency of the approach opens up new possibilities regarding ensemble simulations and high-resolution environmental modeling. The coupling of the surface flow with the spatially distributed infiltration and interception component allows the direct inclusion of green infrastructure by varying the parameters accordingly. Detailed results help raise public awareness for flash floods by providing straightforward impact analysis at the scale of individual buildings and enable the analysis of efforts to mitigate the effects of climate change in rural and urban settings.

5 Summary and overall conclusions

This thesis addresses challenges related to fluvial and pluvial flood hazard mapping at large scales. Particularly pressing issues are identified and subsequently examined. They include the robustness and accuracy of the numerical scheme used for solving the shallow water equations (SWEs) in complex terrain, the efficiency of large-scale flood inundation modeling and the integration of multiple model components in flash flood simulations.

In Chapter 2, the first-order shallow water scheme developed by Chen and Noelle (2017) is extended to second-order accuracy in regions where the solution is smooth. Difficulties related to discontinuities in the bed source term are overcome by a specialized "adaptive" reconstruction. The scheme's second-order accuracy is verified in numerical test cases, as is the scheme's ability to preserve still-water and lake-at-rest steady states. Compared to the popular hydrostatic reconstruction scheme of Audusse et al. (2004), the proposed discretization of the SWEs offers an economical approximation of the bed source term resulting in faster runtimes. In the case of shallow downhill flows over steps, it provides more accurate results. The numerical model is validated against measured data from laboratory experiments and historic floods.

In Chapter 3, the presented scheme is applied to delineate inundated flood areas for Austria (83,880 km^2) at a resolution of 2 m. A river network of 33,880 km is simulated in a distributed setup of 182 rectangular tiles. A computationally efficient approach to maintain flood probabilities along the river network is proposed by adjusting the discharges via additional source terms in the SWEs. The proposed regional approach is an appealing alternative to ensemble simulations which require numerous evaluations. Given a tiling of the region of interest, the flood hazard model is integrated in the automation framework Visdom, which automatically sets up the boundary conditions, executes the hydraulic simulation and carries out post-processing tasks without the need for human intervention. For a 100-year flood, 3532 km^2 or 883 million wet pixels of inundated areas are simulated in less than a month on 10 NVIDIA TITAN RTX graphics processing units (GPUs). The inundated areas compare well with detailed local flood hazard maps, i. e. critical success index (CSI) scores range from 0.61 to 0.74 across Austria's regions. For all of Austria, a CSI score of 0.7 and a hit rate of 83 % is achieved. Differences occur in particular due to the proposed regional approach of adjusting flood quantiles and due to small deviations in the digital terrain model (DTM).

In Chapter 4, the first-order accurate CN scheme by Chen and Noelle (2017) and the proposed second-order accurate scheme are extended by model components required for a comprehensive description of processes relevant for flash floods. Interception and infiltration are modeled in a spatially distributed way, allowing for different interception and infiltration parameters in every cell of the computa-

tional domain. For urban scenarios, the popular Storm Water Management Model (SWMM) is coupled with the rainfall–runoff simulator in an efficient interleaved way. The integrated modeling framework is validated on a laboratory and a rural test case. Model runtimes of the GPU-accelerated version are more than 1000 times faster than the corresponding sequential version running on a single central processing unit (CPU). Considering the tradeoff between workload and accuracy, results indicate that the usage of the first-order scheme in combination with higher resolution should be favored over the usage of the second-order scheme at comparably lower resolutions. The integrated model is applied to the city of Cologne, demonstrating the model's capability to simulate cities of up to 200 km^2 at a resolution of 1 m.

Not long ago, resolutions of 25 to 100 m were considered characteristic for regional flood hazard assessments (Moel et al., 2015). This thesis demonstrates the feasibility of large-scale flood hazard mapping at a resolution of a few meters. The detailed simulations allow for the estimation of damage for individual buildings and the analysis of local small-scale alterations, e. g. of green infrastructure or protective measures, at large scales.

Regarding the validation of large-scale models, observed inundation data is typically sparse in space and/or time. Thus a comprehensive validation, in particular of the integrated flash flood modeling framework, requires further data. Nevertheless, for scenarios where validation data is available, good agreement between reference data and simulated data is found, thus underlining the predictive performance of the developed methods.

Still, limitations exist in the proposed methods. The presented second-order scheme is able to preserve quiescent steady states. However, an extension to more general steady states, for example moving-water steady states accounting for friction, could improve the model's accuracy even further. For certain Riemann problems, the full wave structure is not replicated, thus future work could focus on this issue.

To enable the simulation of even larger domains, multi-GPU implementations could extend current limitations by distributing the work onto multiple GPUs in a tightly coupled way where state variables are exchanged in every time step. Another possible direction of future work are machine learning methods. Neural networks that respect the given laws of physics described by nonlinear partial differential equations, so-called physics-informed neural networks, provide computationally efficient surrogate models (Raissi et al., 2019).

In this thesis, flood hazards are assessed only for a single driver, e. g. either from extreme river flows or rainfall. A combined evaluation of pluvial and fluvial flood hazard model was done for the conterminous United States in Bates et al. (2021). By combining the presented methods an extension to account for multiple drivers seems like a comparably small step and a natural progression of this work.

Unfortunately, a thorough analysis of the uncertainty in the model cascade used for the delineation of the inundated areas was beyond the scope of this work but could be addressed in a future study. Traditionally, methods to quantify uncertainties rely on Monte Carlo or ensemble simulations. They are also used to quantify

consequences of uncertain predictions of future conditions including, for example, increasing streamflow discharges or precipitation rates under a changing climate. Due to the efficient computational techniques, the evaluation of ensemble simulations is possible within reasonable time spans.

Overall, this thesis contributes to the recent research on flood hazard mapping at large scales in several ways. First, a novel second-order accurate scheme is proposed to accurately simulate water flow (Chapter 2). Second, a new approach to maintain flood probabilities across a large river network and an innovative automation framework for inundation modeling are proposed (Chapter 3). Third, a comprehensive assessment of heavy rain events is supported by the coupling of overland flow simulation, of spatially distributed infiltration and interception processes, of culverts and the sewer system (Chapter 4). Fourth, the combination of the proposed second-order accurate scheme and the extensive use of GPUs enables the simulation of large domains, e. g. entire cities or regions, at high resolutions with short model runtimes (Chapter 3–4). The innovative methods developed in this thesis pave the way for a new standard in flood hazard mapping with regards to accuracy and computational efficiency.

Acknowledgments

This work was supported by the VRVis Zentrum für Virtual Reality und Visualisierung and by the Austrian Science Funds (FWF) as part of the Vienna Doctoral Programme on Water Resource Systems (DK W1219-N28). VRVis is funded by BMK, BMDW, Styria, SFG, Tyrol and Vienna Business Agency in the scope of COMET – Competence Centers for Excellent Technologies (879730), which is managed by FFG.

We thank the Stadtentwässerungsbetriebe Köln (`www.steb-koeln.de`) and the Bundesamt für Wasserwirtschaft – Institut für Kulturtechnik und Bodenwasserhaushalt for providing us with data necessary for setting up the Cologne and Petzenkirchen scenarios in Chapter 4, respectively.

References

Acuña, M. A. and T. Aoki (2009). Real-time tsunami simulation on multi-node GPU cluster. *ACM/IEEE conference on supercomputing.*

Alfieri, L., P. Burek, L. Feyen, and G. Forzieri (2015). Global warming increases the frequency of river floods in Europe. *Hydrology and Earth System Sciences* 19.5, pp. 2247–2260. DOI: 10.5194/hess-19-2247-2015.

Alfieri, L., B. Bisselink, F. Dottori, G. Naumann, A. de Roo, P. Salamon, K. Wyser, and L. Feyen (2017). Global projections of river flood risk in a warmer world. *Earth's Future* 5.2, pp. 171–182. DOI: 10.1002/2016EF000485.

Alfieri, L., P. Salamon, A. Bianchi, J. C. Neal, P. D. Bates, and L. Feyen (2014). Advances in pan-European flood hazard mapping. *Hydrological Processes* 28.13, pp. 4067–4077. DOI: 10.1002/hyp.9947.

Almeida, G. de, P. Bates, and H. Ozdemir (2016). Modelling urban floods at sub-metre resolution: challenges or opportunities for flood risk management? *Journal of Flood Risk Management* 11, S855–S865. DOI: 10.1111/jfr3.12276.

An, H. and S. Yu (2012). Well-balanced shallow water flow simulation on quadtree cut cell grids. *Advances in Water Resources* 39, pp. 60–70.

Annis, A., F. Nardi, E. Volpi, and A. Fiori (2020). Quantifying the relative impact of hydrological and hydraulic modelling parameterizations on uncertainty of in-undation maps. *Hydrological Sciences Journal* 65.4, pp. 507–523. DOI: 10.1080/02626667.2019.1709640.

Aricò, C. and C. Nasello (2018). Comparative Analyses between the Zero-Inertia and Fully Dynamic Models of the Shallow Water Equations for Unsteady Overland Flow Propagation. *Water* 10.1. DOI: 10.3390/w10010044.

Aronica, G., P. D. Bates, and M. S. Horritt (2002). Assessing the uncertainty in distributed model predictions using observed binary pattern information within GLUE. *Hydrological Processes* 16.10, pp. 2001–2016. DOI: 10.1002/hyp.398.

Asunción, M. de la, M. J. Castro, E. D. Fernández-Nieto, J. M. Mantas, S. O. Acosta, and J. M. González-Vida (2013). Efficient GPU implementation of a two waves TVD-WAF method for the two-dimensional one layer shallow water system on structured meshes. *Computers & Fluids* 80, pp. 441–452.

Audusse, E., F. Bouchut, M.-O. Bristeau, R. Klein, and B. Perthame (2004). A Fast and Stable Well-Balanced Scheme with Hydrostatic Reconstruction for Shallow Water Flows. *SIAM Journal on Scientific Computing* 25.6, pp. 2050–2065.

Audusse, E., F. Bouchut, M.-O. Bristeau, and J. Sainte-Marie (2016). Kinetic entropy inequality and hydrostatic reconstruction scheme for the Saint-Venant system. *Math. Comp.* 85.302, pp. 2815–2837. DOI: 10.1090/mcom/3099.

Audusse, E. and M.-O. Bristeau (2005). A Well-Balanced Positivity Preserving "Second-order" Scheme for Shallow Water Flows on Unstructured Meshes. *Journal of Computational Physics* 206.1, pp. 311–333. DOI: 10.1016/j.jcp.2004.12.016.

References

Aureli, F., F. Prost, R. Vacondio, S. Dazzi, and A. Ferrari (2020). A GPU-Accelerated Shallow-Water Scheme for Surface Runoff Simulations. *Water* 12.3, p. 637. DOI: `10.3390/w12030637`.

Bates, P. D., N. Quinn, C. Sampson, A. Smith, O. Wing, J. Sosa, J. Savage, G. Olcese, J. Neal, G. Schumann, L. Giustarini, G. Coxon, J. R. Porter, M. F. Amodeo, Z. Chu, S. Lewis-Gruss, N. B. Freeman, T. Houser, M. Delgado, A. Hamidi, I. Bolliger, K. E. McCusker, K. Emanuel, C. M. Ferreira, A. Khalid, I. D. Haigh, A. Couasnon, R. E. Kopp, S. Hsiang, and W. F. Krajewski (2021). Combined Modeling of US Fluvial, Pluvial, and Coastal Flood Hazard Under Current and Future Climates. *Water Resources Research* 57.2. e2020WR028673 2020WR028673, e2020WR028673. DOI: `10.1029/2020WR028673`.

Bender, J., T. Wahl, A. Müller, and J. Jensen (2016). A multivariate design framework for river confluences. *Hydrological Sciences Journal* 61.3, pp. 471–482. DOI: `10.1080/02626667.2015.1052816`.

Berland, A., S. A. Shiflett, W. D. Shuster, A. S. Garmestani, H. C. Goddard, D. L. Herrmann, and M. E. Hopton (2017). The role of trees in urban stormwater management. *Landscape and Urban Planning* 162, pp. 167–177. DOI: `10.1016/j.landurbplan.2017.02.017`.

Bernet, D. B., A. P. Zischg, V. Prasuhn, and R. Weingartner (2018). Modeling the extent of surface water floods in rural areas: Lessons learned from the application of various uncalibrated models. *Environmental Modelling & Software* 109, pp. 134–151. DOI: `10.1016/j.envsoft.2018.08.005`.

Berthon, C. and F. Foucher (2012). Efficient well-balanced hydrostatic upwind schemes for shallow-water equations. *Journal of Computational Physics* 231.15, pp. 4993–5015. DOI: `10.1016/j.jcp.2012.02.031`.

Blöschl, G., A. P. Blaschke, M. Broer, C. Bucher, G. Carr, X. Chen, A. Eder, M. Exner-Kittridge, A. Farnleitner, A. Flores-Orozco, P. Haas, P. Hogan, A. K. Amiri, M. Oismüller, J. Parajka, R. Silasari, P. Stadler, P. Strauss, M. Vreugdenhil, W. Wagner, and M. Zessner (2016). The Hydrological Open Air Laboratory (HOAL) in Petzenkirchen: a hypothesis-driven observatory. *Hydrology and Earth System Sciences* 20.1, pp. 227–255. DOI: `10.5194/hess-20-227-2016`.

Blöschl, G., L. Gaál, J. Hall, A. Kiss, J. Komma, T. Nester, J. Parajka, R. A. Perdigão, L. Plavcová, M. Rogger, et al. (2015). Increasing river floods: fiction or reality? *Wiley Interdisciplinary Reviews: Water* 2.4, pp. 329–344. DOI: `10.1002/wat2.1079`.

Blöschl, G., J. Hall, A. Viglione, R. A. P. Perdigão, J. Parajka, B. Merz, D. Lun, B. Arheimer, G. T. Aronica, A. Bilibashi, M. Boháč, O. Bonacci, M. Borga, I. Čanjevac, A. Castellarin, G. B. Chirico, P. Claps, N. Frolova, D. Ganora, L. Gorbachova, A. Gül, J. Hannaford, S. Harrigan, M. Kireeva, A. Kiss, T. R. Kjeldsen, S. Kohnová, J. J. Koskela, O. Ledvinka, N. Macdonald, M. Mavrova-Guirguinova, L. Mediero, R. Merz, P. Molnar, A. Montanari, C. Murphy, M. Osuch, V. Ovcharuk, I. Radevski, J. L. Salinas, E. Sauquet, M. Šraj, J. Szolgay, E. Volpi, D. Wilson, K. Zaimi, and N. Živković (2019). Changing climate both increases and decreases

European river floods. *Nature* 573.7772, pp. 108–111. DOI: 10.1038/s41586-019-1495-6.

Blöschl, G., T. Nester, J. Komma, J. Parajka, and R. A. Perdigão (2013). The June 2013 flood in the Upper Danube Basin, and Comparisons with the 2002, 1954 and 1899 floods. *Hydrology and Earth System Sciences* 17.12, pp. 5197–5212. DOI: 10.5194/hess-17-5197-2013.

Bollermann, A., G. Chen, A. Kurganov, and S. Noelle (2013). A Well-Balanced Reconstruction of Wet/Dry Fronts for the Shallow Water Equations. *J. Sci. Comput.* 56.2, pp. 267–290. DOI: 10.1007/s10915-012-9677-5.

Bouchut, F. (2004). *Nonlinear Stability of Finite Volume Methods for Hyperbolic Conservation Laws: And Well-Balanced Schemes for Sources*. Springer Science & Business Media.

Bouchut, F. (2007). Chapter 4: Efficient Numerical Finite Volume Schemes for Shallow Water Models. *Nonlinear Dynamics of Rotating Shallow Water: Methods and Advances*. Ed. by V. Zeitlin. Vol. 2. Edited Series on Advances in Nonlinear Science and Complexity. Elsevier Science, pp. 189–256. DOI: 10.1016/S1574-6909(06)02004-1.

Brodtkorb, A. R., T. R. Hagen, K.-A. Lie, and J. R. Natvig (2010). Simulation and visualization of the Saint-Venant system using GPUs. *Computing and Visualization in Science* 13.7, pp. 341–353.

Brodtkorb, A. R., M. L. Sætra, and M. S. Altinakar (2012). Efficient Shallow Water Simulations on GPUs: Implementation, Visualization, Verification, and Validation. *Computers & Fluids* 55.0, pp. 1–12. DOI: 10.1016/j.compfluid.2011.10.012.

Buffard, T. and S. Clain (2010). Monoslope and multislope MUSCL methods for unstructured meshes. *Journal of Computational Physics* 229.10, pp. 3745–3776. DOI: 10.1016/j.jcp.2010.01.026.

Bures, L., R. Roub, P. Sychova, K. Gdulova, and J. Doubalova (2019). Comparison of bathymetric data sources used in hydraulic modelling of floods. *Journal of Flood Risk Management* 12.S1, e12495. DOI: 10.1111/jfr3.12495.

Burger, G., R. Sitzenfrei, M. Kleidorfer, and W. Rauch (2014). Parallel flow routing in SWMM 5. *Environmental Modelling & Software* 53, pp. 27–34. DOI: 10.1016/j.envsoft.2013.11.002.

Buttinger-Kreuzhuber, A., Z. Horváth, S. Noelle, G. Blöschl, and J. Waser (2019). A fast second-order shallow water scheme on two-dimensional structured grids over abrupt topography. *Advances in Water Resources* 127, pp. 89–108. DOI: 10.1016/j.advwatres.2019.03.010.

Caffier, A., C. Elsner, C. Rath, F. Robens, J. Seidel, and K. Will (2017). Offene Geobasisdaten für NRW. *Z. Geodäsie Geoinf. Landmanag.(Zfv)* 142, pp. 133–145.

Carsel, R. F. and R. S. Parrish (1988). Developing joint probability distributions of soil water retention characteristics. *Water Resources Research* 24.5, pp. 755–769. DOI: 10.1029/wr024i005p00755.

Castro, M. J., A. F. Ferreiro, J. García-Rodríguez, J. González-Vida, J. Macías, C. Parés, and M. E. Vázquez-Cendón (2005). The numerical treatment of wet/dry

References

fronts in shallow flows: application to one-layer and two-layer systems. *Mathematical and Computer Modelling* 42.3, pp. 419–439. DOI: 10.1016/j.mcm.2004.01.016.

Castro, M. J., P. G. LeFloch, M. L. Muñoz-Ruiz, and C. Parés (2008). Why Many Theories of Shock Waves Are Necessary: Convergence Error in Formally Path-Consistent Schemes. *Journal of Computational Physics* 227.17, pp. 8107–8129. DOI: 10.1016/j.jcp.2008.05.012.

Castro, M. J., A. Pardo Milanés, and C. Parés (2007). Well-Balanced Numerical Schemes Based on a Generalized Hydrostatic Reconstruction Technique. *Mathematical Models and Methods in Applied Sciences* 17.12, pp. 2055–2113. DOI: 10.1142/S021820250700256X.

Caviedes-Voullième, D., J. Fernández-Pato, and C. Hinz (2020). Performance assessment of 2D Zero-Inertia and Shallow Water models for simulating rainfall-runoff processes. *Journal of Hydrology* 584, p. 124663. DOI: 10.1016/j.jhydrol.2020.124663.

Chen, A. S., J. Leandro, and S. Djordjević (2016). Modelling sewer discharge via displacement of manhole covers during flood events using 1D/2D SIPSON/P-DWave dual drainage simulations. *Urban Water Journal* 13.8, pp. 830–840. DOI: 10.1080/1573062X.2015.1041991.

Chen, G. and S. Noelle (2017). A New Hydrostatic Reconstruction Scheme Based on Subcell Reconstructions. *SIAM Journal on Numerical Analysis* 55.2, pp. 758–784.

Chen, Y., W. Moufouma-Okia, V. Masson-Delmotte, P. Zhai, and A. Pirani (2018). Recent Progress and Emerging Topics on Weather and Climate Extremes Since the Fifth Assessment Report of the Intergovernmental Panel on Climate Change. *Annual Review of Environment and Resources* 43.1, pp. 35–59. DOI: 10.1146/annurev-environ-102017-030052.

Chinnayya, A., A.-Y. Leroux, and N. Seguin (2004). A well-balanced numerical scheme for the approximation of the shallow-water equations with topography: the resonance phenomenon. *International Journal on Finite Volumes* 1, pp. 1–33.

Chow, V. T., D. Maidment, and L. Mays (1988). *Applied Hydrology*. McGraw-Hill series in water resources and environmental engineering. McGraw-Hill.

Chow, V. T. (1959). *Open-channel hydraulics*. McGraw-Hill civil engineering series. McGraw-Hill.

Clain, S., C. Reis, R. Costa, J. Figueiredo, M. A. Baptista, and J. M. Miranda (2016). Second-order finite volume with hydrostatic reconstruction for tsunami simulation. *Journal of Advances in Modeling Earth Systems* 8.4, pp. 1691–1713. DOI: 10.1002/2015MS000603.

Cornwall, W. (2021). Europe's deadly floods leave scientists stunned. *Science* 373.6553, pp. 372–373. DOI: 10.1126/science.373.6553.372.

Corradini, C., F. Melone, and R. E. Smith (2000). Modeling local infiltration for a two-layered soil under complex rainfall patterns. *Journal of Hydrology* 237.1, pp. 58–73. DOI: 10.1016/S0022-1694(00)00298-5.

Costabile, P., C. Costanzo, G. De Lorenzo, and F. Macchione (2020). Is local flood hazard assessment in urban areas significantly influenced by the physical complexity of the hydrodynamic inundation model? *Journal of Hydrology* 580, p. 124231. DOI: 10.1016/j.jhydrol.2019.124231.

Costabile, P., C. Costanzo, and F. Macchione (2013). A storm event watershed model for surface runoff based on 2D fully dynamic wave equations. *Hydrological Processes* 27.4, pp. 554–569. DOI: 10.1002/hyp.9237.

Costabile, P., C. Costanzo, and F. Macchione (2017). Performances and limitations of the diffusive approximation of the 2-d shallow water equations for flood simulation in urban and rural areas. *Applied Numerical Mathematics* 116. New Trends in Numerical Analysis: Theory, Methods, Algorithms and Applications (NETNA 2015), pp. 141–156. DOI: 10.1016/j.apnum.2016.07.003.

Courant, R., K. Friedrichs, and H. Lewy (1967). On the partial difference equations of mathematical physics. *IBM journal of Research and Development* 11.2, pp. 215–234.

Cozzolino, L., L. Cimorelli, R. Della Morte, G. Pugliano, V. Piscopo, and D. Pianese (2019). Flood propagation modeling with the Local Inertia Approximation: Theoretical and numerical analysis of its physical limitations. *Advances in Water Resources* 133, p. 103422. DOI: 10.1016/j.advwatres.2019.103422.

Dal Maso, G., P. G. LeFloch, and F. Murat (1995). Definition and weak stability of nonconservative products. *J. Math. Pures Appl. (9)* 74.6, pp. 483–548.

Delestre, O., S. Cordier, F. Darboux, and F. James (2012). A Limitation of the Hydrostatic Reconstruction Technique for Shallow Water Equations. *Comptes Rendus Mathematique* 350.13-14, pp. 677–681. DOI: 10.1016/j.crma.2012.08.004.

Delestre, O., F. Darboux, F. James, C. Lucas, C. Laguerre, and S. Cordier (2017). FullSWOF: Full Shallow-Water equations for Overland Flow. *The Journal of Open Source Software* 2.20, p. 448. DOI: 10.21105/joss.00448.

Delestre, O., C. Lucas, P.-A. Ksinant, F. Darboux, C. Laguerre, T.-N. Vo, F. James, S. Cordier, et al. (2013). SWASHES: a compilation of shallow water analytic solutions for hydraulic and environmental studies. *International Journal for Numerical Methods in Fluids* 72.3, pp. 269–300. DOI: 10.1002/fld.3741.

Delis, A. I., I. K. Nikolos, and M. Kazolea (2011). Performance and Comparison of Cell-Centered and Node-Centered Unstructured Finite Volume Discretizations for Shallow Water Free Surface Flows. *Archives of Computational Methods in Engineering* 18.1, pp. 57–118. DOI: 10.1007/s11831-011-9057-6.

Djordjević, S., D. Prodanović, Č. Maksimović, M. Ivetić, and D. Savić (2005). SIPSON – Simulation of Interaction between Pipe flow and Surface Overland flow in Networks. *Water Science and Technology* 52.5, pp. 275–283. DOI: 10.2166/wst.2005.0143.

Dottori, F., G. Di Baldassarre, and E. Todini (2013). Detailed data is welcome, but with a pinch of salt: Accuracy, precision, and uncertainty in flood inundation modeling. *Water Resources Research* 49.9, pp. 6079–6085. DOI: 10.1002/wrcr.20406.

References

Dottori, F., P. Salamon, A. Bianchi, L. Alfieri, F. A. Hirpa, and L. Feyen (2016). Development and evaluation of a framework for global flood hazard mapping. *Advances in Water Resources* 94, pp. 87–102. DOI: `10.1016/j.advwatres.2016.05.002`.

Duran, A., Q. Liang, and F. Marche (2013). On the well-balanced numerical discretization of shallow water equations on unstructured meshes. *Journal of Computational Physics* 235, pp. 565–586.

Dutykh, D., R. Poncet, and F. Dias (2011). The VOLNA Code for the Numerical Modeling of Tsunami Waves: Generation, Propagation and Inundation. *European Journal of Mechanics-B/Fluids* 30.6, pp. 598–615.

Echeverribar, I., M. Morales-Hernández, P. Brufau, and P. García-Navarro (2019). 2D numerical simulation of unsteady flows for large scale floods prediction in real time. *Advances in Water Resources* 134, p. 103444. DOI: `10.1016/j.advwatres.2019.103444`.

Ernst, J., B. J. Dewals, S. Detrembleur, P. Archambeau, S. Erpicum, and M. Pirotton (2010). Micro-scale flood risk analysis based on detailed 2D hydraulic modelling and high resolution geographic data. *Natural Hazards* 55.2, pp. 181–209. DOI: `10.1007/s11069-010-9520-y`.

European Commission (2007). Directive 2007/60/EC of the European Parliament and of the Council of 23 October 2007 on the assessment and management of flood risks. *Official Journal of the European Union* L288, pp. 27–34.

Falter, D., N. Dung, S. Vorogushyn, K. Schröter, Y. Hundecha, H. Kreibich, H. Apel, F. Theisselmann, and B. Merz (2016). Continuous, large-scale simulation model for flood risk assessments: proof-of-concept. *Journal of Flood Risk Management* 9.1, pp. 3–21. DOI: `10.1111/jfr3.12105`.

Falter, D., K. Schröter, N. V. Dung, S. Vorogushyn, H. Kreibich, Y. Hundecha, H. Apel, and B. Merz (2015). Spatially coherent flood risk assessment based on long-term continuous simulation with a coupled model chain. *Journal of Hydrology* 524, pp. 182–193. DOI: `https://doi.org/10.1016/j.jhydrol.2015.02.021`.

Fernández-Pato, J., D. Caviedes-Voullième, and P. García-Navarro (2016). Rainfall/runoff simulation with 2D full shallow water equations: Sensitivity analysis and calibration of infiltration parameters. *Journal of Hydrology* 536, pp. 496–513. DOI: `10.1016/j.jhydrol.2016.03.021`.

Fernández-Pato, J. and P. García-Navarro (2018). Development of a New Simulation Tool Coupling a 2D Finite Volume Overland Flow Model and a Drainage Network Model. *Geosciences* 8.8, p. 288. DOI: `10.3390/geosciences8080288`.

Fewtrell, T. J., A. Duncan, C. C. Sampson, J. C. Neal, and P. D. Bates (2011). Benchmarking urban flood models of varying complexity and scale using high resolution terrestrial LiDAR data. *Physics and Chemistry of the Earth, Parts A/B/C* 36.7. Recent Advances in Mapping and Modelling Flood Processes in Lowland Areas, pp. 281–291. DOI: `10.1016/j.pce.2010.12.011`.

Fiedler, F. R. and J. A. Ramirez (2000). A numerical method for simulating discontinuous shallow flow over an infiltrating surface. *International Journal for*

Numerical Methods in Fluids 32.2, pp. 219–239. DOI: `10.1002/(SICI)1097-0363(20000130)32:2<219::AID-FLD936>3.0.CO;2-J`.

Fleischmann, A., R. Paiva, and W. Collischonn (2019). Can regional to continental river hydrodynamic models be locally relevant? A cross-scale comparison. *Journal of Hydrology X* 3, p. 100027. DOI: `10.1016/j.hydroa.2019.100027`.

Frazao, S. S., F. Alcrudo, and N. Goutal (1999). Dam-break test cases summary. *Proceedings of the Fourth CADAM Meeting*, pp. 9–25.

Fry, T. J. and R. M. Maxwell (2018). Using a Distributed Hydrologic Model to Improve the Green Infrastructure Parameterization Used in a Lumped Model. *Water* 10.12. DOI: `10.3390/w10121756`.

Gallardo, J. M., C. Parés, and M. J. Castro (2007). On a Well-Balanced High-Order Finite Volume Scheme for Shallow Water Equations with Topography and Dry Areas. *Journal of Computational Physics* 227.1, pp. 574–601.

Gallegos, H. A., J. E. Schubert, and B. F. Sanders (2009). Two-dimensional, high-resolution modeling of urban dam-break flooding: A case study of Baldwin Hills, California. *Advances in Water Resources* 32.8, pp. 1323–1335. DOI: `10.1016/j.advwatres.2009.05.008`.

George, D. L. (2011). Adaptive Finite Volume Methods with Well-Balanced Riemann Solvers for Modeling Floods in Rugged Terrain: Application to the Malpasset Dam-Break Flood (France, 1959). *International Journal for Numerical Methods in Fluids* 66.8, pp. 1000–1018.

Gerbeau, J.-F. and B. Perthame (2001). Derivation of viscous Saint-Venant system for laminar shallow water; Numerical validation. *Discrete & Continuous Dynamical Systems - B* 1.1, pp. 89–102.

Ghidaglia, J.-M. and F. Pascal (2005). The Normal Flux Method at the Boundary for Multidimensional Finite Volume Approximations in CFD. *European Journal of Mechanics-B/Fluids* 24.1, pp. 1–17. DOI: `10.1016/j.euromechflu.2004.05.003`.

Gottlieb, S., C.-W. Shu, and E. Tadmor (2001). Strong stability-preserving high-order time discretization methods. *SIAM Rev.* 43.1, pp. 89–112. DOI: `10.1137/S003614450036757X`.

Goutal, N., M.-H. Le, and P. Ung (2017). A Godunov-Type Scheme for Shallow Water Equations Dedicated to Simulations of Overland Flows on Stepped Slopes. *Finite Volumes for Complex Applications VIII - Hyperbolic, Elliptic and Parabolic Problems: FVCA 8, Lille, France, June 2017*. Ed. by C. Cancès and P. Omnes. Cham: Springer International Publishing. Chap. Hyperbolic Problems, pp. 275–283. DOI: `10.1007/978-3-319-57394-6_30`.

Goutal, N. and F. Maurel (1997). Note Technique EDF, HE-43/97/016/B. *Proceedings of the 2nd Workshop on Dam-Break Simulation*. Department Laboratoire National d'Hydraulique, Groupe Hydraulique Fluviale.

Gowdish, L. and R. Muñoz-Carpena (2009). An Improved Green–Ampt Infiltration and Redistribution Method for Uneven Multistorm Series. *Vadose Zone Journal* 8.2, pp. 470–479. DOI: `10.2136/vzj2008.0049`.

Grayson, R. and G. Blöschl (2001). *Spatial patterns in catchment hydrology: observations and modelling*. CUP Archive.

References

Guse, B., B. Merz, L. Wietzke, S. Ullrich, A. Viglione, and S. Vorogushyn (2020). The role of flood wave superposition in the severity of large floods. *Hydrology and Earth System Sciences* 24.4, pp. 1633–1648. DOI: 10.5194/hess-24-1633-2020.

Han, E. and G. Warnecke (2014). Exact Riemann solutions to shallow water equations. *Quart. Appl. Math.* 72.3, pp. 407–453. DOI: 10.1090/S0033-569X-2014-01353-3.

Harten, A. and J. M. Hyman (1983). Self adjusting grid methods for one-dimensional hyperbolic conservation laws. *Journal of computational Physics* 50.2, pp. 235–269.

Harten, A., P. D. Lax, and B. van Leer (1983). On Upstream Differencing and Godunov-Type Schemes for Hyperbolic Conservation Laws. *SIAM Review* 25.1, pp. 35–61. DOI: 10.1137/1025002.

Hervouet, J.-M. and A. Petitjean (1999). Malpasset dam-break revisited with two-dimensional computations. *Journal of Hydraulic Research* 37.6, pp. 777–788.

Hoch, J. M., D. Eilander, H. Ikeuchi, F. Baart, and H. C. Winsemius (2019). Evaluating the impact of model complexity on flood wave propagation and inundation extent with a hydrologic–hydrodynamic model coupling framework. *Natural Hazards and Earth System Sciences* 19.8, pp. 1723–1735. DOI: 10.5194/nhess-19-1723-2019.

Holdahl, R., H. Holden, and K.-A. Lie (1999). Unconditionally stable splitting methods for the shallow water equations. *BIT Numerical Mathematics* 39.3, pp. 451–472.

Horváth, Z., A. Buttinger-Kreuzhuber, A. Konev, D. Cornel, J. Komma, G. Blöschl, S. Noelle, and J. Waser (2020). Comparison of Fast Shallow-Water Schemes on Real-World Floods. *Journal of Hydraulic Engineering* 146.1, p. 05019005. DOI: 10.1061/(ASCE)HY.1943-7900.0001657.

Horváth, Z., R. A. Perdigão, J. Waser, D. Cornel, A. Konev, and G. Blöschl (2016). Kepler Shuffle for Real-World Flood Simulations on GPUs. *The International Journal of High Performance Computing Applications* 30.4, pp. 379–395. DOI: 10.1177/1094342016630800.

Horváth, Z., J. Waser, R. A. Perdigão, A. Konev, and G. Blöschl (2015). A Two-Dimensional Numerical Scheme of Dry/Wet Fronts for the Saint-Venant System of Shallow Water Equations. *International Journal for Numerical Methods in Fluids* 77.3, pp. 159–182.

Hou, J., Q. Liang, F. Simons, and R. Hinkelmann (2013a). A 2D well-balanced shallow flow model for unstructured grids with novel slope source term treatment. *Advances in Water Resources* 52, pp. 107–131.

Hou, J., Q. Liang, H. Zhang, and R. Hinkelmann (2014). Multislope MUSCL method applied to solve shallow water equations. *Computers & Mathematics with Applications* 68.12, pp. 2012–2027.

Hou, J., F. Simons, M. Mahgoub, and R. Hinkelmann (2013b). A robust well-balanced model on unstructured grids for shallow water flows with wetting and drying over complex topography. *Computer Methods in Applied Mechanics and Engineering* 257, pp. 126–149. DOI: 10.1016/j.cma.2013.01.015.

Ingram, D. M., D. M. Causon, and C. G. Mingham (2003). Developments in Cartesian cut cell methods. *Mathematics and Computers in Simulation* 61.3, pp. 561–572.

Jongman, B. (2018). Effective adaptation to rising flood risk. *Nature Communications* 9.1. DOI: 10.1038/s41467-018-04396-1.

Jonkman, S. N. (2005). Global Perspectives on Loss of Human Life Caused by Floods. *Natural Hazards* 34.2, pp. 151–175. DOI: 10.1007/s11069-004-8891-3.

Junghänel, T., H. Ertel, and T. Deutschländer (2017). *Bericht zur Revision von KOSTRA-DWD-2010*. Tech. rep. Last visited on 2021-04-29. Deutscher Wetterdienst, Abteilung Hydrometeorologie. URL: https://www.dwd.de/DE/leistungen/kostra_dwd_rasterwerte/kostra_dwd_rasterwerte.html.

Kaiser, M., M. Borga, and M. Disse (2020). Occurrence and Characteristics of Flash Floods in Bavaria (Germany). *Climate Change, Hazards and Adaptation Options: Handling the Impacts of a Changing Climate*. Ed. by W. Leal Filho, G. J. Nagy, M. Borga, P. D. Chávez Muñoz, and A. Magnuszewski. Cham: Springer International Publishing. Chap. Occurrence and Characteristics of Flash Floods in Bavaria (Germany), pp. 293–310. DOI: 10.1007/978-3-030-37425-9_16.

Kesserwani, G. and Q. Liang (2012). Dynamically adaptive grid based discontinuous Galerkin shallow water model. *Advances in Water Resources* 37, pp. 23–39.

Klöckner, A., T. Warburton, J. Bridge, and J. S. Hesthaven (2009). Nodal discontinuous Galerkin methods on graphics processors. *Journal of Computational Physics* 228.21, pp. 7863–7882.

Kraus, K. (2011). *Photogrammetry*. De Gruyter. DOI: doi:10.1515/9783110892871.

Kuffour, B. N. O., N. B. Engdahl, C. S. Woodward, L. E. Condon, S. Kollet, and R. M. Maxwell (2020). Simulating coupled surface–subsurface flows with ParFlow v3.5.0: capabilities, applications, and ongoing development of an open-source, massively parallel, integrated hydrologic model. *Geoscientific Model Development* 13.3, pp. 1373–1397. DOI: 10.5194/gmd-13-1373-2020.

Kvočka, D., R. A. Falconer, and M. Bray (2015). Appropriate model use for predicting elevations and inundation extent for extreme flood events. *Natural Hazards* 79.3, pp. 1791–1808. DOI: 10.1007/s11069-015-1926-0.

Lacasta, A., M. Morales-Hernández, J. Murillo, and P. García-Navarro (2015). GPU Implementation of the 2D Shallow Water Equations for the Simulation of Rainfall/Runoff Events. *Environmental Earth Sciences* 74.11, pp. 7295–7305.

Le, P. V., P. Kumar, A. J. Valocchi, and H.-V. Dang (2015). GPU-based high-performance computing for integrated surface–sub-surface flow modeling. *Environmental Modelling & Software* 73, pp. 1–13. DOI: 10.1016/j.envsoft.2015.07.015.

Leandro, J., A. Schumann, and A. Pfister (2016). A step towards considering the spatial heterogeneity of urban key features in urban hydrology flood modelling. *Journal of Hydrology* 535, pp. 356–365. DOI: 10.1016/j.jhydrol.2016.01.060.

Leandro, J. and R. Martins (2016). A methodology for linking 2D overland flow models with the sewer network model SWMM 5.1 based on dynamic link libraries.

Water Science and Technology 73.12, pp. 3017–3026. DOI: 10.2166/wst.2016.171.

LeFloch, P. G. and M. D. Thanh (2007). The Riemann Problem for the Shallow Water Equations with Discontinuous Topography. *Commun. Math. Sci.* 5.4, pp. 865–885.

LeFloch, P. G. and M. D. Thanh (2011). A Godunov-Type Method for the Shallow Water Equations with Discontinuous Topography in the Resonant Regime. *Journal of Computational Physics* 230.20, pp. 7631–7660. DOI: 10.1016/j.jcp.2011.06.017.

LeVeque, R. J. (1992). *Numerical Methods for Conservation Laws*. Second. Lectures in Mathematics ETH Zürich. Birkhäuser verlag, Basel, pp. x+214. DOI: 10.1007/978-3-0348-8629-1.

Li, Q., Q. Liang, and X. Xia (2020). A novel 1D-2D coupled model for hydrodynamic simulation of flows in drainage networks. *Advances in Water Resources* 137, p. 103519. DOI: 10.1016/j.advwatres.2020.103519.

Liang, Q. and F. Marche (2009). Numerical resolution of well-balanced shallow water equations with complex source terms. *Advances in Water Resources* 32, pp. 873–884. DOI: 10.1016/j.advwatres.2009.02.010.

Maxwell, R. M. (2013). A terrain-following grid transform and preconditioner for parallel, large-scale, integrated hydrologic modeling. *Advances in Water Resources* 53, pp. 109–117. DOI: 10.1016/j.advwatres.2012.10.001.

Merz, R., G. Blöschl, and G. Humer (2008). National flood discharge mapping in Austria. *Natural Hazards* 46.1, pp. 53–72. DOI: 10.1007/s11069-007-9181-7.

Merz, R., U. Piock-Ellena, G. Blöschl, and D. Gutknecht (1999). Seasonality of flood processes in Austria. *Hydrological Extremes: Understanding, Predicting, Mitigating. Wallingford, UK*. IAHS Press, pp. 273–278.

Moel, H. de, B. Jongman, H. Kreibich, B. Merz, E. Penning-Rowsell, and P. J. Ward (2015). Flood risk assessments at different spatial scales. *Mitigation and Adaptation Strategies for Global Change* 20.6, pp. 865–890. DOI: 10.1007/s11027-015-9654-z.

Mohammadzadeh-Habili, J. and M. Heidarpour (2015). Application of the Green–Ampt model for infiltration into layered soils. *Journal of Hydrology* 527, pp. 824–832. DOI: 10.1016/j.jhydrol.2015.05.052.

Morales de Luna, T., M. J. Castro Díaz, and C. Parés (2013). Reliability of First Order Numerical Schemes for Solving Shallow Water System over Abrupt Topography. *Applied Mathematics and Computation* 219.17, pp. 9012–9032.

Morales-Hernández, M., P. García-Navarro, J. Burguete, and P. Brufau (2013). A Conservative Strategy to Couple 1D and 2D Models for Shallow Water Flow Simulation. *Computers & Fluids* 81, pp. 26–44.

Morales-Hernández, M., M. B. Sharif, A. Kalyanapu, S. Ghafoor, T. Dullo, S. Gangrade, S.-C. Kao, M. Norman, and K. Evans (2021). TRITON: A Multi-GPU open source 2D hydrodynamic flood model. *Environmental Modelling & Software* 141, p. 105034. DOI: 10.1016/j.envsoft.2021.105034.

Mügler, C., O. Planchon, J. Patin, S. Weill, N. Silvera, P. Richard, and E. Mouche (2011). Comparison of roughness models to simulate overland flow and tracer transport experiments under simulated rainfall at plot scale. *Journal of Hydrology* 402.1, pp. 25–40. DOI: `10.1016/j.jhydrol.2011.02.032`.

Murillo, J. and P. García-Navarro (2010). Weak solutions for partial differential equations with source terms: Application to the shallow water equations. *Journal of Computational Physics* 229.11, pp. 4327–4368. DOI: `10.1016/j.jcp.2010.02.016`.

Murillo, J. and P. García-Navarro (2012). Augmented versions of the HLL and HLLC Riemann solvers including source terms in one and two dimensions for shallow flow applications. *Journal of Computational Physics* 231.20, pp. 6861–6906. DOI: `10.1016/j.jcp.2012.06.031`.

Murillo, J. and P. García-Navarro (2013). Energy balance numerical schemes for shallow water equations with discontinuous topography. *Journal of Computational Physics* 236, pp. 119–142. DOI: `10.1016/j.jcp.2012.11.003`.

Murillo, J. and A. Navas-Montilla (2016). A comprehensive explanation and exercise of the source terms in hyperbolic systems using Roe type solutions. Application to the 1D-2D shallow water equations. *Advances in Water Resources* 98, pp. 70–96. DOI: `10.1016/j.advwatres.2016.10.019`.

Neal, J. C., T. J. Fewtrell, P. D. Bates, and N. G. Wright (2010). A comparison of three parallelisation methods for 2D flood inundation models. *Environmental Modelling & Software* 25.4, pp. 398–411. DOI: `10.1016/j.envsoft.2009.11.007`.

Neal, J. C., G. Schumann, and P. D. Bates (2012). A subgrid channel model for simulating river hydraulics and floodplain inundation over large and data sparse areas. *Water Resources Research* 48.11. DOI: `10.1029/2012WR012514`.

Nessyahu, H. and E. Tadmor (1990). Non-oscillatory central differencing for hyperbolic conservation laws. *Journal of computational physics* 87.2, pp. 408–463.

Noelle, S., N. Pankratz, G. Puppo, and J. R. Natvig (2006). Well-balanced finite volume schemes of arbitrary order of accuracy for shallow water flows. *Journal of Computational Physics* 213.2, pp. 474–499.

Noh, S. J., J.-H. Lee, S. Lee, K. Kawaike, and D.-J. Seo (2018). Hyper-resolution 1D-2D urban flood modelling using LiDAR data and hybrid parallelization. *Environmental Modelling & Software* 103, pp. 131–145. DOI: `10.1016/j.envsoft.2018.02.008`.

Özgen, I., J. Zhao, D. Liang, and R. Hinkelmann (2016). Urban flood modeling using shallow water equations with depth-dependent anisotropic porosity. *Journal of Hydrology* 541, pp. 1165–1184. DOI: `https://doi.org/10.1016/j.jhydrol.2016.08.025`.

Pankratz, N., J. R. Natvig, B. Gjevik, and S. Noelle (2007). High-Order Well-Balanced Finite-Volume Schemes for Barotropic Flows: Development and Numerical Comparisons. *Ocean Modelling* 18.1, pp. 53–79. DOI: `10.1016/j.ocemod.2007.03.005`.

References

Parés, C. and E. Pimentel (2019). The Riemann Problem for the Shallow Water Equations with Discontinuous Topography: the Wet-Dry Case. *Journal of Computational Physics* 378, pp. 344–365. DOI: `10.1016/j.jcp.2018.11.019`.

Perks, M. T., A. J. Russell, and A. R. G. Large (2016). Technical Note: Advances in flash flood monitoring using unmanned aerial vehicles (UAVs). *Hydrology and Earth System Sciences* 20.10, pp. 4005–4015. DOI: `10.5194/hess-20-4005-2016`.

Pfeifer, N. and C. Briese (2007). Laser scanning — principles and applications. *GeoSiberia 2007 - International Exhibition and Scientific Congress*. European Association of Geoscientists & Engineers. DOI: `10.3997/2214-4609.201403279`.

Picciafuoco, T., R. Morbidelli, A. Flammini, C. Saltalippi, C. Corradini, P. Strauss, and G. Blöschl (2019). On the estimation of spatially representative plot scale saturated hydraulic conductivity in an agricultural setting. *Journal of Hydrology* 570, pp. 106–117. DOI: `10.1016/j.jhydrol.2018.12.044`.

Raissi, M., P. Perdikaris, and G. Karniadakis (2019). Physics-informed neural networks: A deep learning framework for solving forward and inverse problems involving nonlinear partial differential equations. *Journal of Computational Physics* 378, pp. 686–707. DOI: `10.1016/j.jcp.2018.10.045`.

Rajib, A., Z. Liu, V. Merwade, A. A. Tavakoly, and M. L. Follum (2020). Towards a large-scale locally relevant flood inundation modeling framework using SWAT and LISFLOOD-FP. *Journal of Hydrology* 581, p. 124406. DOI: `10.1016/j.jhydrol.2019.124406`.

Rawls, W. J., D. L. Brakensiek, and N. Miller (1983). Green–Ampt Infiltration Parameters from Soils Data. *Journal of Hydraulic Engineering* 109.1, pp. 62–70. DOI: `10.1061/(asce)0733-9429(1983)109:1(62)`.

Rosenzweig, B. R., P. Herreros Cantis, Y. Kim, A. Cohn, K. Grove, J. Brock, J. Yesuf, P. Mistry, C. Welty, T. McPhearson, J. Sauer, and H. Chang (2021). The Value of Urban Flood Modeling. *Earth's Future* 9.1, e2020EF001739. DOI: `10.1029/2020EF001739`.

Rossman, L. A. (2017). *Storm Water Management Model*. Ed. by EPA. EPA/600/R-17/111. U.S. Environmental Protection Agency. Cincinnati, OH.

Rubinato, M., R. Martins, G. Kesserwani, J. Leandro, S. Djordjević, and J. Shucksmith (2017). Experimental calibration and validation of sewer/surface flow exchange equations in steady and unsteady flow conditions. *Journal of Hydrology* 552, pp. 421–432. DOI: `10.1016/j.jhydrol.2017.06.024`.

Russo, G. (2005). Central schemes for conservation laws with application to shallow water equations. *Trends and Applications of Mathematics to Mechanics*. Springer, pp. 225–246.

Sampson, C. C., A. M. Smith, P. D. Bates, J. C. Neal, L. Alfieri, and J. E. Freer (2015). A high-resolution global flood hazard model. *Water Resources Research* 51.9, pp. 7358–7381. DOI: `10.1002/2015WR016954`.

Sampson, J., A. Easton, and M. Singh (2006). Moving Boundary Shallow Water Flow Above Parabolic Bottom Topography. *Anziam Journal* 47, pp. C373–C387.

Schindler, B., J. Waser, H. Ribičić, R. Fuchs, and R. Peikert (2013). Multiverse data-flow control. *IEEE transactions on visualization and computer graphics* 19.6, pp. 1005–1019.

Schumann, G. J.-P., K. M. Andreadis, and P. D. Bates (2014). Downscaling coarse grid hydrodynamic model simulations over large domains. *Journal of Hydrology* 508, pp. 289–298. DOI: 10.1016/j.jhydrol.2013.08.051.

Shustikova, I., A. Domeneghetti, J. C. Neal, P. Bates, and A. Castellarin (2019). Comparing 2D capabilities of HEC-RAS and LISFLOOD-FP on complex topography. *Hydrological Sciences Journal* 64.14, pp. 1769–1782. DOI: 10.1080/02626667.2019.1671982.

Simons, F., T. Busse, J. Hou, I. Özgen, and R. Hinkelmann (2013). A model for overland flow and associated processes within the Hydroinformatics Modelling System. *Journal of Hydroinformatics* 16.2, pp. 375–391. DOI: 10.2166/hydro.2013.173.

Singh, J., M. S. Altinakar, and Y. Ding (2011). Two-dimensional numerical modeling of dam-break flows over natural terrain using a central explicit scheme. *Advances in Water Resources* 34.10, pp. 1366–1375. DOI: 10.1016/j.advwatres.2011.07.007.

Skøien, J. O., R. Merz, and G. Blöschl (2006). Top-kriging - geostatistics on stream networks. *Hydrology and Earth System Sciences* 10.2, pp. 277–287. DOI: 10.5194/hess-10-277-2006.

Smith, E., R. J. Smettem, P. Broadbridge, and D. A. Woolhiser (2002). *Infiltration Theory for Hydrologic Applications*. American Geophysical Union. DOI: 10.1029/wm015.

Sweby, P. K. (1984). High resolution schemes using flux limiters for hyperbolic conservation laws. *SIAM journal on numerical analysis* 21.5, pp. 995–1011.

Tatard, L., O. Planchon, J. Wainwright, G. Nord, D. Favis-Mortlock, N. Silvera, O. Ribolzi, M. Esteves, and C. H. Huang (2008). Measurement and modelling of high-resolution flow-velocity data under simulated rainfall on a low-slope sandy soil. *Journal of Hydrology* 348.1-2, pp. 1–12. DOI: 10.1016/j.jhydrol.2007.07.016.

Temam, R. (1984). *Navier–Stokes equations*. Vol. 2. North-Holland Amsterdam.

Teng, J., A. Jakeman, J. Vaze, B. Croke, D. Dutta, and S. Kim (2017). Flood inundation modelling: A review of methods, recent advances and uncertainty analysis. *Environmental Modelling & Software* 90, pp. 201–216. DOI: 10.1016/j.envsoft.2017.01.006.

Thacker, W. C. (1981). Some exact solutions to the nonlinear shallow-water wave equations. *Journal of Fluid Mechanics* 107, pp. 499–508.

Toro, E. F. (2001). *Shock-Capturing Methods for Free-Surface Shallow Flows*. John Wiley & Sons, Inc., pp. xi+309.

Vacondio, R., A. Ferrari, P. Mignosa, F. Aureli, and A. Dal (2016). Efficient Non-Uniform Grid for GPU-parallel Shallow Water Equations models. *River Flow 2016*. CRC Press, pp. 281–288.

Valiani, A., V. Caleffi, and A. Zanni (2002). Case Study: Malpasset Dam-Break Simulation using a Two-Dimensional Finite Volume Method. *Journal of Hydraulic*

References

Engineering 128.5, pp. 460–472. DOI: `10.1061/(ASCE)0733-9429(2002)128:5(460)`.

Van Leer, B. (1979). Towards the Ultimate Conservative Difference Scheme. V. A Second-Order Sequel to Godunov's Method. *Journal of Computational Physics* 32.1, pp. 101–136.

Wang, Y., A. S. Chen, G. Fu, S. Djordjević, C. Zhang, and D. A. Savić (2018). An integrated framework for high-resolution urban flood modelling considering multiple information sources and urban features. *Environmental Modelling & Software* 107, pp. 85–95. DOI: `10.1016/j.envsoft.2018.06.010`.

Waser, J., H. Ribičić, R. Fuchs, C. Hirsch, B. Schindler, G. Blöschl, and M. E. Gröller (2011). Nodes on Ropes: A Comprehensive Data and Control Flow for Steering Ensemble Simulations. *IEEE Transactions on Visualization and Computer Graphics* 17.12, pp. 1872–1881.

Whitham, G. B. (1999a). Water Waves. *Linear and Nonlinear Waves.* John Wiley & Sons, Inc. Chap. Water Waves, pp. 431–484. DOI: `10.1002/9781118032954.ch13`.

Whitham, G. B. (1999b). *Linear and Nonlinear Waves.* Vol. 42. John Wiley & Sons, pp. 1–636.

Wimmer, M. H., M. Hollaus, G. Blöschl, A. Buttinger-Kreuzhuber, J. Komma, J. Waser, and N. Pfeifer (2021). Processing of nationwide topographic data for ensuring consistent river network representation. Submitted to Journal of Hydrology.

Wing, O. E. J., A. M. Smith, M. L. Marston, J. R. Porter, M. F. Amodeo, C. C. Sampson, and P. D. Bates (2021). Simulating historical flood events at the continental scale: observational validation of a large-scale hydrodynamic model. *Natural Hazards and Earth System Sciences* 21.2, pp. 559–575. DOI: `10.5194/nhess-21-559-2021`.

Wing, O. E. J., P. D. Bates, C. C. Sampson, A. M. Smith, K. A. Johnson, and T. A. Erickson (2017). Validation of a 30 m resolution flood hazard model of the conterminous United States. *Water Resources Research* 53.9, pp. 7968–7986. DOI: `10.1002/2017WR020917`.

Xia, X., Q. Liang, and X. Ming (2019). A full-scale fluvial flood modelling framework based on a high-performance integrated hydrodynamic modelling system (HiPIMS). *Advances in Water Resources* 132, p. 103392. DOI: `10.1016/j.advwatres.2019.103392`.

Xia, X., Q. Liang, X. Ming, and J. Hou (2017). An Efficient and Stable Hydrodynamic Model with Novel Source Term Discretization Schemes for Overland Flow and Flood Simulations. *Water Resources Research* 53.5, pp. 3730–3759. DOI: `10.1002/2016WR020055`.

Xing, Y., Q. Liang, G. Wang, X. Ming, and X. Xia (2018). City-scale hydrodynamic modelling of urban flash floods: the issues of scale and resolution. *Natural Hazards* 96.1, pp. 473–496. DOI: `10.1007/s11069-018-3553-z`.

Yang, Y., L. Sun, R. Li, J. Yin, and D. Yu (2020). Linking a Storm Water Management Model to a Novel Two-Dimensional Model for Urban Pluvial Flood Modeling. *International Journal of Disaster Risk Science* 11.4, pp. 508–518. DOI: `10.1007/s13753-020-00278-7`.

Yu, D., J. Yin, and M. Liu (2016). Validating city-scale surface water flood modelling using crowd-sourced data. *Environmental Research Letters* 11.12, p. 124011. DOI: `10.1088/1748-9326/11/12/124011`.

Zehe, E., H. Elsenbeer, F. Lindenmaier, K. Schulz, and G. Blöschl (2007). Patterns of predictability in hydrological threshold systems. *Water Resources Research* 43.7. DOI: `10.1029/2006WR005589`.

Zischg, A. P., M. Mosimann, D. B. Bernet, and V. Röthlisberger (2018). Validation of 2D flood models with insurance claims. *Journal of Hydrology* 557, pp. 350–361. DOI: `10.1016/j.jhydrol.2017.12.042`.

Appendix

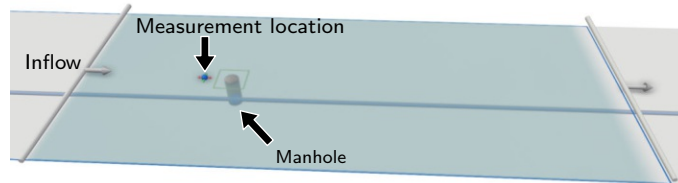## A1 Sewer–surface coupling

Fig. 1. Geometric setup of the surface-sewer coupling test case.

In this section, we present simulation results to verify the sewer–surface coupling against experimental data provided by (Rubinato et al., 2017). The setup consists of a flume and a single manhole connected to a pipe. The surface bed is 4 m wide and 8 m long with a slope of 1 m per 1 km. At the upper end, a hydrograph with a constant discharge of 11 L/s is specified. At the outlet, critical flow conditions are imposed. The manhole is located 2.5 m downstream of the inlet and has a diameter of 0.24 m. The invert level of the pipe is 0.478 m below the flume bed. Manning's roughness coefficient is set to 0.009 s/m$^{1/3}$ for both the pipe and the flume as both are PVC. In the experiment, the pipe pressure and the surface level was measured 0.34 m and 0.35 m away from the manhole (Fig. 1).

First, we tested steady state inflow from the surface into the sewer system for various prescribed surface discharges ranging from 5 L/s to 11 L/s. The simulation reaches a steady state after 300 s. The simulation is able to accurately reproduce the measured water depths and exchange flows (Fig. 2). With a mean absolute error (MAE) of 0.19 mm and relative differences ranging from 0.1% to 4.3%, the accuracy is excellent.

In the second test case, we simulated overflow from the sewer onto the wet flume. The surface inflow is fixed at 11 L/s and the pipe inflow ranges from 2.2 L/s to 7.6 L/s. Again, the simulated water depths agree well with the measured water depths with a MAE of 0.72 mm. The relative differences range from 3% to 4.8% in this case. Unfortunately, SWMM can not extract the pressure head at an arbitrary location along the pipe, so instead we extracted the pressure head directly at the manhole. The pressure head at the node is supposed to be lower than in the pipe, as energy is dissipated in the transition from the pipe into the manhole. This discrepancy is visible in Fig. 3b.

Overall, the coupled simulation correctly exchanges flows from the surface to the sewer system and vice versa as simulated and observed values agree and are comparable to results in the literature (Rubinato et al., 2017; Fernández-Pato and García-Navarro, 2018).
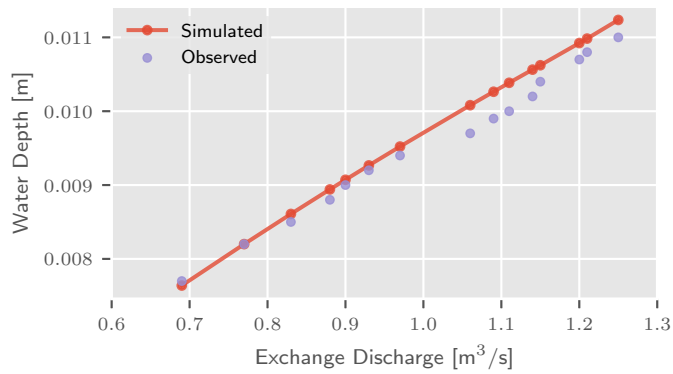
Appendix

Fig. 2. Surface to sewer coupling, i. e. water is flowing from the surface into the sewer. Simulated (red) and observed water depths (violet) over exchange discharge for a range of prescribed surface flow discharges.
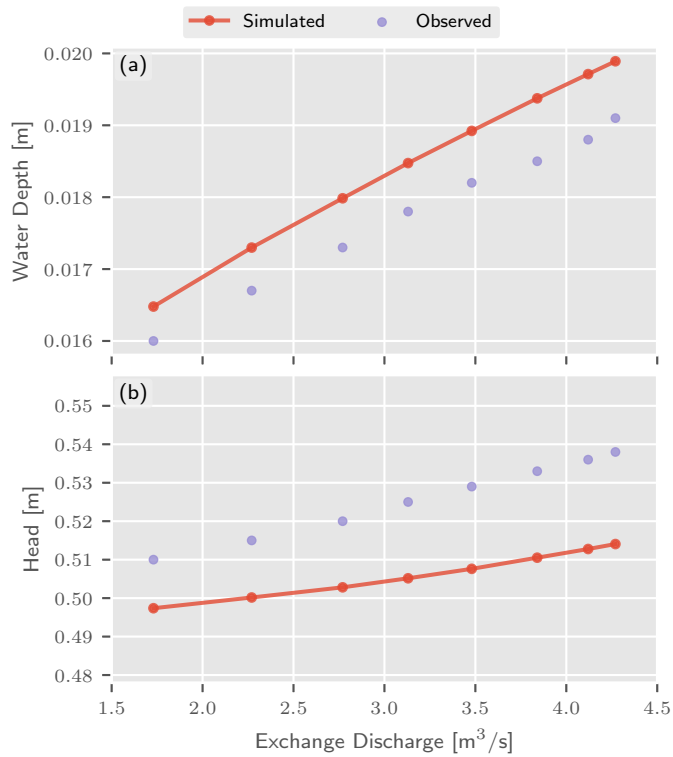

Fig. 3. Sewer to surface coupling, i. e. water is flowing from the sewer onto the surface. Simulated (red) and measured (violet) water depths (a) and pressure heads (b) over the exchange discharges. The water depths show good agreement. The simulated pressure head is extracted directly at the node and not 0.35 m away from the node as in the experiment thus resulting in lower simulated pipe pressure heads.